

Nanoscale

Accepted Manuscript



This is an *Accepted Manuscript*, which has been through the Royal Society of Chemistry peer review process and has been accepted for publication.

Accepted Manuscripts are published online shortly after acceptance, before technical editing, formatting and proof reading. Using this free service, authors can make their results available to the community, in citable form, before we publish the edited article. We will replace this *Accepted Manuscript* with the edited and formatted *Advance Article* as soon as it is available.

You can find more information about *Accepted Manuscripts* in the [Information for Authors](#).

Please note that technical editing may introduce minor changes to the text and/or graphics, which may alter content. The journal's standard [Terms & Conditions](#) and the [Ethical guidelines](#) still apply. In no event shall the Royal Society of Chemistry be held responsible for any errors or omissions in this *Accepted Manuscript* or any consequences arising from the use of any information it contains.

Cite this: DOI: 10.1039/c0xx00000x

www.rsc.org/xxxxxx

ARTICLE TYPE

Nanoparticles for photothermal therapies

D. Jaque, *^a L. Martínez Maestro, ^a B. del Rosal, ^a P. Haro-Gonzalez, ^a A. Benayas, ^{a,b} J.L. Plaza, ^a E. Martín Rodríguez, ^a and J. García Solé ^a

Received (in XXX, XXX) Xth XXXXXXXXX 20XX, Accepted Xth XXXXXXXXX 20XX

DOI: 10.1039/b000000x

The current status of the use of nanoparticles for photothermal treatments is reviewed in detail. The different families of heating nanoparticles are described paying special attention to the physical mechanisms at the root of the light-to-heat conversion processes. The heating efficiencies and spectral working ranges are listed and compared. The most important results obtained in both *in vivo* and *in vitro* nanoparticle assisted photo thermal treatments are summarized. The advantages and disadvantages of the different heating nanoparticles are discussed.

A. Introduction

A.I. Temperature and health: Thermal therapies

Thermal treatments are based on driving a part or the whole body above their normal temperature for a defined period of time. It is well known that temperature is one of the most important parameters determining the dynamics and viability of biological systems ranging from the simplest (cells) to the most sophisticated ones (tissues and organisms).¹⁻⁵ In the case of humans, any temperature increment above the normal body temperature (circa 37 °C) is usually regarded as a negative sign as it could indicate the presence of disease (fever) and also because it could lead to irreversible damage and even to fatal organ failure.⁶⁻⁸ Nevertheless, contrary to general thinking, controlled temperature increments could have positive effects in patients with an ongoing disease, such as cancer.^{4,9} The beneficial effects of thermal therapy in the treatment of cancer were first observed in the 19th century. At that time, it was observed that the administration of living bacteria to cancer patients could cause a partial tumor regression. This positive effect was only observed when the bacteria caused an infection in the patient, thus leading to the appearance of fever.^{10,11} Almost simultaneously with this pioneering work, successful treatment of uterine cervix cancer was achieved when treated with circulating heat water.^{7,11} However, the heating methods and temperature measuring technologies were not sufficiently advanced at that time, so the success and reproducibility of such treatments were reduced. As a consequence, the clinical application of these therapies was not accomplished. The interest on thermal treatments was reactivated in the 1980s, when different institutes and societies focused on the understanding and development of novel thermal therapies were started.¹² In the recent decades, the publication of several scientific reports that demonstrated substantial improvements in cancer treatment outcomes by using thermal treatments led to a renewed interest in thermal therapy.^{4,13-16} For the last few years, a great effort has been put not only in the development of novel

techniques for controlled and localized heating but also in the understanding of the mechanisms at the basis of temperature-induced cell killing and modification.^{1,17,18} Despite the large number of works published on these phenomena, this is a controversial issue that is still far from being fully understood. In any case, what has been clearly stated and demonstrated is that the effect caused by a temperature rise on a given bio-system cannot be completely understood by just considering the effect of temperature increment on individual cells. This is mostly because the thermal effects produced in the tissues surrounding the target (tumor in cancer treatments) also play a relevant role, known as *host effects*.¹¹ These effects (related to temperature-induced changes in tissue elasticity and blood flow rate) are difficult to predict and are generally considered to be of second order.^{19,20} It is widely assumed that the efficacy of a thermal treatment is given by two main factors: the magnitude of the temperature increment and the duration of the treatment.^{11,21} Indeed, the temperature-induced changes caused at the cellular level are unequivocally determined by the intensity and duration of the temperature increment.²² Depending on the magnitude of the induced temperature increment, thermal treatments and related effects of cancerous tumors can be classified as follows (see **Figure 1**):³

- *Irreversible injury treatments*.²³⁻²⁷ These treatments are carried out by increasing tumor temperature above 48°C during a period of time exceeding a few minutes. In this case, a drastic activation of cell death is achieved as a consequence of coagulative necrosis processes. The effect of temperature is therefore considered as drastic and *non-reversible*. These treatments are regarded to be highly efficient but, since cell death activation at such high temperatures is not only taking place in cancer cells but also in healthy ones, these treatments lack selectivity and so they are accompanied by relevant collateral damage to adjacent tissue.²⁸ Irreversible thermal treatments have clinical applications beyond cancer treatment, being also used in other fields such as urology²⁹ (for benign prostatic

hyperplasia treatment) and in cardiology for heart stimulation.³⁰ Above 60°C, an almost instantaneous and irreversible protein denaturation is instantaneously caused. For even larger temperatures (above 80 °C) tissue explosion and removal is produced due, among other reasons, to water vaporization. In this case it is said that tissue ablation is taking place.^{31, 32}

Hyperthermia treatments.^{13, 14} These thermal treatments consist in setting the temperature of a tumor within the 41-48°C temperature range (the so-called clinically relevant temperature range).³³ Hyperthermia treatments are usually applied in combination with other cancer treatments, such as radiation therapy or chemotherapy, whose efficacy is increased when applied after a hyperthermia cycle.^{4, 11, 34} The biological processes at the basis of hyperthermia treatments are still far from being completely understood. In the 41-48 °C temperature range, several process of relevance at the cellular level are simultaneously activated. On one hand, it is well known that when cellular temperature exceeds 39 °C, protein denaturation starts.^{35, 36} As a result of denaturation, proteins are prone to aggregation and the subsequent aggregates can have destructive consequences in the cell dynamics and survival rates. The induction of cellular temperatures above 41 °C not only causes protein denaturation but also temporary cell inactivation that could last for several hours. The response of the cells exposed to high temperatures depend both on the duration of the exposure and the magnitude of the temperature. Slightly lower temperatures (40 °C) cause cell inactivation in a process that lasts for several hours. Beyond that time, the surviving cells appear resistant to further exposure to such temperatures due to the creation of a temporary resistance to heat (the so called *thermo-tolerance*).³⁷ Application of slightly higher temperatures (41-42 °C) for a very prolonged time (several hours), would cause this transient thermo-tolerance (traditionally related to the synthesis of heat-shock proteins) to be overcome. “Severe” hyperthermia treatments (43-45 °C) cause long term cell inactivation.^{33, 38, 39} In this temperature range, the rate of biochemical reactions is significantly increased and this leads to the appearance of oxidative stress due to the increment of the intracellular density of reactive oxygen species.³³ These species can cause oxidative damage to proteins, lipids and nucleic acids. Indeed, successful tumor treatment in rabbits in this temperature range has been found to be accompanied by an increase in lipid peroxidation.⁴⁰ The basis of hyperthermia is that the appearance of cell thermo-tolerance is, in some cases, accompanied by a modification of the cellular response to some drugs or an increase in their sensitivity to X-ray irradiation. Generally speaking, moderate *hyperthermia* seems to be adequate for reducing cell resistance against radiation.⁴¹ It is widely assumed that this kind of treatments could lead to protein denaturation and aggregation while keeping the production of heat shock proteins at a minimum. Finally, there are reports about a “suppressive hyperthermia” (45-

48 °C), that produces rapid necrotic cell death in cancer cells that are resistant to standard hyperthermia (not induced by nanoparticles).^{1, 15, 42, 43}

Diathermia treatments.^{44, 45} These are based on heating processes up to 41°C. In this case, temperature does not induce relevant modifications at the cellular level. However, these soft to moderate heating treatments have beneficial health effects that are associated to different processes, such as increment in blood flow and ion diffusion rate across cellular membranes. In addition, some tissues (such as tendons) can be stretched more easily when they are subjected to moderate heating,⁴⁶ thus favoring muscle relaxation and pain relief. Because of all these effects, diathermia treatments are mainly applied in physiotherapy, sometimes in combination with electrical currents.

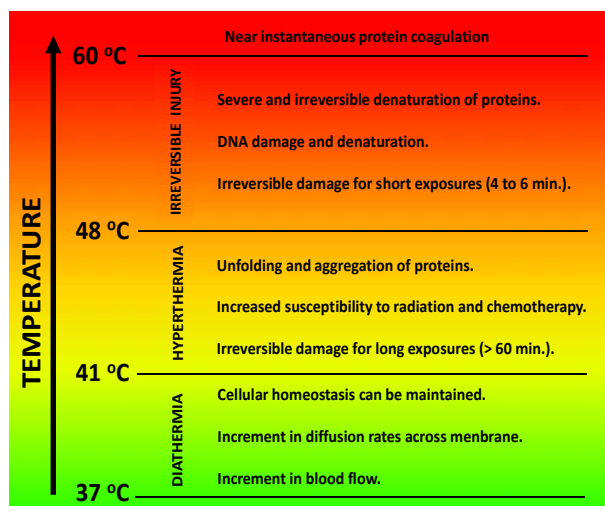


Fig. 1 Schematic diagram of the variety of effects caused by the different thermal treatments as classified by the corresponding operating temperature.

In addition to the above described temperature-induced modifications at cellular level, moderate hyperthermia treatments are also known to induce several physiological changes, including oxygenation, pH variation and blood flow.⁴⁷ It is widely assumed that the benefits of hyperthermia can be partially related to the fact that tumor tissues are poorly vascularized.⁴⁸ Tumor cells located well inside the tumor are relatively resistant to chemotherapy due to the poor drug delivery efficiency and also because some drugs need oxygen to cause cell cytotoxicity.⁴⁹ Increasing the tumor temperature would lead to a larger intra-tumor blood flow and, thus, to an improving of the chemotherapy. Another consequence of the temperature-induced increased blood flow inside tumors is an improved oxygenation, which is believed to make tumors more sensitive to radiation and to certain anticancer drugs.⁵⁰ Finally, blood flow increase also enhances the migration of immune cells to targets, which would allow for a better control of tumor burden.⁵¹⁻⁵³

A.II. Conventional thermal treatment techniques

For the purpose of cancer treatment, *hyperthermia* (HT) is nowadays attracting much attention from the scientific community, as the corresponding temperature range seems to be

assumed as the optimum one.^{11, 12} When compared to traditional techniques for tumor destruction, such as surgery (which is limited to tumors that are surgically accessible) and chemotherapy or radiation therapy (which present a number of significant collateral negative effects),⁵⁴⁻⁵⁶ HT therapies seem to be much less invasive. Moderate HT (41-42 °C) is not considered as a complete therapy in itself since tumor destruction requires combination with other techniques. Indeed, the role of HT is to increase the efficacy of traditional treatments, reducing their negative side effects.^{4, 57}

For the purpose of thermal treatment of tumors (based either on thermal ablation or hyperthermia), it is necessary to induce a well localized heating, so that a significant temperature increase is achieved in the tumor, while keeping the temperature of the surrounding tissue at a normal level.^{11, 12, 24} Producing well defined “hot regions” is far from being an easy task. Traditionally, external heating of superficial tumors has been achieved by using superficial applicators (RF, microwave or ultrasound) in different modalities (waveguide, spiral, current sheet) that are allocated on the surface of the tumor.^{4, 58, 59} The absorption of the incident radiation by the tumor causes a temperature increment whose magnitude is strongly dependent on different properties of the tumor, such as its surface characteristics or the water content inside it.⁶⁰ In general, radiation reaches tumors located at few (3-4) centimeters below the skin, this fact limiting the therapeutic depth of these treatments.⁶¹ For non-superficial tumors, the heating apparatus are more sophisticated and vary depending on whether the tumor is located close to a body cavity or not.⁶² In the former case, local heating could be achieved by inserting thin and flexible electrodes through natural apertures, allowing for direct heating of the tumor.⁶³ For interstitial tumors (deep tumors that are not located close to a body cavity), well localized HT requires the use, in combination to local anesthesia, of thin antennas that are inserted very close to the tumor to be treated.^{64, 65} Depending on the tumor location and size, this process could require the additional use of real time imaging techniques such as ultrasound imaging. Once the antennas have been placed close to the tumor, remote heating is induced by delivering electro-magnetic radiation (radiofrequency or micro waves).^{66, 67} In the case of relatively large tumors, the reduced penetration depth of electromagnetic radiation may lead to a nonhomogeneous temperature distribution inside the tumor, which would only be significantly high in the regions closest to the antennas. In such cases, homogeneous heating could be achieved by simultaneous insertion of multiple antennas in the tumor surroundings.^{68, 69}

A.III. Nanotechnology based thermal therapies

Nanotechnology is currently proposing alternative techniques for remote and localized heating that are based on the development and bioincorporation of heating nanoparticles (hereafter HNPs).⁷⁰⁻⁷² These nanoparticles combine four properties: (i) They are smaller than 100 nm, so that these small sizes allow for long circulating times in the bloodstream and enable effective nanoparticle incorporation into cells, (ii) They are dispersible in biocompatible liquids, so that they can be easily injected into organisms, (iii) In absence of any external stimulus, they should present minimum adverse effects on the normal behavior of the host biosystem and (iv) They should produce heat in an efficient

manner when externally excited.

Nanoparticles for magnetothermal therapy

Nowadays, the most well-known and popular HNPs are those in which heating is induced by the application of oscillating magnetic fields (magnetic heating nanoparticles, M-HNPs).⁷³⁻⁷⁵

Heat generation in M-HNPs under oscillating magnetic fields occurs as a consequence of different mechanisms, including hysteresis loss, Néel relaxation and Brown relaxation.⁷⁴ The procedure to apply M-NPs based HT treatments is simple: These NPs are introduced into the tumor site either by direct injection or by targeted delivery. Then, an oscillating magnetic field is applied so that the magnetic nanoparticles interact with this field to generate heat through any of the already mentioned mechanism.^{76, 77} The proof of concept of HT treatments based on M-HNPs was provided in 1957 by Gilchrist et al. who demonstrated tissue heating by a 1.2 MHz magnetic field based on the presence of γ -Fe₂O₃ magnetic nanoparticles.⁷⁸ This first demonstration motivated an intense research exploring treatment optimization through the study of different materials, magnetic field geometries, surface treatments and delivery procedures. As a consequence of such an intense research, in 2007 Jordan et al. reported the first clinical study of magnetic hyperthermia.⁷⁹ In that work, authors demonstrated successful and safe treatment of brain tumors by using aminosilane-coated superparamagnetic iron oxide nanoparticles. M-HNPs are nowadays considered as a multi-functional platform for cancer therapy, since they can be used for simultaneous tumor heating and imaging.^{74, 77} This dual function is based on the ability of MNPs to produce a relevant enhancement in the proton relaxation of specific tissues, so they can be used as Magnetic Resonance Imaging (MRI) contrast agents.⁸⁰

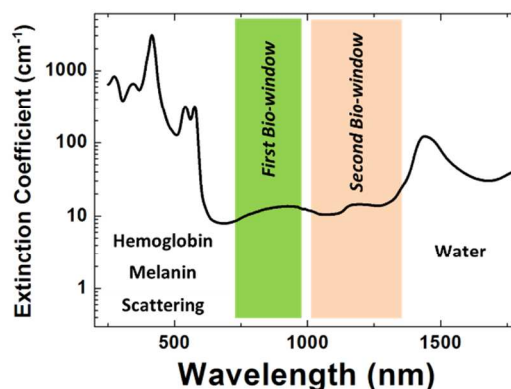


Fig. 2 Extinction coefficient of a representative tissue. The different effects leading to light attenuation (such as the presence of hemoglobin, water and optical scattering) have been indicated. The spectral extensions of the two biological windows are also indicated.

Nanoparticles for photothermal therapies

Despite the good results obtained so far by using M-HNPs, nanotechnology is also exploring other alternatives. In particular, the recent development of nanoparticles capable of efficient heat generation under illumination with laser radiation has attracted much attention for the last few years.⁸¹ The use of laser light-induced hyperthermia/thermal ablation, i.e. photothermal therapy, has been traditionally considered as a non-reliable technique due

to the fact that human tissues show strong extinction coefficients in the visible range of the optical spectrum, this fact limiting photothermal treatments to superficial tumors.^{82, 83} In addition, laser light energy is expected to be absorbed by both healthy and cancerous tissues, which leads to both a reduction in the efficacy of heat delivery within the tumor and an increment in the non-specific damage of the adjacent tissues. However, photothermal therapy is nowadays attracting considerable attention because of the possibility of controlling the incorporation of light-activated heating nanoparticles (L-HNPs) into tumors, allowing for high heat deposition in the tumor area at low laser light intensities and thus minimizing the damage in the surrounding healthy tissue.^{84,}

Further reduction of non-desired light absorption by healthy tissues can be achieved by using specific laser wavelengths lying in the so-called biological windows.^{86, 87} Biological windows can be defined as the spectral ranges where tissues become partially transparent due to a simultaneous reduction in both absorption and scattering. **Figure 2** shows the extinction spectrum (accounting for both absorption and scattering spectra) of a typical human tissue. In a first order approximation, extinction of optical radiation into tissues is determined by the presence of absorption bands of constituents (such as water and hemoglobin) and by the scattering caused by natural tissue. The presence of several absorption bands is used to define two main biological windows (also shown in **Figure 2**):

- *The first biological window* extends from 700 nm to 980 nm and corresponds to the spectral range defined between the visible absorption band of hemoglobin and the characteristic 980 nm absorption band of water. In this spectral region, light absorption strongly vanishes but optical extinction still exists due to the presence of residual scattering, whose relevance decreases for longer wavelengths.
- *The second biological window*^{86, 88} extends from 1000 nm to 1400 nm, both limits corresponding to water absorption bands. In this spectral window, optical absorption does not vanish completely (averaged water absorption coefficient is close to 0.5 cm^{-1}) but, on the other hand, optical scattering is minimized (in respect to the first biological window) because of the longer wavelengths.

The use of specific laser sources working in the biological windows for photothermal therapy does not only reduce the non-selective heating of healthy tissue but, at the same time, allows for deep tissue treatments. Indeed, this is due to the longer optical penetration depth obtained from the simultaneous minimization of scattering and absorption processes.⁸⁹ Working within any of these two biological windows would make possible to achieve the optical excitation of L-HNPs allocated in non-superficial tumors and, hence, the development of deep tissue HT treatments based on light-activated heating nanoparticles.^{16, 90, 91} Being realistic, the maximum optical penetration depth achievable in human tissues is within a few centimeters range.⁸⁹ Nevertheless, nanoparticle-based photothermal treatment of deeper tumors is still achievable if an optical fiber delivery is used in combination with endoscopy techniques.⁹² In this case L-HNPs are incorporated into the tumor to be treated (by appropriate functionalization or by direct injection) and it is externally illuminated/heated by means of one or more fibers.

In order to achieve nanoparticle-based selective and efficient photothermal therapies, the L-HNPs to be used must fulfill a number of requirements:

- *Large absorption cross sections for optical wavelengths within any of the two biological windows.* This would ensure an efficient absorption of optical radiation and, in combination with large light-to-heat conversion efficiency, would make thermal therapy possible with low-power laser sources.⁹³
- *Low toxicity.* Toxicity of L-HNPs should only be activated in presence of optical radiation. L-HNPs should be non-toxic to both healthy and cancer cells. This is required to achieve a selective treatment with minimum side effects.⁹⁴
- *Easy functionalization.* This would also allow for highly selective treatments since tumor targeting would become possible.^{95, 96}
- *Good solubility in biocompatible liquids.* This would ensure long circulation times (half-lives) in the bloodstream and, consequently, easy access to cancer tumors even at low circulation flows.⁹⁷⁻⁹⁹

Nowadays, and thanks to the continuous research on synthesis techniques, a large number of research groups are capable of large-scale nanoparticle synthesis with a high degree of control over the morphology and surface. Some of them satisfy all the requirements listed above and, hence, have already been used as L-HNPs.^{100, 101} They can be classified in different families: metallic nanoparticles,¹⁰² semiconductor nanocrystals,⁸⁴ rare earth ions doped nanocrystals,¹⁰³ carbon-based nanoparticles¹⁰⁴ and organic nanoparticles.¹⁰⁵ The morphology, heating mechanisms, efficiency and spectral ranges of operation greatly differ from one family to another. When designing a specific nanoparticle-based photothermal therapy, the particular L-HNP to be used depends on the nature and location of the tumor to be treated as well as on the laser source to be used. Of course, making the adequate choice among all the available L-HNPs requires a complete comparative study of all of them.

The purpose of this work is to simplify this task by providing a complete review of all the L-HNPs available nowadays for photothermal therapies. We have mostly focused on the L-HNPs used to fight against cancer tumors. This review is divided in five Sections. In addition to this introductory section (Section A), Section B includes a general overview of the spectroscopic properties (determining the light-nanoparticle interaction). The different heating mechanisms, responsible of the light-to-heat conversion for each type of nanoparticle, are also described and explained. Section C provides a brief description of the synthesis procedures and morphologies of the different families of L-HNPs is provided. Section D includes several representative examples of the application of L-HNPs to both *in vivo* and *in vitro* thermal treatments. Finally, in Section E we have included a subjective analysis of the state of the art and some general ideas about the future challenges and perspectives of nanoparticle-based photothermal therapies.

B. Spectroscopy and heating mechanisms

In this section the light-matter interactions taking place in the different NPs capable of light-induced heating are reviewed and

special attention is paid to the different mechanisms at the basis of the light-to-heat conversion processes. The understanding of these mechanisms is not only interesting from the fundamental point of view but is also essential when these nanoparticles are to be applied in real photothermal therapies. In particular, light-matter interaction processes in heating nanoparticles would determine the spectral shape of the extinction coefficient. This, in turn, defines the operating spectral ranges of the different nanoparticles that vary largely from system to system, as can be observed in **Figure 3**. In this figure the first and second biological windows (I-BW and II-BW) have been indicated. It can be seen that most of the nanoheaters operate in the I-BW but only few of them (GNRs and CNTs) operate in the II-BW. At this point it should be mentioned that for photo-thermal therapies, the use of heating nano-particles working in the I-BW seems to be more advantageous than working in the II-BW. This is so because, I-BW is characterized by a negligible absorption in such a way that the solely heating source would be the heating nanoparticles.⁶⁰ On the other hand, in the II-BW, water absorption does exist in all the range. For instance, water absorption coefficient at 1090 nm is close to 0.3 cm^{-1} . This absorption causes the appearance of background heating, and so the selectivity and efficiency of the photo-thermal therapy reduce, as it has been, indeed, experimentally corroborated during in vivo experiments.¹⁰⁶

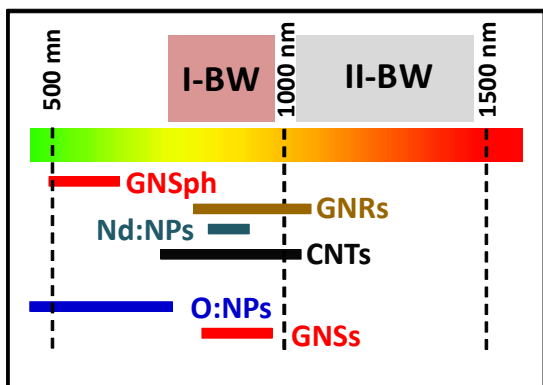


Fig. 3 Schematic representation of the spectral operating ranges corresponding to the different heating nanoparticles under study in this review: gold nanospheres (GNSph), gold nanorods (GNRs) neodymium-doped nanoparticles (Nd:NPs), carbon nanotubes (CNTs), organic nanoparticles (O:NPs) and gold nanostars (GNSs).

When a nanoparticle is illuminated by a light beam, some of the incident photons will be scattered by the nanoparticle while others will be absorbed. The absorbed photons are responsible for heat production and luminescence. These outgoing energy forms are schematically displayed in **Figure 4**. The total number of photons interacting with the NP is determined by its extinction coefficient (α_{ext}). This is given by the sum of the absorption (α_{abs}) and scattering (α_{sct}) coefficients, in such a way that $\alpha_{ext} = \alpha_{abs} + \alpha_{sct}$. The extinction coefficient depends on the concentration (N) of illuminated NPs and on the so-called extinction cross section ($\sigma_{ext} = \sigma_{abs} + \sigma_{sct}$, where σ_{abs} and σ_{sct} denote the absorption and scattering cross sections, respectively). The absorption efficiency, Φ_{abs} , of a given nanoparticle is traditionally defined as the number of absorbed photons divided

by the total number of incident photons interacting with the nanoparticle (i.e. being either absorbed or scattered).

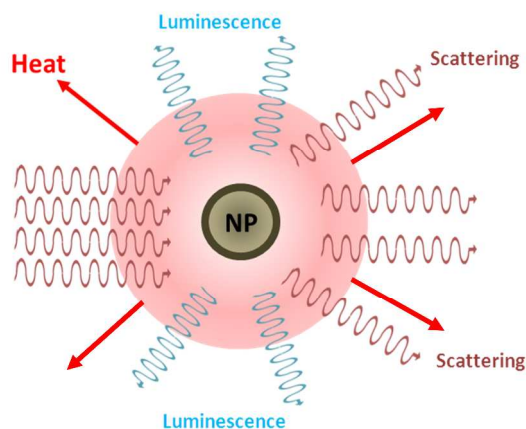


Fig. 4 Schematic representation of the different processes activated when a light beam interacts with a nanoparticle. The presence of scattering, luminescence and heat generation are included. Heat and luminescence occur as a result of light absorption.

The energy absorbed by the NP (energy of incident photons multiplied by the total number of absorbed photons) can be released by either the emission of photons of different energy (frequency) from that of incident photons (luminescence) or by the emission of phonons (i.e. by generating heat). Both processes are also schematically shown in **Figure 4**. For the purpose of efficient photothermal therapies, NPs with large absorption efficiencies and low luminescence quantum yields are required, since this will ensure a large light-to-heat conversion efficiency. In this section, the light-matter interaction processes activated when a nanoparticle is illuminated by a light beam will be described for the different heating nanoparticles under review in this work.

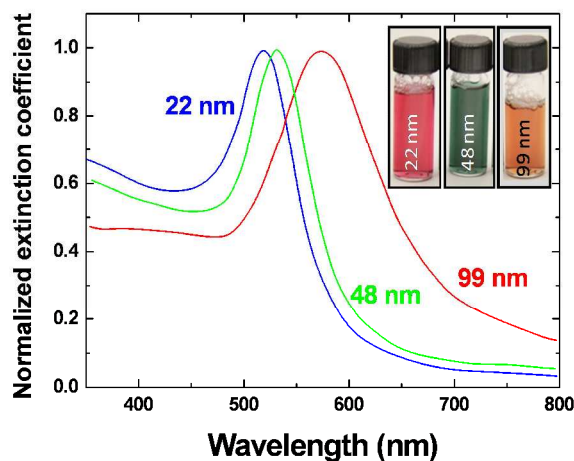


Fig. 5 Normalized, to maximum, extinction coefficient of three aqueous solutions of spherical gold nanoparticles with diameters of 22, 48 and 99 nm. Figure reproduced with permission from Reference 107.

B.I. Metallic nanoparticles

Heat produced by illuminated metals is a well-known effect largely observed in normal life. For bulk metals, this effect is

almost wavelength independent within the optical range and it does not depend on crystal size or shape. Nevertheless, when dealing with metallic nanoparticles, the situation becomes more complicated and, although light-induced heating is still present, heat generation becomes strongly dependent on both the illuminating wavelength and the nanoparticle size and geometry. Indeed, the optical properties of metallic nanoparticles are strongly influenced by size, shape and environment. To properly understand these effects, it is very illustrative to examine the extinction spectrum of spherical metal nanoparticles. **Figure 5** shows the room temperature extinction spectra of three aqueous solutions containing dispersed spherical gold nanoparticles of different diameters (22 nm, 48 nm and 99 nm).^{107, 108} It can be seen how the extinction peak shifts to the red as the nanoparticle size is increased. This effect, which allows for excitation tunability within the visible spectral region, is a clear evidence of the critical role played by size in determining the optical properties of metallic nanoparticles. Let us first focus our attention in the smallest gold nanoparticles (22 nm): their extinction spectrum is dominated by a broad band peaking at about 510 nm that confers the typical “red-purple” color to the aqueous solution of these small gold nanoparticles (see inset in **Figure 5**). This color is at variance with the familiar yellow color of bulk gold, caused by a reduction in the reflectivity with increasing wavelength in the visible spectrum. The 510 nm band is due to the so-called “*surface plasmon resonance*”. This resonance essentially occurs because the oscillating electric field of light forces surface free electrons in the metal to undergo a collective and coherent oscillation along the polarization direction of the electric field. Mie’s formalism solved the Maxwell’s equations for small spheres embedded in a medium and demonstrated that plasmon resonances appear at certain frequencies of the excitation light, depending on the dielectric constants of the metal and its surrounding medium and on the diameter of the spherical particles.¹⁰⁹ This explained the extinction spectrum of metallic nanoparticles with characteristic dimensions up to about 20 nm and thereby the one observed in **Figure 5** for the 22 nm diameter gold nanoparticles.¹¹⁰ It is important to mention that the Mie theory is limited to diluted solutions, i.e. isolated non-interacting nanoparticles, which is the case for the majority of solutions used in biomedicine. However, metallic aggregates can occur for highly concentrated solutions. This aggregation drastically changes the optical properties as a result of inter-particle interaction, as extensively described by Ghosh et al.¹¹¹ Mie’s theory does not explain the optical properties of nanoparticles larger than about 20 nm and so the red-shift of the surface plasmon resonance (extinction maximum) observed for the 48 nm and 99 nm nanoparticles (**Figure 5**). For these “larger” gold nanospheres, the oscillating electric field of optical radiation cannot be assumed to be constant all along the nanoparticle and so it does not homogeneously polarize the nanoparticles. As a result, the dipole order approximation is no longer valid and higher multipolar orders must be considered. The resonance frequencies for these higher order modes peak at lower energies than that of the dipolar one and so the extinction spectrum is redshifted with increasing particle size, as observed in **Figure 5**.

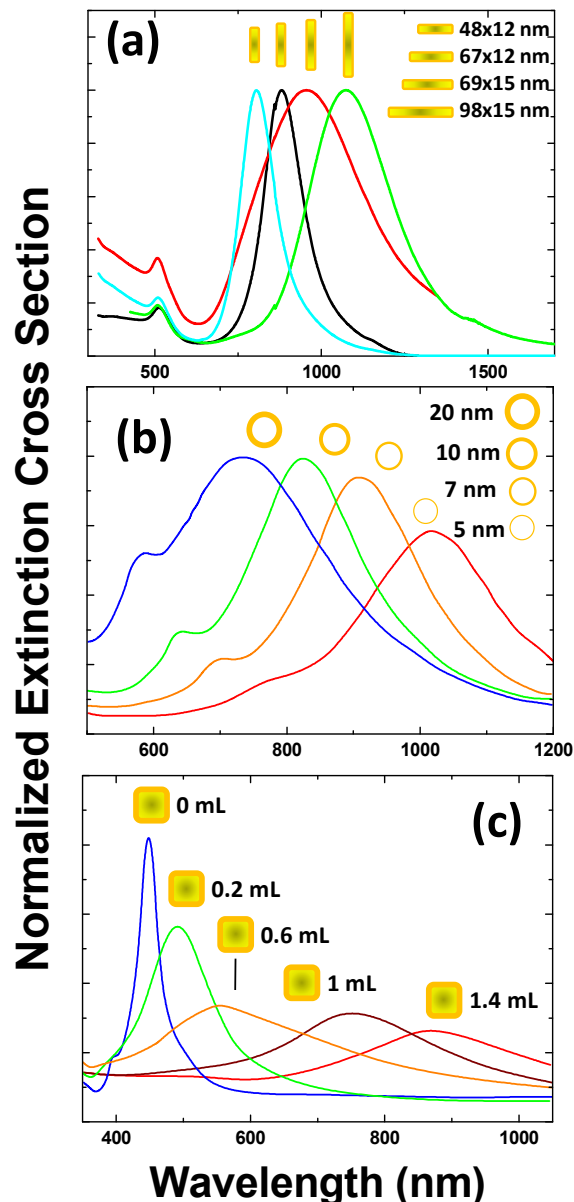


Fig. 6 Extinction cross section spectra (in arbitrary units) of: (a) gold nanorods with different aspect ratios, (b) core(silica)/shell(gold) nanoparticles with different shell thicknesses and (c) gold nanocages with different gold contents. Data for **Figure (a)** extracted from Reference 112. **Figures (b) and (c)** reproduced with permission from References 112 and 113.

As mentioned in Section A, efficient and selective photothermal treatments require nanoparticles that can be optically excited with light lying in the biological windows; i.e. optically excited at wavelengths larger than 700 nm. Increasing the size of single metallic nanospheres (see **Figure 5** for gold nanospheres) allows for surface plasmon tuning in the visible (up to 600 nm) but not in the NIR spectral range. Fortunately, this issue can be solved by using metallic nanoparticles with more complex geometries such as core(silica)-shell(gold) nanoshells, nanorods, nanocages and even nanostars (see **Figure 6**). When

the shape of the metallic nanoparticle deviates from the highly symmetric spherical shape, the dynamics of plasmonic oscillations are strongly modified. The shape influence in the optical extinction of metallic nanoparticles can be explained by the so-called Gans model, which is a formal extension of the Mie theory and explains the extinction cross sections of dilute solutions of randomly oriented gold nanoparticles having ellipsoidal geometries. Despite the good results yielded by this model to describe and predict the optical properties of elliptic metallic nanoparticles, it cannot be applied to more complex geometries. To do that, advanced simulation methods (such as discrete dipole approximation, DDA) need to be used. Indeed, there are several works demonstrating how it is now possible to simulate the optical properties of metallic nanoparticles with almost any arbitrary geometry.¹¹⁴⁻¹¹⁶

Among the different non-spherical metallic nanoparticles, gold nanorods (GNRs) have attracted a great deal of attention due to the large number of synthesis methods available, the high achievable monodispersity and the rational control over the aspect ratio, which is primarily responsible for the change in their optical properties. **Figure 6(a)** shows, as a relevant example, the extinction spectra of gold nanorods with different aspect ratios (length/width). First, it can be seen that for all nanorods the extinction spectrum splits into two main broad bands: a near infrared extinction band, which corresponds to longitudinal oscillations of electrons (longitudinal surface plasmons, i.e. electron oscillations along the longest dimension of the GNR) and a weak visible extinction band that is caused by the light-induced transverse electronic oscillations (transverse surface plasmons, i.e. surface electron oscillations along the short dimension of the GNRs). It is important to notice that the extinction band corresponding to the longitudinal electronic oscillations is strongly red-shifted when the aspect ratio is increased. Thus, this plasmonic extinction band allows for spectral tunability into the biological window by simply changing the aspect ratio of GNRs. This makes GNRs particularly suitable for photothermal therapy. When illuminated with UV-visible radiation, GNRs generate a visible luminescence, which can also be generated by NIR multiphoton excitation. The origin of this luminescence is, at present time, not fully determined, although it is widely assumed that it results from the intrinsic luminescence of gold modulated by a local enhancement factor that depends on the size and shape of the gold nanoparticle. Visible luminescence of GNRs has been widely used for multiphoton fluorescence imaging of bio-systems. Despite its great utility for imaging purposes, it is undesirable for photothermal applications in which, ideally, all the energy absorbed by the nanoparticle from the incident radiation should be relaxed as heat and not as fluorescence. Nevertheless, previous works dealing with the fluorescence of gold nanoparticles have concluded that the fluorescence quantum yield is well below 1%, in such a way that it can be assumed that all the absorbed energy is transformed into heat. Under this assumption, the light-to-heat conversion efficiency would be determined by the relative contribution of the absorption cross section to the total extinction cross section. In this context, the heating efficiency (Φ_{heat} , defined as the fraction of extinct energy that is transformed into heat) of gold nanoparticles is given by the absorption efficiency (Φ_{abs} , fraction

of extinction photons that are absorbed by the nanoparticle). Thus, for a gold nanoparticle, we can write:

$$\Phi_{heat} = \Phi_{abs} = \sigma_{abs} / \sigma_{ext} \quad (1)$$

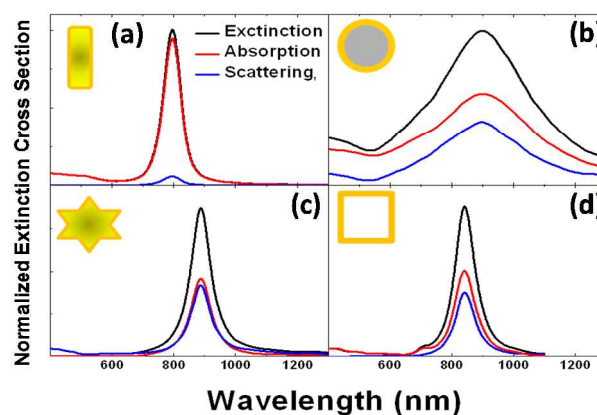


Fig. 7 Simulated extinction, absorption and scattering cross section spectra of: **(a)** gold nanorods (15 nm width and 45 nm length), **(b)** gold nanoshells (silica core of 60 nm in radius and gold shell 10 nm thick), **(c)** gold nanostars (32 nm effective radius and a total number of 6 tips) and **(d)** gold nanocages (5 nm thick walls and 50 nm edge length). Data extracted from References 92,116 and 117..

According to (1) gold nanoparticles with $\sigma_{abs}/\sigma_{ext}$ ratios close to unity are desirable to obtain efficient photothermal therapies. The relative contribution of scattering and absorption processes to the net extinction cross section of gold nanorods is difficult to predict *a priori* and advanced simulation methods are required. **Figure 7** shows the calculated (based on DDA simulations) extinction, absorption and scattering cross sections of a gold nanorod with 45 and 12 nm in length and width, respectively. These GNRs show the plasmon resonance close to 800 nm. This wavelength, has been shown to be optimal for nanoparticle based photothermal treatments, as it leads to minimum collateral heating.¹⁰⁶ For this particular rod gold geometry and size, simulations predict an absorption efficiency close to 98% so that almost all the 800 nm photons interacting with the GNR are being absorbed. Indeed, this numerical prediction has been, experimentally corroborated by L.M. Maestro et al., who found a heating efficiency close to 100% for GNRs by using quantum dot-based fluorescence thermometry.¹¹⁷ According to the extensive work done by El-Sayed's group, GNRs usually show absorption efficiencies above 90% except when the GNR radius exceeds 20 nm.^{82, 107, 108, 112, 116} For such "wide" GNRs, absorption efficiencies are predicted to decrease down to 60%. Interestingly, when the GNR width (diameter) is kept close to 15 nm, the heating efficiency remains above 90%, independently of the GNR length (at least for lengths as large as 160 nm). The relevance of the GNRs geometry to determine their heating (absorption) efficiency is illustrated in **Figure 8** (top), which shows the calculated absorption efficiency of GNRs with a fixed aspect ratio (3.9) as a function of the effective radius (defined as $r_{eff} = (3V/4\pi)^{1/3}$, where V is the GNR volume). It is evidenced that as the GNR volume is increased scattering becomes more relevant, and so the absorption efficiency decreases. Indeed, this was expected, since larger nanoparticles are expected to scatter light more efficiently.

According to numerical simulations it is possible to tailor GNRs in order to shift the plasmon resonance to the infrared (above 1000 nm) while keeping the GNR radius at a minimum. As an example, GNRs with 15 nm in diameter and over 100 nm in length lead to a plasmon resonance above 1000 nm. Such high aspect ratio GNRs would be especially suitable for photothermal treatments in the second biological window (1000-1400 nm).

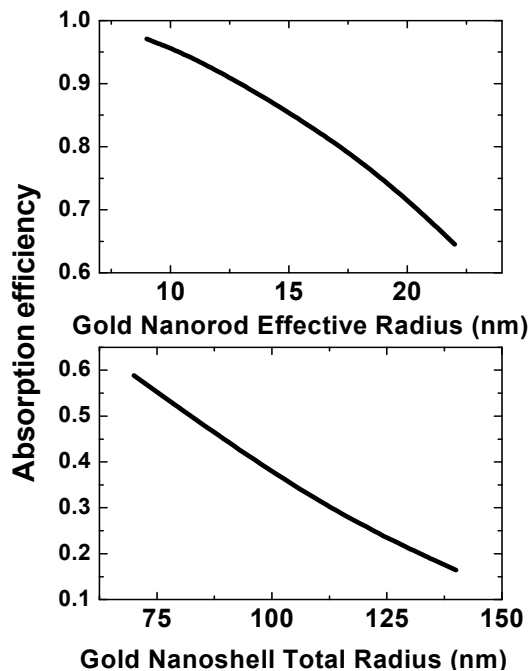


Fig. 8 Top. Dependence of the absorption efficiency of GNRs as a function of their effective radius for a fixed aspect ratio (3.9). **Bottom** Dependence of the absorption efficiency of GNShs as a function of the total radius for a fixed core/shell ratio of 0.857. Data extracted from Reference 116.

Another representative example of gold nanoparticles with peak extinction cross sections within the biological windows are the core/shell structures, commonly denoted as nanoshells (GNShs). **Figure 6 (b)** shows the extinction cross section of gold GNShs constituted by a silica core (60 nm in diameter) surrounded by gold shells of different thicknesses (varying from 5 up to 20 nm). In all the cases, a broad plasmonic extinction band is observed, which is shifted towards longer wavelengths as the gold shell thickness is reduced. Indeed, this behavior is in agreement with the calculations performed by Jain et al. who applied the Mie's theory to calculate the extinction spectra of a variety of silica-Au nanoparticles with different R_1 (core) and R_2 (shell) radii.¹¹⁶ They concluded that the spectral position of the plasmonic extinction band was expected to be strongly dependent on both the core/shell ratio (R_1/R_2) and total radius ($R_{\text{tot}}=R_1+R_2$). In fact, they predicted a spectral redshift of the plasmonic band from 650 up to 900 nm when increasing the core-shell ratio for a fixed nanoshell radius ($R_2=70$ nm). In addition, the plasmonic band could even be shifted from 900 nm to 1100 nm, by increasing the nanoshell total radius R_{tot} while maintaining the core shell ratio ($R_1/R_2=0.857$) fixed. Therefore, GNShs allow for broad optical tunability within the biological spectral windows. Moreover, Jain et al. calculated the relative contribution of both

scattering and absorption to the total extinction spectra.¹¹⁶ A representative example is included in **Figure 7(b)** that includes the absorption, scattering and extinction cross section spectra (in arbitrary units) corresponding to a GNSh constituted by silica core 120 nm in diameter covered by a 5 nm thick gold shell. Such a GNSh has a plasmon resonance at about 900 nm and shows absorption efficiency close to 60%. Low absorption efficiencies seem to be a general feature of GNShs, as extracted from previous simulations dealing with GNShs of different core and shell dimensions¹¹⁸. This is evidenced in **Figure 8**, which includes (at bottom) the absorption efficiency of GNShs of a fixed R_1/R_2 ratio (0.857) as a function of the total radius (R_T). As can be observed, absorption efficiency is always below 0.6. Furthermore, GNShs whose total radius is larger than about 150 nm behave as almost full scattering particles, being useless for photothermal therapies. Indeed, the low absorption efficiencies of GNShs are a serious drawback for their application in photothermal therapies. Nevertheless, GNShs show interesting properties over other gold nanoparticles such as broad extinction cross section spectra extending up to 2 μm thus, allowing for wavelength tunable photothermal therapies within the second biological window. Extraordinary broad extinction spectra have been found in larger GNShs, with both core and shell radius over 100 nm. This has been explained by the simultaneous contribution of multipolar plasmonic resonances.¹¹⁹

The continuous improvement on synthesis methods has made possible to fabricate gold nanoparticles with more complicated geometries such as gold nanostars (GNSs). GNSs are constituted by a central spherical nucleus surrounded by several tips (see **Figures 7(c) and 9**). GNSs were initially studied as novel candidates for surface-enhanced Raman spectroscopy (SERS), based on the strong field enhancement taking place at their tips. Thanks to their particular geometry, GNSs have also been demonstrated to be excellent drug deliverers with an outstanding efficiency.¹²⁰ GNSs provide a large surface on which a high concentration of drug molecules can be loaded, thus reducing the required amount of drug molecules in respect to conventional approaches. In addition, recent works have demonstrated that, when incorporated into cancer cells, GNSs are able to change the shape of the cell nucleus, which improves the effectiveness of the drug release as well as minimize resistance against external treatments.¹²⁰⁻¹²² Very recently, GNSs have emerged as novel photothermal agents with large light-to-heat conversion efficiencies.^{122, 123} Indeed, GNSs have already been used for both hyperthermia and ablation therapies. Their optical properties can be tailored by controlling the growth process, so that the desired length, width and number of tips as well as the dimensions of the central core can be obtained. Changing these parameters would not only lead to a spectral shift of the plasmon resonance (see **Figure 9**) but also to a modification in the absorption efficiency. According to the different simulations published up to now, it can be concluded that GNSs with a reduced number of branches and/or with short and smooth tips show relatively low absorption efficiencies (see **Figure 9**).¹⁶² On the other hand, when the branch tips are sharper, the absorption efficiency increases up to values above 0.9 (see simulations included in **Figure 9**). Indeed, there are some reports stating that such sharp GNSs with plasmon resonances close to 800 nm could present light-to-heat conversion

efficiencies superior to those of GNRs with plasmon resonance around that wavelength.¹²¹

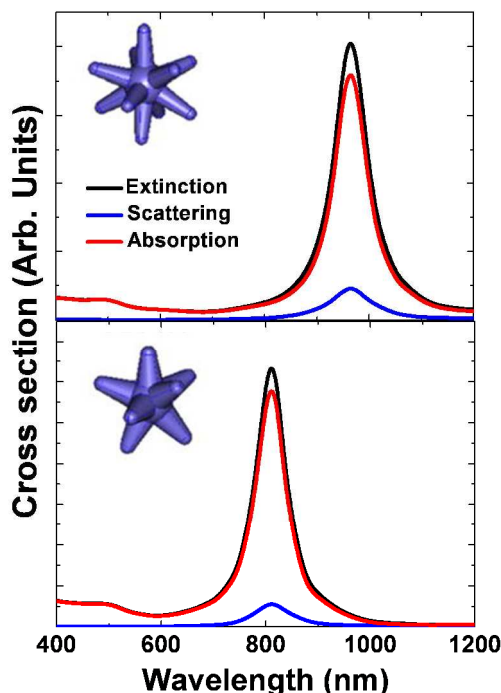


Fig. 9 Simulated wavelength dependence of extinction, absorption and scattering cross sections of gold nanostars with different geometries. Simulations at the top correspond to a GNS with 25 nm core diameter and 8 tips, all of them 19 nm in length and 13 nm in width. Simulations at the bottom correspond to a GNS with a 20 nm core diameter and 8 tips, all of them 22 nm length and 10 nm width. Figure reproduced with permission from Reference 122.

Figure 7(c) includes the extinction, absorption and scattering cross section spectra of hollow gold nanocages (HGNCs). Hollow metallic nanoparticles differ from the already described GNSs, GNRs and GNSs in the fact that metal is only present at the surface. These nanoparticles were initially proposed to be used as drug deliverers, as their inner volume could act as a drug reservoir. Once a given nanoparticle (previously filled with the drug to be delivered) is incorporated into the cell, drug release will be achieved by irradiating at its surface plasmon resonance. By this way, the high local temperatures would “open” the structure, thus releasing the drug by either light-induced metal melting or by temperature-induced changes in the polymer structure surrounding the nanoparticle. Nevertheless, the light-to-heat conversion efficiency was found to be high enough to use these hollow gold nanoparticles as thermal agents for photothermal treatments. From a practical point of view, HGNCs have the advantage that their optical properties can be strongly modified by slight changes in their morphology. In order to illustrate this property, **Figure 6(c)** shows how the extinction spectra of 30 nm (edge length) Au/Ag metallic nanocages can be tuned from the visible to the NIR as their dimensions (controlled by the Au/Ag relative composition) are modified.¹¹³ The surface plasmon peak is red shifted by increasing the HAuCl₄ content that is used in the galvanic replacement of the Ag template. This allows for a fine spectral tuning from the visible (450 nm, when

no Au is present) to the near infrared (900 nm for a 1.4 ml volume of 0.2 mM HAuCl₄ /water solution). Moreover, the relative magnitude of absorption and scattering components can also be changed by varying the cage size.¹²⁴

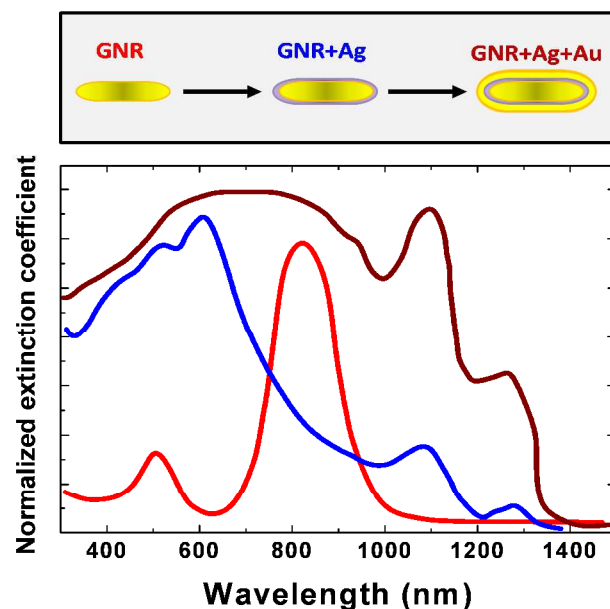


Fig. 10 Top row shows a schematic representation of the approach followed by Min-Fong Tsai et al. for the development of a single metallic nanoparticle capable of optical absorption in the first and second biological windows. Bottom graph includes the optical extinction spectrum of the synthesized nanoparticle at the different preparation stages represented at the top. Figure reprinted (adapted) with permission from M. F. Tsai, S. H. Chang, F. Y. Cheng, V. Shanmugam, Y. S. Cheng, C. H. Su and C. S. Yeh, ACS Nano, 2013, 7, 5330-5342. Copyright (2013) American Chemical Society.

Very recently, new types of gold nanostructures intended to display absorption in both the first and the second biological windows have been synthesized.¹²⁵ This is not an easy task because, as was explained before, the spectral position of the extinction peak is unequivocally determined by the geometry and size of the metallic NP. Therefore, broad absorption bands require a combination of multiple geometries in a single nanoparticle. An interesting approach has been recently proposed by Min-Fong Tsai et al,¹²⁵ which is schematically shown in **Figure 10** (top). They were able to synthesize single all-metallic nanoparticles composed of nanostructures with different geometries, starting from single GNRs with a plasmon resonance wavelength close to 800 nm (corresponding to GNRs with aspect ratio and average length close to 3 and 50 nm, respectively). This “seed” GNRs were then coated with a thin Ag layer (2-7 nm). The presence of this thin Ag layer enhances the visible part of the extinction spectrum of the starting GNRs, as it can be seen in **Figure 10** (bottom). In order to extend the extinction spectrum to the second biological window (1-1.4 μm) the Ag+GNR structure was finally coated with a gold shell (close to 4 nm in diameter). This shell extended the extinction spectrum up to 1400 nm, as it can be observed in **Figure 10** (bottom). Very interestingly, Min-Fong Tsai et al.¹²⁵ also reported on a fine control over the optical properties of the final nanostructure by just varying the Ag gap

thickness between the GNR and the outer Au shell. Indeed, this opens the possibility to perform photothermal therapy at any desired wavelength between 400 and 1400 nm. In respect to complex geometries involving gold nanoparticles, it should be noted that some groups have been able to synthesize encapsulated gold nanoparticles and demonstrated simultaneous imaging and heating by incorporating gold nanoparticles in different types of micro-capsules.¹²⁶⁻¹²⁹

Note that, up to now, this section has been mainly devoted to the description of gold nanoparticles. Nevertheless, the presence of a plasmon resonance is expected to occur for any metallic nanoparticle and not only for Au nanoparticles. Indeed, there are several works reporting on the optical properties of Ag nanoparticles. As a matter of fact, S.C. Boca et al.¹³⁰ reported on the synthesis of water-dispersible silver nanoprisms with a triangular section that showed an intense extinction band at around 800 nm.¹³⁰ These nanoparticles showed high biocompatibility and low intrinsic toxicity. In addition, they demonstrated that these NPs displayed an outstanding efficiency as photothermal agents under optical excitation at 800 nm.

Geometry	Dimensions (nm)	$\sigma_{\text{ext}} \text{ cm}^2$	Φ_{abs}	$\sigma_{\text{abs}} \text{ cm}^2$	$\sigma_{\text{cat}} \text{ cm}^2$	Reference
GNRs	8±1 nm width 29±5 nm length	4.5·10 ⁻¹¹	0.95	4.3·10 ⁻¹¹	2.0·10 ⁻¹²	206
GNSs-I	38±4 nm core 9±3x46±6 nm lobes	4.4·10 ⁻¹¹	1	4.4·10 ⁻¹¹	0	206
GNCs	47±3 nm edge 4±1 wall thickness	50·10 ⁻¹¹	0.63	3.1·10 ⁻¹⁰	1.9·10 ⁻¹⁰	206
GNShs	120±5 nm SI-core 10±1 nm shell	15·10 ⁻¹¹	0.68	10·10 ⁻¹¹	5.0·10 ⁻¹¹	206
Rhodamine6G	Molecular	7.2·10 ⁻²¹	-	-	-	93
Malachite Green	Molecular	9·10 ⁻²¹	0.03	2.34·10 ⁻²²	8.76·10 ⁻²¹	162
CdX(X=S,Se,Te)	R=2	1.8·10 ⁻¹⁹	0.14	2.52·10 ⁻²¹	1.55·10 ⁻²⁰	166
Carbon nanotubes	R=0.6, L=150	4.74 x 10 ⁻¹⁹	0.5	2.37 x 10 ⁻¹⁹	2.37 x 10 ⁻¹⁹	166
Copper selenide	R=8	4.62 x 10 ⁻¹⁸	0.22	1.02 x 10 ⁻¹⁸	3.60 x 10 ⁻¹⁸	166
Organic dye	Molecular	4.52 x 10 ⁻¹⁵	-	-	-	34

Table I. Spectroscopic characteristics of the different nanoparticles and nanostructures discussed all along the text.

Before closing the description of the optical properties and heating mechanisms of metallic nanoparticles we would like to mention the relevant case of the so-called prussian blue nanoparticles (PB-NPs).¹³¹ These are nanoparticles made of mixed-valence transition metal hexacyanoferrates with the general formula of $\text{Fe}^{\text{III}}_4[\text{Fe}^{\text{II}}(\text{CN})_6]_3\text{H}_2\text{O}$ that were extensively used in the past as efficient dyes. Very recently, Guanglei Fu et al., have been demonstrated that these NPs are efficient photothermal agents under infrared optical excitation.¹³¹ PB-NPs present optical properties very similar to Gold Nanorods showing an intense absorption band at around 800 nm. This absorption band, at variance with GNRs, it is not related to the excitation of any surface plasmon resonance but it has been tentatively attributed to the charge transfer transition between Fe(II) and Fe(III) in PB-NPs. Despite the exact origin of this absorption band, it has been demonstrated that under infrared optical excitation PB-NPs were able to convert efficiently optical radiation into heat. As a matter of fact, Guanglei Fu et al. managed to report successful in vitro photo-thermal therapies.¹³¹ When compared with other heating NPs, PB-NPs show the additional advantage of a high photo-chemical stability, low manufacturing costs and a clinically tested and approved bio-safety.^{132, 133}

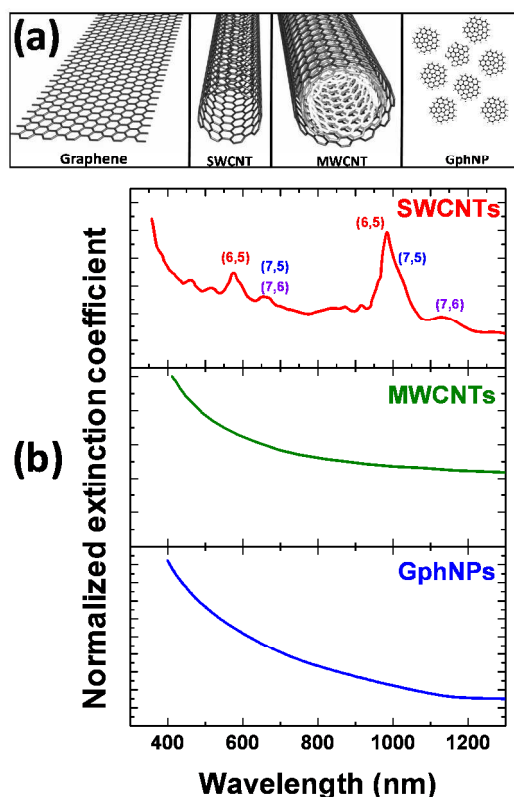


Fig. 11 (a) Schematic drawing of the basic geometries of different carbon-based nanoparticles used for photothermal applications. Images extracted from Reference 171. (b): Room temperature extinction cross sections of single-walled and multi-walled carbon nanotubes (SWCNTs and MWCNTs, respectively) and of graphene oxide nanoparticles (GphNPs). Figure (a) reprinted (adapted) with permission N. H. Levi-Polyachenko, E. J. Merkel, B. T. Jones, D. L. Carroll and J. H. Stewart, *Molecular Pharmaceutics*, 2009, 6, 1092-1099. Copyright (2009) American Chemical Society. Data for Figure (b) extracted from References 139 and 144.

B.II. Carbon nanostructures

As for the case of metals, light-induced heating of carbon-containing materials is also a well-known effect with numerous examples and applications. During the last few years, and due to the fast development of the required synthesis techniques, a number of carbon-based nanomaterials have been successfully developed. From the very beginning, these carbon-based nanoparticles were considered excellent candidates for biological applications, due to the intrinsic biocompatibility of carbon. Carbon-based nanostructures can be divided in two main groups: nanodiamonds and graphite related structures. Nanodiamonds have great relevance for biomedical applications, particularly as luminescent biomarkers capable, for example, of intracellular high resolution tracking.¹³⁵ In addition, very recently, nanodiamonds have been proposed as excellent nanothermometers that can even be used for thermal imaging of single cells.¹³⁶ Nevertheless, for the purpose of photothermal applications, nanodiamonds have not shown remarkable light-to-heat conversion efficiencies. For such applications, graphite-related carbon-based nanostructures have shown remarkably higher light-induced heating.

The simplest graphite-related structure is called graphene, which is simply a bidimensional graphite plane (see **Figure 11 (a)**). However, the most developed carbon-based nanostructures are carbon nanotubes (CNTs, see also **Figure 11(a)**). These nanostructures, discovered by Ijima and coworkers in 1991,¹³⁷ are cylinders made of sheets of graphene which are rolled in a tube shape with characteristic diameters in the range of few nanometers and lengths that may vary from tens of nanometers up to a few microns. The rolling can be made at different angles (“chiral” angles) and curvatures. Thus, there is a tremendous variety of geometries that results in a variety of CNT types, each one leading to different physical, mechanical, electrical and optical properties. In fact, slight changes on the geometrical structure of each individual nanotube can result in significant changes in its electronic structure. The structure of each individual CNT is determined by its diameter and the relative orientation of the graphene basic hexagons with respect to the axis tube. Each CNT is usually identified by two integers (n,m) that determine the so called “chiral vector”. The importance of this (n,m) vector is that it does determine both the electronic and optical properties of the CNT. For instance, depending on the (n,m) indices, the CNT could have either metallic or semiconducting character, depending on the existence or absence of a forbidden energy gap between the valence and conduction bands. In general, the synthesized carbon nanostructures are mixtures of different individual chiralities, i.e. a mixture of non-identical CNTs with different (n,m) indices. As a consequence, typical colloidal solutions of CNTs cannot be classified as metallic or semiconducting but as a mixture of both. Indeed, the so called single-walled carbon nanotubes (SWCNT), that should ideally be constituted by a given chirality (n,m), are considered as synthesized with a clear predominant chirality. However, even these simplest nanostructures can display both metallic and semiconductor properties due to the presence of slightly different geometric deviations of the major (n,m) CNTs. The existing technologies for the production of SWCNTs are often tedious,

low in yield and with low purity. It is nowadays known that the synthesis of nanoparticles consisting of collections of concentric CNTs is much easier and allows for mass production with reduced manufacturing costs. These nanoparticles are commonly denoted as multi-walled carbon nanotubes (MWCNTs) (see **Figure 11(a)**). Finally, several recent works have pointed out the possible use of graphene nanoparticles (GphNPs), constituted by single graphene layers with total areas in the order of few nm² (see also **Figure 11(b)**), with outstanding absorption properties in the near infrared (NIR)^{138, 139}.

Typical extinction spectra of the three main carbon nanostructures used for photothermal therapy are also shown in **Figure 11(b)**. In general, the extinction spectra corresponding to SWCNTs are rich in features, as they consist of several absorption peaks superimposed over a wavelength decreasing background. These peaks correspond to different “Van Hove transitions” for the involved (n,m) nanotubes (see **Figure 11(b)**).¹⁴⁰⁻¹⁴² Each Van Hove peak is a transition between two singularities in the density of states of a given (n, m) nanotube. For instance, in **Figure 11(b)**, the main peaks at about 550 and 1000 nm correspond to two different transitions of the (6,5) predominant nanotubes in that particular solution. Since the (n,m) indices of SWCNTs are unequivocally given by the particular diameter and chirality of the CNTs, from the position of the Van Hove peaks it is possible to elucidate on the particular geometric and structural properties of the SWCNTs. Indeed, optical extinction spectra are commonly used to characterize the geometric and structural properties of the SWCNTs present in a given solution. The additional peaks that appear in **Figure 11** occur as a result of a distribution of diameters around that of the main (6,5) CNTs. At shorter wavelengths (below 600 nm), the rise in the extinction spectrum is mainly related to the contribution of the so-called π plasmon resonance.¹⁴³ This plasmon is related to π bonds between carbon atoms and arises from a light-induced collective charge motion, so the name of π plasmon. Indeed, the presence of this plasmon band is identified as one of the mechanisms leading to the background in the extinction spectra of CNTs. As will be stated later, this background is partially responsible for light-to-heat conversion in CNTs.¹⁴⁴ The presence of Van Hove extinction singularities depends not only of the morphology and structure of the CNTs but also on its aggregation state within the colloidal solution. Indeed, M.J. O’Connell et al. demonstrated how the aggregation of nanotubes into bundles quenches the fluorescence (through interactions with metallic tubes) and broadens the absorption spectra in such a way that identification of Van Hove singularities becomes difficult.¹⁴⁵

The extinction spectra corresponding to MWCNTs and GphNPs in the visible-infrared ranges are somehow similar but simpler than those corresponding to SWCNTs (see **Figure 11(b)**). Essentially, they consist of an extinction background that extends from visible to infrared, whose intensity monotonously decreases with wavelength. In these cases, the extinction peaks due to specific (n,m) nanotubes have disappeared. In the case of MWCNTs, the non-observance of (n,m) peaks is due to the inherent large dispersion in both radius of curvature and relative orientation of the carbon hexagons with respect to the axis tube. In addition, bundling (that difficulties the observation of Van

Hove singularities) is usually present in the solutions of MWCNTs due to their characteristic large lengths.¹⁴⁵

Light-to-heat conversion in CNTs is due to de-excitation processes between Van Hove states, that involve luminescence or non-radiative relaxation. According to this simple model, once a CNT is illuminated it could generate, simultaneously, heat and luminescence. The relative contribution of any of these two de-excitation channels (heat and photoluminescence) is given by the fluorescence quantum yield (QY). In the case of CNTs, fluorescence is efficiently quenched by the interaction between different carbon layers or between carbon layers and other materials (such as substrates or other nanoparticles). The fluorescence QY of SWCNTs is typically below 1% and only when special strategies are adopted to improve isolation of individual CNTs in solution, this yield can exceed 10%.¹⁴⁶⁻¹⁴⁸ As a consequence, and especially in the case of MWCNTs, it can be assumed that all the absorbed energy is transformed into heat. In addition to this heating mechanism, heat in CNTs is also thought to be related to the light-induced collective motion of free carriers, i.e. to the excitation of the π plasmon. In this case, heating mechanism is explained similarly to the case of gold nanoparticles, i.e. heat is produced by the relaxation of surface currents through heat generation.¹⁴⁹

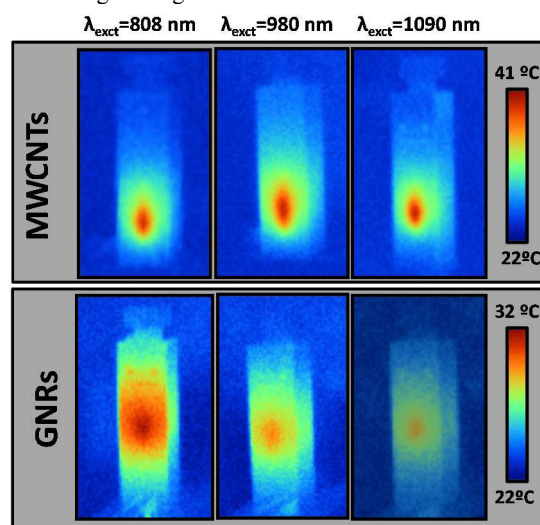


Fig. 12.- Top Thermal images of a cuvette containing an aqueous solution of MWCNTs under laser excitation at 808, 980 and 1090 nm. **Bottom.-** Thermal images of the same cuvette containing an aqueous solution of GNRS with a surface plasmon resonance wavelength close to 808 nm. The laser intensity was set to 1.4 W/cm² in all cases. Adapted with permission from Ref. 106 from The Royal Society of Chemistry.

From **Figure 11(b)** it is clear that, independently of their particular geometry, carbon-based NPs show significant extinction (absorption plus scattering) along the whole biological spectral range (i.e. for wavelengths above 700 nm). Thus, in principle, carbon-based NPs present the advantage of tunable photothermal therapy in a wide spectral range. This is at variance with the case of metallic nanoparticles for which the spectral position of the plasmon resonance is determined unequivocally by their particular geometry (see **Section B.I**), so that heat generation is only produced when they are excited within a restricted spectral range. The ability of CNTs for heat generation under illumination in a wide spectral range is evidenced in

Figure 12 (top), which shows thermal images of an aqueous solution of MWCNTs optically excited at three different infrared wavelengths within the biological windows. As can be observed, although the excitation wavelength has been changed by more than 300 nm, the light induced heating in the solution is almost the same. On the contrary the same experiments but performed in a solution containing GNRS, indicate that the magnitude of the induced heating is strongly wavelength dependent.¹⁰⁶

As it was previously discussed, the ability of any nanosized system as photothermal agent depends on their absorption efficiency. For CNTs, the absorption efficiency has been determined following different approaches conducted by different research groups.¹⁵⁰⁻¹⁵² For the case of SWCNTs, the absorption efficiency has been reported to be strongly dependent on the particular solvent in which they are dispersed. As an example, the absorption efficiency of SWCNTs dispersed in toluene or in chloroform is close to 100 % whereas it goes down to almost 50% when they are dispersed in DCB (C₆H₄Cl₂).¹⁵² For the case of MWCNTs (in water), the absorption efficiency has been determined by quantum dot fluorescence thermometry under different conditions. It was concluded that their absorption efficiency was almost wavelength-independent and close to 50% (see also **Table I**).¹⁰⁶ At this point, the higher absorption efficiency of SWCNTs over MWCNTs would make them more appropriate for photothermal treatments. However, previous works have pointed out the absorption coefficient (per particle) of MWCNTs is approximately 3 times that of SWCNTs. This is mostly because the former ones have more electrons available for absorption per particle and possess greater mass.¹⁵³ When compared to the absorption efficiency of GNPs (usually close to unity for infrared plasmons), MWCNTs show a reduced absorption efficiency, i.e. a larger contribution of scattering to the overall optical extinction. Despite their lower absorption efficiency, it should be noted that the absorption cross section of CNTs is in the range of 10⁻¹¹ cm² per particle.^{154, 155} This value (see **Table I**) is comparable to that of GNPs, but it is important to remark that CNTs present the advantage of broad spectral tunability for excitation.

In respect to GphNPs there is not, up to the best of our knowledge, any study reporting neither on their absorption cross section nor on their absorption efficiency. Nevertheless, in this case the relative contribution of scattering is expected to be smaller due to their reduced size, and so larger absorption efficiencies are predicted.

B.III. Quantum Dots

Quantum dots (QDs) are semiconductor nanosized crystals that have been intensively used for fluorescence bioimaging. A number of direct band gap semiconductors, such as CdSe, CdS, CdTe, InP and PbSe, are efficient emitters when optically excited in the visible (via inter-band transitions across the band gap) or in the infrared (above 800 nm) via multi-photon absorption.¹⁵⁶ Fluorescent QDs have successfully been used for high-contrast, low autofluorescence *in vitro* and deep tissue *in vivo* imaging.¹⁵⁷ Despite the serious concerns about their intrinsic toxicity,¹⁵⁸ recent works related to experiments carried out in small animals, have revealed that when an appropriate surface treatment is performed, QDs have negligible toxicity.¹⁵⁹ The optical properties of QDs are determined by the host semiconductor type

material and its size, which gives rise to quantum confinement effects. The size dependence of optical properties of QDs not only allows for tailoring the emission wavelength (from the visible to the infrared) but also for using the fluorescent QDs as multifunctional fluorescent probes capable, for example, of intracellular thermal sensing during hyperthermia treatments.¹⁶⁰

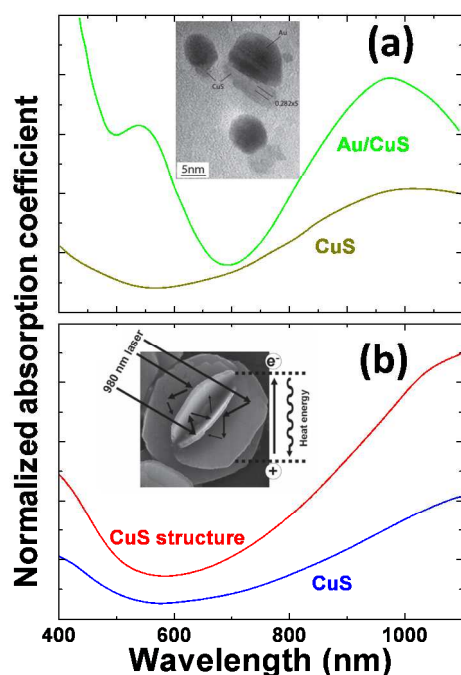


Fig. 13 (a) Extinction spectra of CuS QDs and Au/CuS nano structures (as those shown in the inset). (b) Extinction spectra of CuS QDs and of CuS super-nanostructures (flower-like CuS superstructures as those included in the inset). Figure reproduced with permission from References 161 and 162.

Among the great variety of fluorescent QDs, copper-based semiconductors attracted great attention at early stages as biocompatible Cd-free fluorescent probes for *in vivo* imaging applications.¹⁶³ Importantly, for the purpose of this review, Cu-based QDs (mainly CuSe and CuS) show an extinction spectrum constituted by two broad bands, one of them centered in the UV-visible spectral range and the other one with a maximum at about 980 nm (see, for example the extinction spectra of CuS QDs included in **Figure 13**). The origin of this infrared band has given rise to some controversy. Whereas some authors relate this extinction band to inter-band electronic transitions,^{161, 162, 164, 165} others correlate it to a broadband carrier absorption (due to a high concentration of vacancies) that results in a surface plasmon resonance.^{166, 167} Thus, Cu-based QDs would display absorption features similar to those of metals.¹⁶⁸ Independently of the origin of this absorption band, many research groups have corroborated that when Cu-based QDs are optically excited, substantial heating is produced due to phonon-assisted electronic decay or to relaxation of free-carrier surface currents. The extinction cross sections of Cu-based QDs in the infrared have been determined to be close to $8 \cdot 10^{-14}$ and $28 \cdot 10^{-14}$ cm^2 for CuS and CuSe QDs respectively.^{164, 166} These are orders of magnitude larger than those expected for an indirect optical transition and considerably higher than those of direct band gap semiconductor quantum dots. This fact supports the plasmonic origin of the 970 nm extinction

band.¹⁶⁶ When compared to CNTs or GNPs (see **Table I**), Cu-QDs show extinction cross sections several orders of magnitude smaller. Indeed, this is a limiting factor, so research is currently focusing on the synthesis of novel Cu-QDs structures with enhanced extinction cross sections. Two of these approaches are summarized in **Figure 13**. S. B. Lakshmanan and coworkers managed to synthesize Au/CuS nanocomposites constituted by a CuS core partially surrounded by an Au shell (see inset in **Figure 13(a)**).¹⁶¹ As can be observed in this figure, the extinction coefficient of CuS-QDs at 970 nm is enhanced about 2 times for Au/CuS due to plasmonic-induced local field enhancement. An alternative approach to improve the infrared absorption of Cu-QDs was introduced by Q. Tian et al., who demonstrated that multiple reflection of 980 nm laser radiation in CuS-QDs with complex morphologies (such as the so-called flower-like CuS superstructures shown in **Figure 13(b)**) could lead to a remarkable enhancement in the 970 nm extinction cross section.¹⁶²

Another strategy to deliver heat through quantum dots is to use indirect band gap semiconductor materials. In this case, the maximum in the valence band and the minimum in the conduction band are displaced in k-space (they are at different positions in the momentum axis, as is schematically represented in the inset of **Figure 14**). Radiative transitions in these systems require the interplay between phonons and photons. Consequently, they are inefficient emitters, displaying large non-radiative rates. This is, for example the case of water-soluble germanium QDs (Ge-QDs), whose extinction spectrum is shown in **Figure 14**. Indeed, Ge-QDs have been proven to be capable of efficient heat generation after optical excitation in the near infrared.¹⁶⁹ The available literature on the use of Ge-QDs as photothermal agents is very limited, despite the fact that pioneer works claimed that the light-to-heat conversion efficiency could be comparable or even larger than that of GNPs.¹⁶⁹ Nevertheless, a systematic investigation on the absorption efficiency of Ge-QDs is not available at the present time, so that a direct comparison with other NPs in terms of absorption cross sections is not possible.

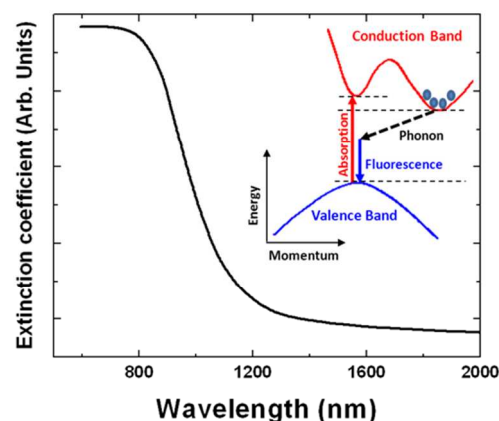


Fig. 14 Extinction spectrum of Germanium QDs as reported by T.N. Lambert et al. Inset shows an schematic representation of the energy bands of Germanium QDs. Solid arrows indicate absorption and luminescence events whereas dashed arrows indicate phonon generation and represent the heating channels. Figure reproduced with permission from Reference 169.

B.IV. Rare earth doped nanocrystals

Rare earth doped nanocrystals (RE:NPs) have been emerging over the last years as very promising fluorescent nanoprobes with numerous applications in modern bioimaging ranging from *in vitro* and *in vivo* fluorescence imaging to intracellular thermal sensing.¹⁷⁰⁻¹⁷⁴ Due to their particular electronic configuration, rare earth ions usually present a rich energy level diagram.¹⁷⁵ Therefore, the incorporation of this kind of ions into dielectric materials leads to the appearance of energy levels in the band gap. This, in turn, leads to the appearance of narrow absorption lines (bands) corresponding to optically stimulated electronic transitions from the ground state to the excited states, as can be observed in the extinction spectrum of NdF₃ nanoparticles included in **Figure 15** (top). In this case, Nd³⁺ ions appear as a constituent ion of the material not as a dopant.^{175, 176} Upon irradiation with an appropriate wavelength, electrons are optically excited from the ground state up to any of the excited states. Then, they relax back to the ground state involving different (radiative and non-radiative) processes that could result in heat generation. In order to illustrate and describe these processes, **Figure 15** includes a schematic diagram of the different radiative and non-radiative processes undergone by Nd³⁺ ions after optical excitation with 808 nm wavelength radiation. The case of Nd³⁺ has been selected since these ions show a reasonable light-to-heat conversion. When Nd³⁺-doped NPs are excited with an 808 nm laser beam, electronic transitions from the ground state up to the ⁴F_{5/2} excited state are stimulated, after which a fast non-radiative de-excitation process down to the metastable ⁴F_{3/2} state takes place. Once in this metastable state, neodymium ions can undergo a radiative decay to anyone of the lower energy states, from which phonon-assisted final decays to the ground state take place. Since heat is generated in each non-radiative de-excitation (i.e. with each phonon-assisted relaxation), neodymium ions are expected to partially convert the 808 nm excitation energy into heat. The relaxation dynamics in RE:NPs become more complicated when the rare earth ion content is increased. In this case, the distances between neighboring RE ions are reduced so that ion-ion interactions are activated. This leads to the appearance of both cross relaxation and energy migration processes, which are schematically represented in **Figure 15** (bottom). In the first case, de-excitation from the metastable state is achieved by promoting two Nd³⁺ neighboring ions from their ground state up to the ⁴I_{15/2} state. Once both ions are at the excited state, they de-excite down to the ground state by a multi-phonon relaxation process (i.e. delivering heat), known as “cross relaxation”. In the second case, energy migrates among Nd³⁺ neighboring ions until a non-radiative center (killer) releases the migrated energy, usually by heat generation. According to the schematic representation of **Figure 15** (bottom), it is clear that RE:NPs with high ion concentrations are expected to convert a significant fraction of the absorbed radiation into heat. Such light-to-heat conversion has already been observed in NPs doped with either Neodymium or Ytterbium/Erbium ions.¹⁷⁷⁻¹⁷⁹ Despite the fact that laser-induced heating in RE:NPs has proven to be a relatively efficient process, no attempts to use them as photo thermal agents in bio-systems have been made up to now. In the case of heavily doped RE:NPs the fluorescence quantum yields (QY) have been reported to be very low (below 0.2 for the case of

heavily Nd³⁺ ion doped nanocrystals),¹⁸⁰ indicating that a large percentage of the absorbed (optical) energy is transformed into heat. Nevertheless, the limiting factor of RE:NPs as photothermal agents resides in the relative low absorption cross sections of RE³⁺ ions. Indeed, for the case of colloidal solutions of neodymium-doped NPs, the absorption bands are hard to be measured, so a direct estimation of the absorption cross section per NP is not possible. For a first order estimation, we refer again to Nd³⁺ ions and recall the fact that the absorption cross section per ion is typically close to 10⁻²⁰ cm². The absorption cross section per NPs could be obtained multiplying this by the number of neodymium ions inside a single NP. Assuming, for instance, a 20 nm diameter NaYF₄ NP, this can be calculated from the NP volume ($\approx 10^{-22}$ m³), the unit cell volume ($\approx 1 \cdot 10^{-28}$ m³) and roughly considering that each unit cell contains a neodymium ion. This estimation concludes that the number of neodymium ions per NP is in the order of 10⁶, so that the absorption cross section per NP can be assumed to be of the order of 10⁻¹⁴ cm², i.e. several orders of magnitude lower than those of GNPs and CNTs but comparable to those of QDs (see **Table I**).

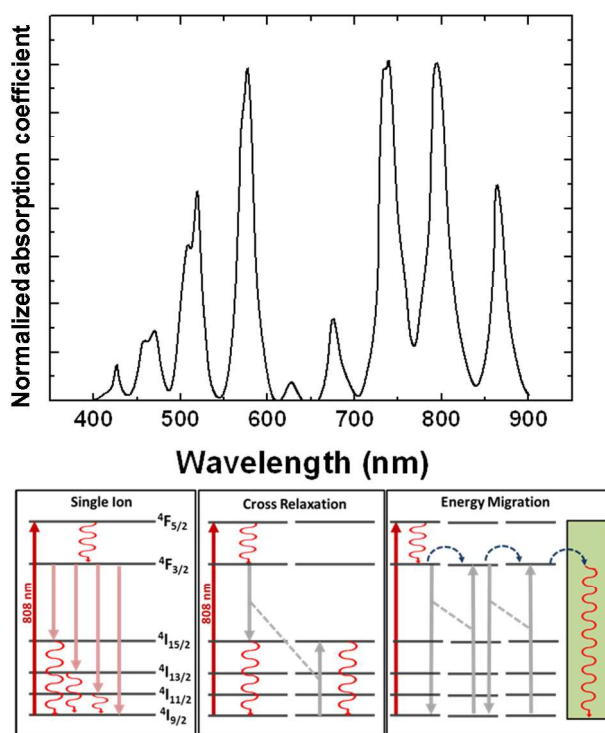


Fig.15 Top Normalized, to maximum, absorption cross section of NdF₃ nanoparticles. **Bottom.-** Schematic representation of the energy level diagram of neodymium-doped nanoparticles. Straight arrows indicate radiative excitations and de-excitations. Wave arrows represent non-radiative de-excitations. Figure reproduced with permission from Reference 176.

B.V. Porous Silicon

Porous silicon (PS) is a synthetic material that can be easily synthesized by electrochemical etching (anodization) of silicon, using a simple electrochemical cell.¹⁸¹ PS has effective band gap energies ranging from 1.12 eV up to 2.5 eV due to quantum confinement effects, associated to the non-homogenous distribution of pores.¹⁸² Moreover, PS has been found to be of

great potential for bio-imaging applications,¹⁸³ mainly due to the fact that silicon is a common trace element in humans and that a primary biodegradation product of porous Si, orthosilicic acid, is the form predominantly absorbed by humans and is naturally present in numerous tissues.¹⁸⁴ In addition, their surface allows for easy and efficient functionalization with therapeutic agents.^{185, 186} All these properties make PS a promising material for bio-applications. Thus, current research is focused on the synthesis of PS nanoparticles (PSNPs), including all these beneficial properties for application in biology. Indeed, PSNPs have already been used as high-brightness biodegradable luminescent nanoparticles for *in vivo* experiments.^{187, 188} The first example of *in vivo* imaging of a tumor, and other organs, using biodegradable silicon NPs in live animals were carried out by Ji-Ho Park et al.¹⁸⁷ They tested biodegradability and biocompatibility of PSNPs showing, first, the accumulation of PSNPs mainly in the liver and the spleen. However, the PSNPs accumulated in the organs are noticeably cleared from the body within a period of 1 week and completely cleared in 4 weeks. The mechanism of clearance is attributed to degradation into soluble silicic acid followed by excretion.¹⁸⁷

In addition, PSNPs have also been demonstrated to provide significant light-to-heat conversion efficiencies.¹⁸⁹ The mechanism of the photothermal effect in PS is similar to that of crystalline silicon and other semiconductors. When optical absorption takes place, pairs of charge carriers are generated, which diffuse through the material. Each carrier gains an energy approximately equal to the band gap of the material. This energy is delivered by electron-hole recombination, causing a local heating of the lattice and, therefore, in the surroundings. Thus, PSNPs have been reported as non-toxic therapeutic agents that generate heat to irreversibly destroy cancer cells when exposed to NIR light.^{184, 189, 190} As PS has atomic and electronic structures similar to those of CNTs, PSNPs are expected to show similar heating efficiencies. An additional advantage of porous silicon-based nanoparticles is that their absorption coefficient is expanded over the whole spectral window allowing for the use of appropriate NIR laser sources to avoid significant collateral damage.¹⁹¹

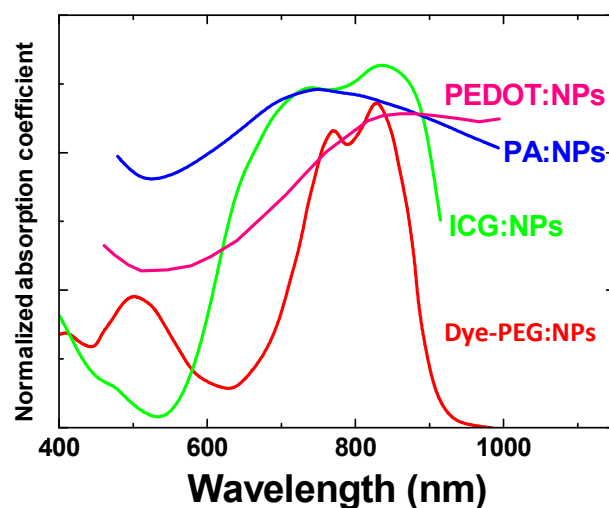


Fig. 16 Extinction spectra corresponding to colloidal solutions of different organic NPs which have been demonstrated to be efficient photothermal agents. Data extracted from References 105, 192 and 193.

B.VI. Organic Nanoparticles

All the above-described nanoparticles have shown high photothermal efficiencies but they display, as a common drawback, their inorganic nature. This means that they are non-biodegradable, and likely to be retained in the body for long periods of time, preventing their further application in real clinical treatments due to potential long-term toxicity concerns.¹⁹⁴

Organic nanoparticles, typically polymeric ones, have been traditionally used in nanomedicine as drug delivery carriers. Light-absorbing organic nanoparticles have very recently attracted great attention as photothermal agents because of the pioneering demonstration of light-to-heat conversion in polyaniline conductive polymers and in porphyrin organic nanoparticles.^{110, 193} These pioneer works motivated the research of novel organic nanostructures with improved properties. In particular, in order to avoid excessive collateral heating due to tissue absorptions in the visible, a great effort has been carried out in the synthesis of organic NPs with enhanced absorption in the near infrared (NIR). In this respect, Indocyanine Green (ICG) based nanoparticles are of special relevance. ICG is a FDA-

approved substance for a number of clinical imaging applications that, simultaneously, shows an appreciable light-to-heat conversion efficiency.¹⁹² In order to overcome some drawbacks of ICG (low metabolization rate, negligible absorption from intestine and poor intrabody recirculation)¹⁹⁵ several approaches have been proposed. A very interesting one is that proposed by Jie Yu et al., who encapsulated ICG in a ~120 nm structure coated with antibodies through an all-water synthesis route.¹⁹²

The resulting ICG-based nanostructures (ICG:NPs) showed remarkable absorption in the NIR (see **Figure 16**) and were successfully used for cell targeting and for photothermal damage of cancer cells by NIR excitation at 808 nm. Other approaches allowing the use of ICG as photothermal agent are based on more complex structures, such as those proposed by M. Zheng et al.¹⁹⁶ They synthesized complex NPs consisting of a core formed by a mixture of doxorubicin (DOX) and ICG surrounded by a poly(lactic-co glycolic acid) (PLGA)-lecithin-polyethylene shell. These complex nanostructures, also showing optical absorption in the NIR, served as dual-functional agents capable of simultaneous chemo- and photothermal therapy. Recently, attention has been given to the use of biological materials as platforms for the delivery of therapeutic or imaging agents. As an example, the research group of B. Anvari reported the use of genome-depleted plant infecting bromo mosaic virus doped with ICG as a nanoconstruct for NIR fluorescence and photoacoustic imaging.^{197, 198}

In addition, the first successful engineering of hybrid nanoscale constructs derived from membranes of hemoglobin-depleted erythrocytes that encapsulate the near infrared chromophore, indocyanine green were carried out by Bahmani et al. They show the utility of the constructs as phototheranostic agents in fluorescence imaging and photothermal destruction of human cells.¹⁹⁹ Other authors developed efficient heating agents by loading ICG into SPIO nanoparticles with phospholipid-PEG coating that have been demonstrated to be specially suitable for dual-modal imaging and photothermal therapies.²⁰⁰

In addition to the encapsulated ICG based nanoparticles, some groups have proposed other chemical organic species as

photothermal agents. For instance, polyaniline-based NPs (PA:NPs) have been satisfactorily employed as photothermal agents for efficient photothermal treatment of epithelial cancer.¹⁹³ From the photophysical point of view, a key advantage of PA:NPs is that dopants (i.e., strong acids, Lewis acids, transition metals and alkali ions) for protonation generate an interband gap state (between valence and conduction bands) that induces the movement of electrons and decreases the excitation-energy level.^{201, 202} As a consequence of the presence of such inter-band states, optical transitions occur at low photon energies and, consequently, optical absorption bands appear in the NIR (see **Figure 16**). These NPs also present good colloidal stability in water, but their NIR absorption depends on the pH value as well as on the presence of oxidative species in the intracellular environment. Thus, the possibility to be applied to different types of cancer is still pending of further investigations.

Very recently, organic NPs based on conductive polymers (PEDOT:PPS and polypyrrole) have successfully demonstrated their photothermal properties at low power densities.¹⁰⁵ The required optical powers for efficient tumor treatment are similar or even lower than those employed with gold nanoparticles, suggesting a similar light-to-heat conversion efficiencies. These organic nanoparticles, whose typical size is below 100 nm, show a strong absorbance in the infrared. Since both PEDOT:PPS and polypyrrole are conductive polymers, their heating mechanism is very likely related to the relaxation of light induced carrier currents. **Figure 16** includes, for the sake of comparison, the extinction spectrum of PEDOT:NPs as reported by L. Cheng et al.¹⁰⁵

The work recently published by L. Cheng et al. should be also mentioned, as these authors present a novel and smart approach. In this case, the photothermal agent was constituted by an infrared absorbing dye encapsulated by a PEG shell. This shell provides both colloidal stability as well as biocompatibility.²⁰³

The resulting nanoparticles (Dye-PEG:NPs) show a broad extinction band (see **Figure 16**) and a completely quenched fluorescence, close to the noise level. This quenching is very likely caused by non-radiative interactions between dye molecules inside the PEG core. These nanoparticles displayed no observable toxicity to three cell lines at the tested concentrations. Moreover, they were not found to be noticeably toxic during *in vivo* experiments.²⁰³ In these NPs, the heating mechanism is related to the complete relaxation of the absorbed optical power via multiphonon relaxation, as no luminescence is generated by the dye.

The photothermal capability of organic nanostructures is usually limited by their relative low absorption coefficient. For organic-based nanostructures, extinction cross sections have been estimated to be of the order of 10^{-14} cm² (see **Table I**).^{34, 204} This drawback can be overcome by using porphyrins based NPs (PPH:NPs).^{110, 205} PPH:NPs are self-assembled from porphyrin lipid into liposome-like nanoparticles (~100 nm diameter). The porphyrin packing density per particle is very high, so they absorb light with extremely high efficiency. As the packing density also induces self-quenching of luminescence from the porphyrin excited states, the absorbed energy is mostly released as heat, providing exceptional properties as photothermal agents. The absorption cross section of PPH:NPs has been estimated to

be close to $1 \cdot 10^{-11}$ cm, i.e. comparable to that of metallic NPs²⁰⁶ (see **Table I**).^{110, 205} Good results have been also obtained by using Polypyrrole nanoparticles that have been demonstrated to provide high photothermal conversion efficiencies during photothermal ablation of cancer cells.^{207, 208}

Finally, it is necessary to mention here that Yan Ma et al. have been also reported on the synthesis of highly efficient heating nanoparticles constituted by gold coated organic nano micelles that can be used as multi-functional nanoparticles capable of magnetic and optical contrast agents.²⁰⁹

C. Synthesis and morphology

In this section, a general overview of the different procedures developed up to now for the synthesis of L-HNPs is given. As it is described in Section B, there are several families of NPs capable of efficient light to heat conversion. Each family can be synthesized by using several synthesis procedures although not all lead to the same results. In the next paragraphs we will summarize those methods that have shown the best results in terms of the synthesis of HNPs.

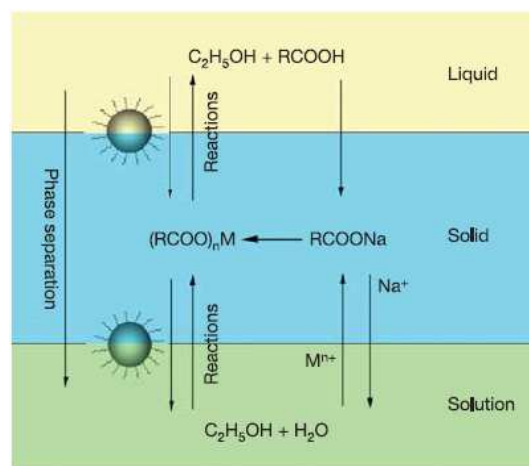


Fig. 17 The Liquid-Solid-Solution phase transfer Scheme (LSS) for the fabrication of Au NPs. Figure reproduced with permission from Reference 217.

C.I. Metallic nanoparticles

Many publications have been devoted to the synthesis and fabrication of gold colloids in the size range of 10 – 15 nm. In the early 1950s Turkevich presented a pioneer reduction-based method for producing gold of uniform size in the range of 20-150 nm.²¹⁰ This method was based on the development of an aqueous solution made by mixing an auric salt (gold chloride) and an organic reducing agent (sodium citrate). The process involves intense stirring and a slight heating around 100 °C. During the preparation process the reduction of an auric ion takes place, giving rise to a complex which easily decomposes when attaining a proper size, and finally forming a gold nucleus. They also demonstrated that the particle size was controlled by the kinetics of the reaction, so that the control of the nucleation parameters and growth stages could allow for the control of the nanoparticle size. About 20 years later, Frens et al. reported that by changing the relative amounts of reactants, i.e. by changing the sodium

citrate concentration during the nucleation process, they were able to control the size of their particles between 16 and 150 nm.²¹¹ Other modifications of this method include further filtration and detection processes to improve the monodispersity of the obtained colloids.²¹²⁻²¹⁴

An alternative method for the synthesis of Au NPs that has been extensively used is the so-called Brust method. This method is specially suitable for efficient synthesis of monodisperse Au nanoparticles in organic liquids that are immiscible in water.²¹⁵
 10 ²¹⁶ The method involves the reaction of a chloroauric acid solution with a tetraoctylammonium bromide (TOAB) solution in toluene and sodium borohydride as an anticoagulant and reducing agent, respectively.

Another method that has proven to be extremely versatile for fabricating any kind of nanoparticles (metallic, semiconducting or insulating) is the hydro(solvo)thermal one, developed by Wang et al.²¹⁷ This method performs chemical reactions in a solvent above its critical point under an elevated pressure and temperature, which is enabled by placing the reactants in aqueous or organic solvents in a sealed and heated autoclave. The main advantage of this method compared to the thermal decomposition methods is that lower reaction temperatures are needed and, at the same time, the implementation of a set of reactions is possible. The reaction mechanism is based on the so-called Liquid-Solid-Solution Scheme (LSS) (see **Figure 17**), which is mainly based on a phase transfer and separation process. In particular, for metallic nanoparticle separation, the primary reaction involves reduction of (noble) metal ions provided from a metallic salt, due to the action of ethanol at the interfaces of a certain metallinolate (solid), ethanol-linoleic acid (liquid phase) and water-ethanol (solution). Few hours are enough in order to obtain extremely monodisperse metal nanoparticles with sizes below 10 nm. These small nanoparticles can then be used as seeds for growing Au nanorods for photothermal therapy. For example, these nanoparticles can be used in a more complex seed-mediated growth method, as that used by Huang et al. This method is based on that from Murphy et al.²¹⁸ and Nikoobakht et al.,²¹⁹ and where the aspect ratio of the resulting rods and wires is determined by control of the ratio of metallic spherical seeds to metal salt during reduction

For the purpose of efficient photothermal therapies some other gold nanostructures, such as Au nanorods (GNRs) are of special interest as their optical and heating properties can be tailored from their rod geometry.^{83, 220} GNRs, known to be relatively stable and biocompatible,²²¹ were obtained by the modification of their surface with α -lipoyl- ω -hydroxyl poly(ethylene glycol) through ligand exchange from acetyl trimethylammonium bromide (CTAB)-stabilized gold nanorods.^{222, 223} Typically, GNRs were shown to have rod morphology with dimensions of about 40 nm \times 10 nm (aspect ratio around 4), although an adequate variation of the synthesis conditions could modify their aspect ratio. Indeed, it is nowadays possible to get commercially available GNRs with aspect ratios well in excess of 7.

Other gold nanoparticles with more complex geometries are also of relevance for photothermal therapies. This is the case of gold nanocages of relatively small size (about 50 nm edge length). They consist in nanostructures with cage shape and hollow or porous interiors which are made from sacrificial silver template

nanocubes that are sequentially transformed into gold nanocubes (or nanocages) by the so called galvanic replacement of Ag by Au atoms.²²⁴ Important factors affecting the optical properties are the morphology (edge wall thickness and cage sizes) and the composition, i.e. the relative amount of gold to the template silver. Both of them are controllable during the synthesis procedure.²²⁵ Additional biomedical perspectives for these nanostructures are their multiple functionalization and encapsulation challenge because of different outer or inner surfaces.^{113, 226, 227}

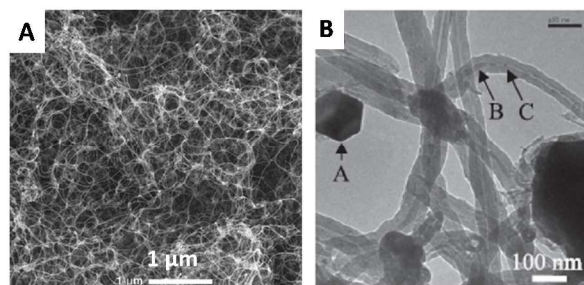


Fig. 18 (a) Typical SEM image of CNTs synthesized by the arc discharge method (b) Representative TEM image of CNTs synthesized by CVD. Arrows indicate the presence of remanent catalyst particles. Reproduced with permissions from References 228 and 229.

C.II. Carbon Nanotubes

As it has been described in greater detail in **Section B.II**, Carbon nanotubes (CNTs) consist in continuously rolled single sheets of carbon atoms, only a few nanometers across. There are several methods than can be used for the synthesis of CNTs. Among them, laser ablation, arc discharging and chemical vapor deposition (CVD) techniques in the presence of transition metal catalysts (such as Fe, Ni, Co) are the most popular ones.^{228, 230, 231}

These three different synthesis routes will be shortly described in the following paragraphs:

- *Arc discharge growth of CNTs*. In this case the synthesis of CNTs takes place inside a discharge reactor.²²⁸ The arc is generated between two electrodes in a reactor under a helium atmosphere (typical pressures around 660 mbar). A graphite rod (16 mm diameter, 40 mm long) acts as cathode, being the anode also a graphite rod in which a hole is drilled and filled with a mixture of a metallic catalyst and graphite powder. The arc discharge is then created between the electrodes. Typical synthesis times are around few minutes. Mixtures such as Ni-Co, Co-Y or Ni-Y are normally used as catalysts. Different carbon nanostructures can be synthesized, as described by Journet et al.²²⁸ **Figure 18(a)** shows a representative SEM image of CNTs growth by the arc discharge method.
- *CVD growth of CNTs*. CVD technique essentially involves the decomposition of a carbon-bearing gas and the diffusion and precipitation of C atoms on catalyst particles.²³² Iron compounds (e.g. oxides, nitrates) are often used as catalyst precursors. A pre-reduction step is generally made, using H₂ or NH₃ as reducing agents, prior to introducing a C containing gas such as CH₄ or CO.²³³⁻²³⁵ CNT growth from CH₄ commonly diluted by H₂ takes place at elevated temperatures. **Figure 18(b)** shows

electron microscope images of typical CNTs synthesized by CVD.²²⁹

- *Laser ablation synthesis of CNTs.* Laser ablation induced synthesis of CNTs is known to be an efficient and relatively simple technique since the pioneer work of T. Guo et al. in 1995.²³⁰ In this case, CNTs are produced by focusing a high power laser into a graphite target. When laser energy/power exceeds that required for optical breakdown of the target, carbon vaporization takes place. Recombination of vaporized carbon atoms leads to the formation of CNTs, which are collected in a cooled collector positioned downstream. In some cases, metal particles must be added to the graphite targets to act as catalysts, as it is also done in the arc discharge technique. Growing rates and structural properties of CNTs synthesized by laser ablation can be controlled by an adequate selection of laser power, target temperature, pressure and type of inner gas. Purity of CNTs synthesized by laser ablation has been reported to be above 90 %.²³⁶

C.III. Semiconductor nanoparticles

The synthesis of semiconductor quantum dots (QDs) has been carried out by different routes, generally top-down processing methods and bottom-up approaches.^{237, 238}

Top-down processing methods include molecular beam epitaxy (MBE), ion implantation, e-beam lithography, and X-ray lithography. In these approaches, a bulk semiconductor is thinned, and generally the obtained QDs have 30 nm of diameter approximately.

To synthesize colloidal QDs, self-assembly techniques (bottom-up) are used²³⁷. They can be broadly divided into wet-chemical and vapor-phase methods:

- *Wet-chemical methods* consist in following the conventional precipitation methods with a careful control of the parameters for a single solution. In a simplified view of the synthesis, two main events occur: the nucleation of colloids, followed by the growth of the nanocrystals. By heating a reaction medium to high temperature, the precursors chemically transform into monomers. Once the monomers reach a high enough supersaturation level, the nanocrystals growth starts with a nucleation process. The temperature during the growth process is one of the critical factors in determining optimal conditions for the nanocrystal growth. The wet-chemical methods include micro-emulsion, sol-gel, competitive reaction chemistry, hot-solution decomposition, sonic waves or microwaves, and electrochemistry.

- *Vapor-phase methods* start with atom-by-atom layer growth. After this, self-assembly occurs on a substrate without any patterning. Self-assembly of nanostructures in materials grown by MBE, sputtering, liquid metal ion sources, or aggregation of gaseous monomers are generally categorized under vapor-phase methods.²³⁸

C.IV. Ion doped nanocrystals

This kind of nanocrystals are usually based on fluoride (NaYF₄,

NaGdF₄, LaF₃, CaF₂ among others) and oxide materials as the most usual hosts, and lanthanide dopant ions as active emitters. Their applications have been mostly focused on imaging and nanothermometry. However, some works have recently been published reporting photothermal features by means of a wise tailoring of doping concentrations in order to favor the non-radiative transitions, and so the heat delivery from the NPs to the surrounding environment. A more detailed description about the physical characteristics of rare earth-doped nanocrystals is given in Section B.IV. Different methods have been used to prepare this kind of materials, including ionic liquids-based synthesis, co-precipitation, combustion, and sol-gel. However, the two methods that provide controlled size, uniform and monodisperse nanoparticles are the *hydrothermal* and the *thermal decomposition synthesis*.

The *thermal decomposition* synthesis is a two-step method. In a first step, organic precursors of the rare earth ions or alkali components are prepared and dried. In the second step, these precursors are decomposed in a high-boiling organic solvent that can act as a surfactant. The nanocrystals size, crystalline phase, and shape are controlled by the reaction parameters (reaction time, relative composition of the organic solvent and surfactants, addition rate of the precursors to the hot organic solvent). After this method was described by Yan et al. several kinds of fluoride nanoparticles, with different sizes and geometries, were obtained.²³⁹ These materials include LaF₃ triangular nanoplates, cubic and hexagonal NaGdF₄, NaYF₄, NaGdF₄, diamond shaped LiYF₄, NaYbF₄, Na₃ScF₆, YF₃, nanocrystals, etc.²⁴⁰⁻²⁴⁴ However, for each host-dopant combination, an optimization of the concentrations and synthesis parameters is needed.

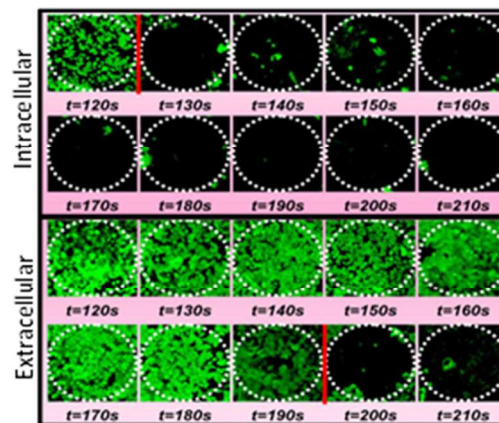


Fig. 19 Damage induced in liver cancer cells (obtained in terms of the FDA dye emitted intensity) produced by GNRs optically excited by an 800 nm laser beam for different irradiation times. Results obtained when the GNRs were located in either the surroundings or inside the cells (extracellular or intracellular heating, respectively) are shown. Data reproduced with permission from Reference 250.

The *hydro(solvo)thermal method* has been previously described in this review regarding the synthesis of gold nanoparticles. The versatility of this method has made possible to prepare several types of lanthanide-doped fluoride nanoparticles.^{245, 246} For this method, the size and morphology of the nanocrystals have been demonstrated to be strongly dependent not only on the reaction conditions and the surfactants but also on the doping ion

concentrations. This approach is very useful to obtain nanocrystals with different sizes and geometries. Examples that can be found in the literature include microprism crystals, microrods, microtubes, octahedrons, microspheres and flower-like NPs.^{201, 247-249} Despite its versatility, the hydro(solvo)thermal method presents several problems when considering the synthesis of insulating crystals: The preparation involves large reaction times (usually about 24 hours) to produce uniform and monodisperse nanoparticles and the particles obtained usually have sizes larger than 100 nm.

D. *In vitro* and *In vivo* treatments

Up to this point, the main features of the different nanoparticles of interest as photothermal agents have been described, so that it is now possible to choose the most adequate system depending on the desired spectral working range. Once the nanoparticles to be used have been selected, the next step is to look for the best conditions to perform a specific photothermal therapy. This second step has propelled an intensive research on both *in vitro* and *in vivo* experiments so that the future application of these nanoparticles in clinical treatments has been explored. In this section we summarize the most relevant pre-clinical experiments (both *in vivo* and *in vitro*) that have been used to identify experimental factors that should be controlled to ensure efficient photothermal therapy. This section has been divided into two parts. **D.I** is devoted to the description of *in vitro* photothermal therapies (at the cellular level) whereas **D.II** includes a general overview of the nanoparticle based photothermal therapies performed up to date in small animals (*in vivo* experiments).

D.I. *In vitro* photothermal treatments

Targeting and cell uptake assays are the first steps to design a photothermal therapy. Essentially, the selected L-HNPs are diluted in a biocompatible solution (usually saline buffer) and then they are left to interact with cultured cells during a certain incubation time in a suitable atmosphere and temperature environment. The incubation time is regulated in order to control the number of nanoparticles that interacts with cells (i.e. that are internalized or attached to the cell membrane). This is an important factor in order to increase the cell temperature within the typical values used for photo-induced thermal damage (see **Figure 1**). The determination of an optimum incubation time is far from being an easy task as it depends on a large number of factors such as those related to the particular L-HNPs used (size, shape, NP concentration in the bio-compatible solution, surface coating). Moreover, this incubation time also depends on a great variety of other factors, such as the particular tumoral cell line and the properties of the laser light source (wavelength, time modulation, energy fluence and polarization). Indeed, all these features will finally determine the degree and type of light-induced cell damage. Despite the complexity of the problem, as a large number of factors are involved, we will next discuss the most relevant ones so that strategical aspects can be established before carrying out a photothermal treatment. This section is, therefore, divided in the following subsections: *Effect of nanoparticle location*, *Size and shape effects*, *Concentration and incubation time effects* and *Relevance of laser beam properties*.

Effect of nanoparticle location

W. Zhou et al. were pioneers in pointing out the relevance of the location of heating nanoparticles, in respect to the cell, in the overall efficiency of *in vitro* photothermal treatments.²⁵⁰ In particular, they compared the efficiency of photothermal treatments at the cellular level when the L-HNPs are located outside the cell (in its surroundings) with that obtained when the photothermal agents are allocated inside the cell: Extracellular versus intracellular therapies. For such a comparative study, they used GNRs (30 nm long and 8.4 nm wide) as L-HNPs that were optically excited at around 800 nm. They observed that, for moderate CW laser powers, the photothermal therapy was more efficient when the GNRs were attached to the cells (intracellular therapy) than when the NHTs were outside the cells, i.e. in the bath solution around the cells to be treated (extracellular therapy). As a relevant example, **Figure 19** shows the damage induced in liver cancer cells (HeG2 line) by means of phosphorylcholine (PC) coated GNRs (a coat designed for specific targeting of these cells) as a function of CW irradiation time at 800 nm (200 mW laser power). The amount of damaged cells is quantified by using FDA dye fluorescent cell markers that can be observed by confocal fluorescence microscopy.²⁵¹ Thus, FDA fluorescence (green spots) gives a value of the number of living cells. It can be seen how for the intracellular modality (GNRs incubated 12 hours) virtually all the cells within the irradiated area are dead after 130 s of irradiation. On the contrary, the cells are still alive until almost 190 s of irradiation for the extracellular modality (GNRs not attached to cells). These authors also observed that GNRs internalized into cancer cells were mostly localized in the endosomes and lysosomes, from which hydrolytic enzymes should be released to the cytoplasm to cause fatal effects on the contained functional proteins.²⁵²

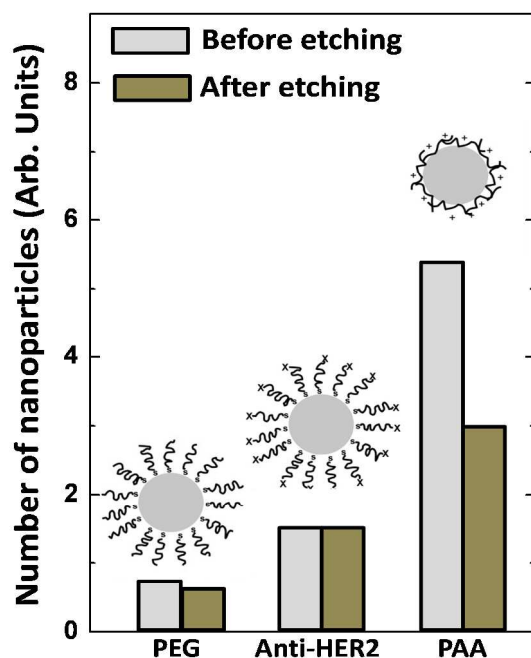


Fig. 20 Number of gold nanoparticles uptake by cancer cells (SK-BR-3) for three different surface coatings as obtained before and after etching. Data extracted from Reference 253.

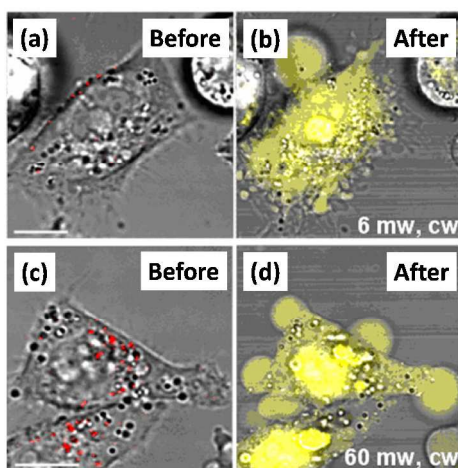


Fig. 21 (a) Optical image of a cancer cell incubated with GNRs (red points) allocated at the cell membrane before any optical treatment. (b) Fluorescence image of the same cell as in (a) after optical irradiation with a 6 mW laser beam, as obtained in terms of the EB emitted intensity (which reveals membrane damage). (c) Optical image of a cancer cell incubated with GNRs (red points) allocated inside the cell before irradiation. (d) Fluorescence image of the same cell as in (a) after optical irradiation with a 60 mW laser beam as obtained in terms of the EB emitted intensity. Reproduced with permission from Reference 254.

Data included in **Figure 19** demonstrate that efficient photothermal treatments require a large degree of interaction between the LHNPs and the cell to be treated by either intracellular incorporation or by selective attachment to the cell membrane. Such control can be obtained by an adequate surface modification. In this respect, E.C. Cho et al. investigated the efficiency of intracellular incorporation and membrane adhesion of Gold Nanoparticles with three different coatings.²⁵³ They studied SK-BR-3 breast cancer cells with three different coatings: PEG (a neutrally-charged polymer), PAA (polyallylaminehydrochloride, which provides a positive-charged coating) and anti-Her2 (an antibody for specific adhesion to SK-BR-3 cancer cells via body-antibody membrane targeting). These three different coatings are schematically displayed in **Figure 20**. After incubating cancer cells with the same amount of GNPs in exactly the same conditions, the uptake efficiencies for each surface coating were analyzed (see **Figure 20**) by means of coupled plasma spectroscopy (ICP-MS). The largest uptake efficiencies were obtained for PAA coated GNPs. Indeed, this superior uptake rate obeys to an efficient cell membrane adhesion, very likely due to the electrostatic attraction between the positive outer charges of the PAA-coated GNPs and the negatively charged membrane. This is followed by subsequent internalization of GNPs during the membrane evolution to its normal charge state. At variance, much lower uptake efficiencies were obtained for the other two (neutrally-charged) coatings. By suitable etching treatments, E.C. Cho et al. were able to conclude that, for the case of PEG and anti-Her coatings, most of the GNPs were located inside the cell whereas for PAA coating almost 50% of the GNPs remained at the cell membrane. So they provided evidence of how the uptake rate and location (intracellular or attached to membrane) of NPs can be controlled by surface treatment. Such a control becomes of great relevance when trying to increase the efficiency of photothermal treatments at single cell

level. Indeed, photothermal experiments systematically performed in tumoral (KB) cells have demonstrated a much more effective photothermal therapy when the L-HNPs (GNRs in this case) are located in the membrane than when they are internalized.^{254, 255} This is illustrated in **Figure 21**, which includes optical images of cancer cells with GNRs selectively attached to their membrane (red dots) before and after irradiation with a 6 mW laser power ((a) and (b), respectively). Cell damage was evidenced by the presence of the intracellular yellow luminescence of Ethidium Bromide (EB, a fluorescent cell damage probe).²⁵⁶ When the GNRs were incorporated into the cell instead of being attached to the membrane (see red spots in **Figure 21(c)**), similar cell damage levels required much higher laser powers (60 mW, **Figure 21(d)**), instead of 6 mW, **Figure 21(b)**). The authors stated that several factors could be contributing to a greater efficacy of photothermal therapies when L-HNPs are allocated at the cell membrane. In particular, they stated that the greater damage caused when GNRs were attached to the membrane could be due to a combination of three factors: (i) thermal disruption of the membrane, providing the most direct opportunity to inflict cell damage, (ii) focusing of photothermal effects (due to GNR accumulation) at the membrane and, finally, (iii) the relatively low thermal conductivity of cell membrane contributing to the creation of larger temperature gradients in the surroundings of the laser focus.²⁵⁷ In addition to all these possible reasons, some authors have also stated that, when L-HNPs are attached to the cell membrane, cell perforation is favored by light-induced cavitation processes.^{254, 258} It should be also noted that a slightly higher uptake efficiency was observed for the antibody coating than for the PEG one (see again **Figure 20**). This fact is essentially due to a larger adhesion to the cell membrane via body-antibody linkage and reveals the advantage of selective targeting of cancer cells via this type of interaction.^{82, 259-262} This kind of targeting allows for selective photothermal therapy, i.e. for damage creation only in preselected malignant cells by adequate body-antibody conjugation. In this respect, it is necessary to mention the results published by El-Sayed's group relating the use of anti-EGFR conjugated GNPs for photothermal treatment of three different cell lines; HaCat benign cells, and HSC and HOC malignant cells.^{83, 263} El-Sayed and coworkers studied for each cell line the damage induced as a function of the laser intensity. Results are summarized in **Figure 22**, where it can be observed how non-malignant HaCat cells were destroyed at much higher laser intensities (20 W/cm²) than HSC and HOC malignant cells (10 W/cm²). Thus, if the laser intensity is set between these two values, damage would only be restricted to malignant cells, leading to the achievement of a highly selective photothermal treatment. Such selectivity was explained by El-Sayed and coworkers in terms of the higher uptake rates for both types of malignant cells, as they over express EGFR on their surface membranes.^{82, 83} In fact, this increase in GNRs loading was corroborated by comparing the absorption spectra of malignant and non-malignant cells incubated with anti-EGFR conjugated GNPs; the surface plasmon resonance peak was clearly dominant for cancerous cells, indicating their larger uptake efficiencies.^{82, 83}

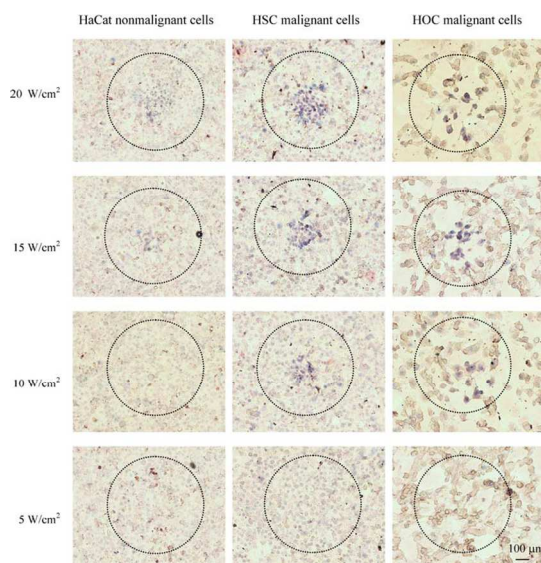


Fig. 22 Optical and fluorescence merged images of HaCat (non-malignant), HSC and HOC (malignant) cells incubated with anti-EFGR conjugated GNRs after laser irradiation at different laser intensities. Dashed circle indicates the spatial extension of laser spot. Cell damage is evidenced by the appearance of blue fluorescence emission generated by a damage cell marker. Figure reprinted (adapted) with permission from. X. Huang, I. H. El-Sayed, W. Qian and M. A. El-Sayed, *Journal of the American Chemical Society*, 2006, 128, 2115-2120. Copyright (2006) American Chemical Society

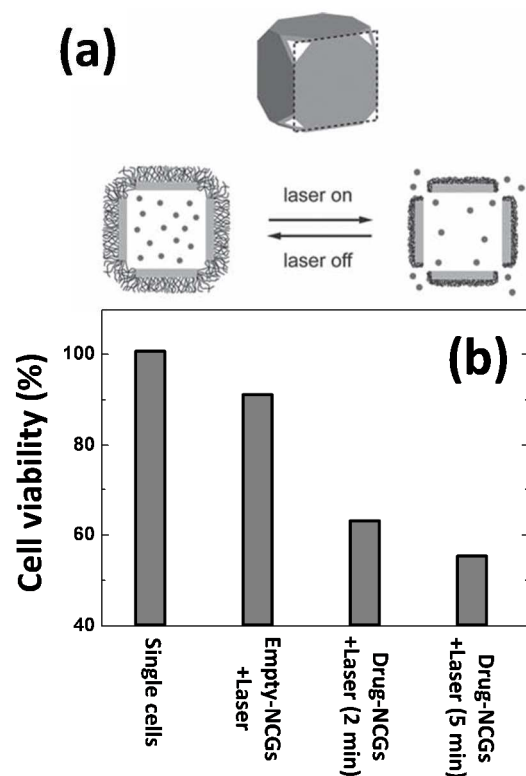


Fig. 23 (a) Schematic illustration of the photo-activated drug release system based on gold nanocages. (b) Cell viability corresponding to cells irradiated in the absence of Au nanocages, cells irradiated in the presence of empty Au nanocages, cells irradiated in the presence of drug-loaded Au nanocages for 2 min and cells irradiated in the presence of drug-loaded Au nanocages for 5 min. In all the cases the laser power density was set to 20 mW·cm⁻². Reproduced with permission from Reference 264.

20

Surface coating is not only useful to control NP adhesion and incorporation into cancer cells but it can also be used for other purposes, such as photothermally controlled drug delivery.²⁶⁴ M.S. Yavuz and coworkers demonstrated this possibility by using specially designed gold nanostructures.²⁶⁴ They managed to synthesize smart gold nanocages with pores in the corners. After being filled with an adequate drug, the nanocages were fully coated with a polymer in order to avoid drug leakage through corners (see **Figure 23(a)**). The polymer used by M.S. Yavuz et al. (poly-N-isopropylacrylamide) displays the property of varying its conformation when the temperature is slightly increased above a critical threshold value, in such a way that when the temperature is raised over this critical value the polymer chains tend to collapse.²⁶⁵ When this takes place, the pores are no longer blocked and the drug is released from the gold nanocages. Furthermore, when the temperature is decreased below the critical value, the polymer recovers its original form and the pores block once again. This temperature induced “*pore-gating*” can be activated by illuminating the gold nanocages at their plasmon wavelength resonance, so that the NP temperature is increased over the critical one. This possibility was, indeed, tested by Yavuz et al. who managed to place anti-cancer drug molecules in pored gold nanocages coated with a composed polymer that displayed a critical temperature of 39 °C.²⁶⁴ This is slightly above the body temperature (37 °C) but still below the temperature needed to perform hyperthermia (41 °C). Drug-loaded nanocages were incubated into breast cancer cells and the viability of these cells was studied after laser irradiation with laser intensity of 20 mW·cm⁻² at different treatment times. The results, summarized in **Figure 23(b)**, showed that the cell viability was reduced to about 60% for 2 min. of laser irradiation and still decreasing for 5 min. of irradiation. To point out the efficiency of the drug delivery process, the same experiment was carried out incubating cells with unloaded nanocages. This treatment led only to a reduction of 10 % in respect to the control (cells irradiated but non-incubated with nanocages). These results make it clear that the special design of nanoparticle and surface coating can also be used to achieve highly efficient photothermally-mediated drug delivery based therapies.

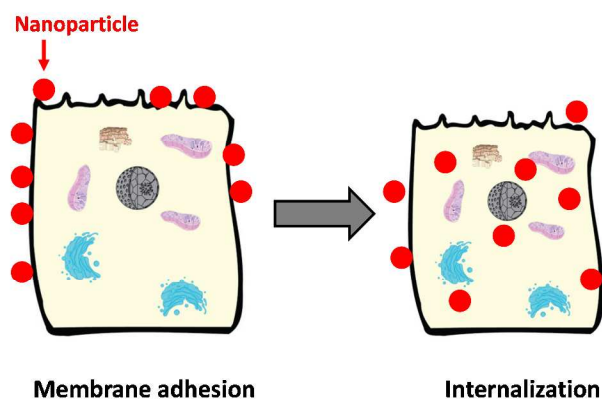
60 Size and shape effects

The size and shape of the L-HNPs could not only play a role in determining their optical properties and light-to-heat conversion mechanisms and efficiency (see **Section B**) but these factors are also crucial to determine the uptake efficiency by cells. This was, indeed, demonstrated by B.D. Chithrani and coworkers who demonstrated that, independently of the particular coating, spherical gold NPs are more efficiently up-taken by cancer cells than rod-shaped gold nanoparticles (GNRs).²⁶⁶ Moreover, they also evidenced that the internalization efficiency of GNRs decreases when the aspect ratio is increased. In principle, this result can be simply explained in terms of the longer membrane wrapping time required to fully endocytose elongated particles. By incubating gold nanospheres of different sizes (ranging from 10 to 100 nm) and analyzing the uptake efficiency by cancer cells, B.D. Chithrani et al. found that the optimum size is close to 50 nm in diameter.^{266, 267} Indeed, the existence of such an optimum size for cell uptake is in accordance with the results of F. Osaki et al., who also found a similar optimum size for

potential guests of endocytosis, such as viruses and lipid-carrying proteins.²⁶⁸ Thus a size of ~50nm is presently accepted as the optimum one for an efficient internalization into cells.

5 Concentration and incubation time effects

Nanoparticle concentration and incubation time are also known to be critical parameters determining the cell uptake efficiency of L-HNPs for *in vitro* experiments.²⁶⁹⁻²⁷² It is nowadays widely assumed that the uptake efficiency of NPs usually displays saturating trends with both parameters; i.e. the amount of nanoparticles internalized by the cells (usually in the order of few thousands, in the best cases) is limited. Typically, when dealing with immortalized cancer cells, incubation times larger than 4 hours do not lead to a further increment in the number of internalized NPs and, hence, *in vitro* experiments are usually limited to times no longer than about 4 h.²⁷³ As an example, a saturation plateau in the uptake efficiency of gold nanospheres has been reported by B.D. Chithrani et al. for incubation times larger than 4 hours and different NP diameters.²⁶⁶ The cellular uptake efficiency also displays a saturating behavior with the increasing concentration of NPs in the bath solution. However, in this case it is not possible to establish any concentration that could be considered as optimum.

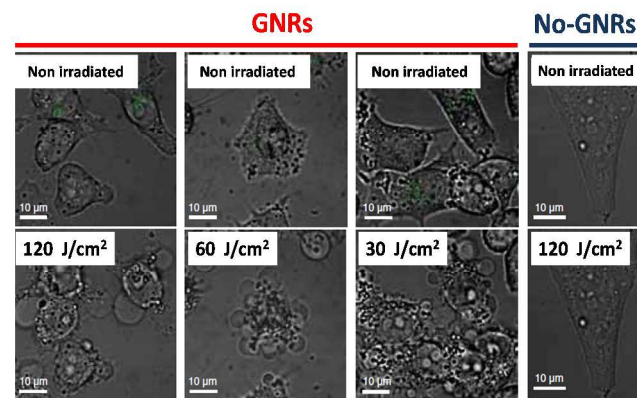


25 **Fig. 24** Schematic illustration of the NP uptake process by living cells.

At this point, it is important to recall that the NP uptake process by a given cell essentially involves two steps: (i) selective adhesion to the plasma membrane (cell adhesion), and (ii) subsequent internalization (see **Figure 24**).²⁶⁷ This second step is a receptor-mediated endocytosis and requires longer times (>10 h for relevant internalization).²⁷⁴⁻²⁷⁷ However, as it has already been discussed above, cell internalization is not strictly necessary for efficient photothermal *in vitro* therapies, so that such long incubation times are not required.

Finally, when determining the optimum concentration and incubation times the uptake efficiency should not be the only parameter to be considered. Other effects to be taken into consideration are toxicity and aggregation. A number of works have evidenced that some NPs are not toxic at low to moderate concentrations but they show some degree of toxicity when either incubation time or nanoparticle concentration is increased.²⁷⁸ In this respect, the associated cytotoxicity effects must be evaluated and considered when designing an *in vitro* photothermal treatment. In addition, when high NP concentrations are used, the

probability of particle aggregation in the culture medium (at the membrane or inside the cell) is increased. This is a key point, since for some of the L-HNPs described in Section B (such as CNTs, GNPs and QDs) their optical properties are strongly modified/deteriorated by the presence of aggregation. This effect could lead to a decrease in the efficiency of photothermal therapies even with an increasing number of NPs internalized by cells.²⁷⁹



55 **Fig. 25** Optical images of KB cells before and after laser irradiation at different laser fluences. Results obtained with and without incubation with GNRs are included. Data reproduced with permission from Reference 255.

Relevance of laser properties.

In general, photothermal therapies use lasers as light sources. Two types of time profile operating lasers are usually employed; pulsed or continuous wave lasers (hereafter PW and CW lasers, respectively). PW lasers are able to produce high peak intensities and, therefore, induce photothermal cell damage by different mechanisms than those activated by CW lasers. Regardless of the laser time profile, important parameters to be considered in a given photothermal treatment are laser intensity (often called power density) and energy fluence. The laser intensity (laser power divided by laser spot area) can be controlled by adjusting the laser power and/or the focal area. On the other hand, laser fluence gives a measure of the total energy delivered to the biosystem per unit area and can be adjusted through the irradiation time and/or the laser intensity. When the works dealing with *in vitro* photothermal experiments are reviewed, it is clear that the threshold laser intensity required to achieve cell destruction depends on a large variety of parameters, including the cell type, nanoparticles used as photothermal agents, number of nanoparticles uptaken by cells and environmental conditions. Due to this multi-parameter dependence the threshold intensities ensuring efficient photothermal treatment vary in a wide range. Nevertheless, typical intensities reported for photothermal treatment range from 1 to about 100 W/cm² when CW laser sources are used.

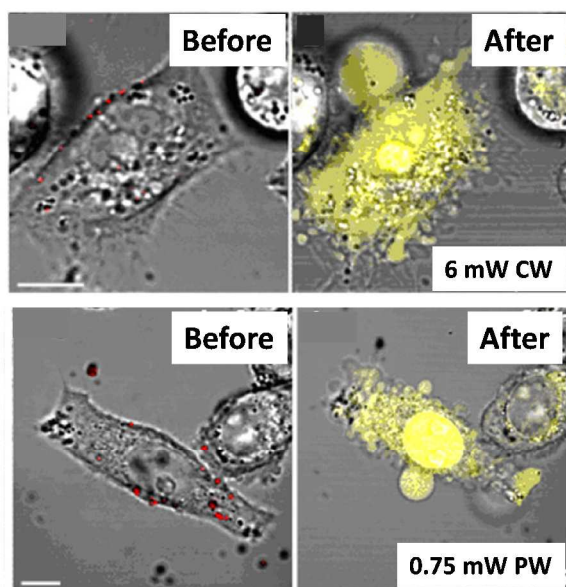


Fig. 26 Optical images of tumoral KB cells incubated with GNRs (denoted by red spots) before and after laser irradiation with a continuous wave or a pulse laser (CW or PW, respectively). Yellow fluorescence corresponds to EB and reveals the presence of cell damage. Reproduced with permission from References 254 and 280.

The threshold conditions required for efficient *in vitro* photothermal treatments can also be established/described in terms of laser fluence. This should always be kept below the so-called medical safety level.²⁸¹ T. B Huff et al. have performed systematic photothermal cell damage experiments at different laser fluences in GNRs incubated KB cells (a cell line derived from oral epithelium).²⁵⁵ **Figure 25** shows morphological changes that occur at cellular level for three different laser fluences (30, 60 and 120 J/cm²), when the irradiation was performed by a CW laser tuned to the surface plasmon resonance wavelength. Severe blebbing in cells containing GNRs is observed even for the lowest laser fluence (30 J/cm²), which is a clear indication of irreversible cell damage.^{282, 283} On the contrary, the morphology of the non-incubated cells is unaffected even for the highest laser fluence (120 J/cm²).

Thus, **Figure 25** evidences relevant morphological changes in living cells during photothermal treatment. The magnitude and type of these changes are also dependent on the laser operating mode (CW or PW). This is further evidenced in **Figure 26**, that includes optical images of tumoral KB cells incubated with GNRs (red spots at the cell membrane) under laser excitation with either CW or a PW laser.²⁵⁴ After photothermal treatment two main effects are observed. First, considerable membrane blebbing and second, a substantial increase in the membrane permeability induced by laser irradiation, this one manifested by the yellow fluorescence signal given by the EB fluorescence, which unequivocally reveals membrane damage. Photothermal treatment strongly degrades the integrity of the cell membrane and it does allow for influx of extracellular material. The laser-induced increment in cell permeability also explains the blebbing. As a matter of fact, it has been established that blebbing it is not a direct consequence of photothermolysis but a chemical damage that occurs as a result of influx of extracellular Ca²⁺ ions followed by degradation of the actin network.²⁵⁴ This is supported by

experimental evidence provided by L. Tong et al. who found that KB laser-irradiated cells with GNRs attached to their membrane did not experiment blebbing when they were in complete absence of Ca²⁺.²⁵⁴ L. Tong et al. also concluded that the efficiency of photothermal treatments was substantially enhanced when irradiation was done using PW laser sources instead of CW ones. In **Figure 26**, it can be observed that similar cell damage was obtained for PW and CW laser irradiation, but using a much lower laser fluence for PW-fs irradiation (24 J/cm² for CW irradiation and only 3 J/cm² for PW irradiation). Indeed, the mechanisms at the basis of cell damage under irradiation with PW lasers (femtosecond pulse widths) have been proposed to be completely different from those associated to CW photothermal therapies. Ultrafast PW lasers are able to produce high peak intensities in the femtosecond timescale, giving place to multiphoton absorption that initializes thermalization of conduction electrons. This excitation is produced in the femtosecond time whereas the electron-phonon assisted energy transfer from electrons to the surrounding medium takes place in the picosecond time scale.²⁸⁴ As a consequence of such big differences in the excitation/heat generation time scales, no remarkable heat diffusion to the environment of GNRs is produced and heating is restricted to tissue very close to the GNRs site. In the end, this causes a well-localized superheating that leads to plasma and cavitating bubble formation.²⁸⁵ Therefore, when femtosecond pulses are used, thermal damage is produced while keeping cellular temperature constant at its equilibrium value. On the contrary, CW lasers cannot produce such high intensities but keep plasmonic electron oscillations indefinitely, so that Joule heating occurs in a continuous way. Thus, heat is diffused through the whole cell increasing substantially its temperature.¹⁶⁰

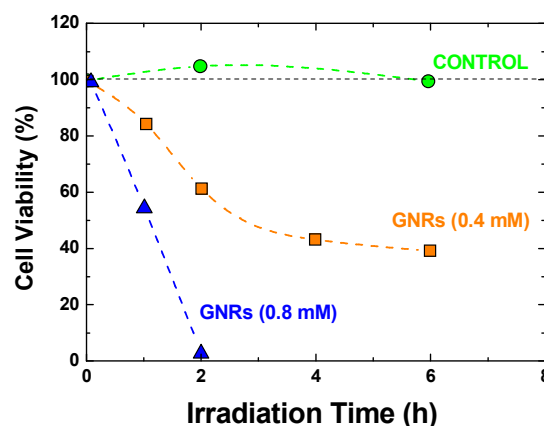


Fig. 27 Influence of GNRs concentration in the photothermal treatment efficiency performed in HeLa cells. Two GNRs concentrations were incubated. Control data are also included. Data extracted from Reference 18.

Photothermal therapy can also be strongly affected by the presence of the so-called reshaping effects. Reshaping occurs mainly in GNPs when the temperature reaches a critical value that produces melting and, thus, a remarkable change in shape. This effect takes place when moderate/large laser fluences are used and it has been widely reported and studied for the case of GNPs.^{107, 286-289} For the particular case of GNRs, laser-induced

heating transforms their rod shape into a spherical shape, deeply affecting the plasmonic extinction.²⁸⁸ H. Petrova et al have systematically investigated the temperature stability of GNRs deposited on a glass slide under both thermal annealing and femtosecond PW laser irradiation.²⁸⁸ They observed that at about 250 °C the nanorods are completely transformed into spheres after about 1 hour of thermal annealing, but partial reshaping occurs even at 100 °C. The same authors also studied this reshaping effect under fs-PW laser irradiation and indirectly estimated the local temperature at the GNRs sites. They demonstrated that the GNR shape was preserved for local temperatures below 700 °C. The different reshaping efficiency reached by thermal annealing and by fs PW laser irradiation was mostly associated to the fact that for ultrafast laser excitation the GNRs do not stay hot long enough to produce significant structural changes.²⁸⁸ The photothermal reshaping of GNRs has also been found to be a key parameter affecting the efficiency of the photothermal therapy, especially when large/moderate laser fluences are used. This was indeed evidenced by T. Hironobu et al., who studied the efficiency of photothermal therapies carried out in HeLa cancer cells incubated with GNRs and subjected to PW laser irradiation (5-7 ns Q-switched Nd:YAG laser).¹⁸

Figure 27 shows how the cell viability depends on the irradiation time (i.e. on the laser fluence) as obtained for different concentrations of GNRs. For HeLa cells without GNRs, no cellular damage occurs in the range of irradiation times studied. On the other hand, the cell viability decreases down to about 40% after 4 min of laser irradiation for cells incubated in a 0.4 mM GNR solution, and it does remain constant for longer times. This result was tentatively explained considering the fact that for such long times (laser fluencies) GNRs had been reshaped into spheres so that the longitudinal plasmonic absorption was quenched and damage was ceased as the energy absorption at the laser wavelength vanished. However, if the GNRs concentration is doubled (0.8 mM), this plateau is not observed, and after 2 min of laser irradiation 100% of HeLa cells have been photothermally damaged.¹⁸

An intelligent approach to improve the efficiency of photothermal treatments based on GNRs (and hence avoiding the use of long irradiation times that could lead to the appearance of reshaping effects) was proposed by H. Kang et al.²⁹⁰ They demonstrated how it is possible to perform efficient photothermal treatments in HeLa cells incubated with GNRs by using radially polarized beams instead of the traditionally used linearly polarized ones. The GNRs are randomly oriented inside the cell and so, when using linearly polarized laser radiation, only those GNRs orientated along the electric field vector would absorb laser light efficiently. Indeed, this means that only a small portion of the GNRs allocated inside the cell will contribute to the photothermal treatment. This fact can be solved by using a radially polarized laser beam so that the electric field associated to laser radiation inside the cell points along all the directions. This means that, although GNRs are randomly oriented, all of them would absorb the laser radiation (each GNR will absorb the electric field component along its longest dimension). H. Kang and coworkers demonstrated the benefits of radially polarized laser beam by incubating GNRs of 45 nm average length (aspect ratio 4) in human cervical cancer cells.²⁹⁰ They demonstrated (see **Figure**

28) that the minimum energy fluence required to induced severe cell damage when using radially polarized beams was five times lower that that required when linearly polarized beams were used. H. Kang et al also found that radially polarized beams lead to much more intense fluorescence cellular images due to a larger amount of excited GNRs.²⁹⁰

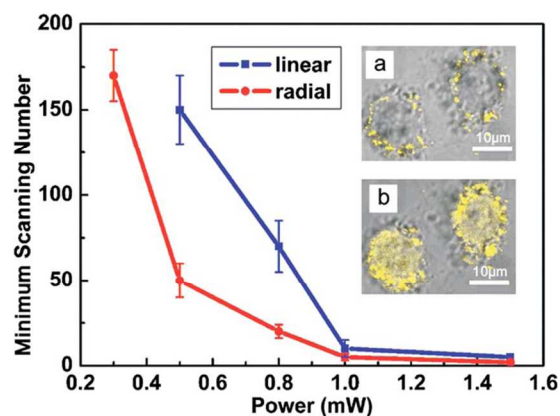


Fig. 28 Number of required scanning cycles (a measure of the energy fluence) required to cause irreversible damage in HeLa cancer cells incubated with GNRs as obtained when radial and linear polarized laser beams were used. Insets show two photon fluorescence images of the HeLa cancer cells incubated with GNRs as obtained when linear and radial polarized beams were used. Published with permission from Reference 290.

Another relevant approach involving pulsed lasers for photothermal *in vivo* therapies is the so-called laser-activated nano-thermolysis (LANTCET) method, developed in the recent years by Lapotko et al.²⁹¹ This method allows the selective detection and destruction of individual tumor cells by the generation of intracellular photothermal bubbles, around clusters of gold nanoparticles. The physical insight of this technique comes from the non-stationary character of the sequential heating processes. Due to its non-stationary on-demand nature, the bubbles created after laser irradiation of clusters of gold nanoparticles are formally not a particle but an event. Plasmon resonance of GNPs converts optical energy into highly localized heat that evaporates liquid near the surface of GNPs. This creates expanding and collapsing vapor nanobubbles, termed plasmonic nanobubbles (PNB). The lifetime of these PNBs varies between 20 and 300 ns.²⁹² When PNBs are created inside cancer cells, they can induce cell death due to a pure mechanical process rather than a pure thermal one. Indeed, the collapse of the so-generated PNBs causes the explosive disruption of the cellular membrane and other components and can be defined as immediate lysis, not apoptosis or necrosis. The PNB treatment using a 40 mJ/cm² single laser pulse demonstrated a 97% mortality rate on cancer cells while causing a minimum effect on normal cells (cell death level below 21%), even those adjacent to the cancer cells where PNBs were generated.²⁹³ The laser fluences required were then 4-6 orders of magnitude lower than those employed in previously reported *in vivo* studies of photothermal hyperthermia with gold NPs ($3-72 \times 10^2$ J/cm²).²⁹⁴ Besides, the remarkable target-cell specificity of PNB-based photothermal processes is of special interest due to the fact that thermo-mechanical damaging processes are fully confined in the endosomal system of the target (cancer) cells.^{295, 296} The PNBs have also been used in other

therapeutic methods in nanomedicine, such as intracellular and extracellular drug release^{297, 298}.

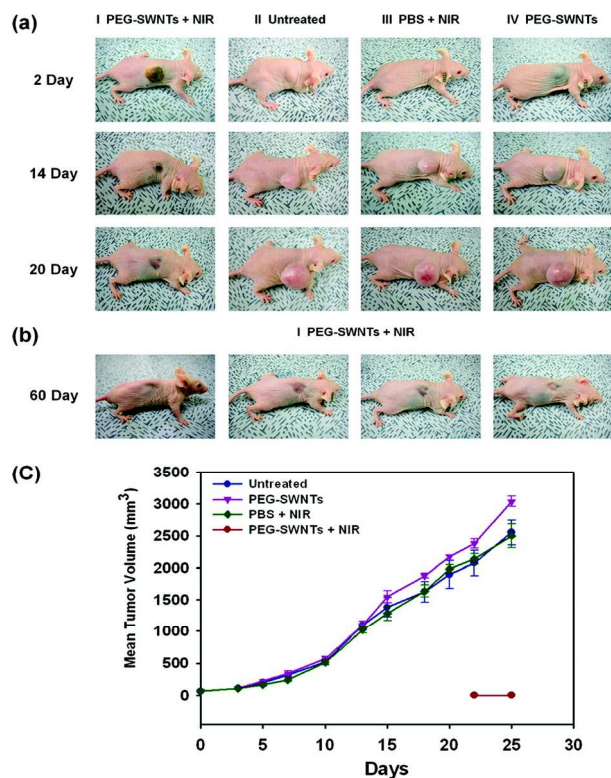


Fig. 29 (a) Representative photographs of mice inoculated with malignant cancer cells (KB cells) photothermally treated and untreated at different times after each treatment (I, PEG-CNTs + NIR; II, untreated; III, PBS + NIR; IV, PEG-CNTs). (b) Four mice 60 days after different treatments. (c) Time-dependent tumor growth curves of tumors after photothermal treatment. Figure reprinted (adapted) with permission from H. K. Moon, S. H. Lee and H. C. Choi, *ACS Nano*, 2009, 3, 3707-3713. Copyright (2009) American Chemical Society.

D.II. *In vivo* photothermal treatments

The performance of efficient *in vivo* photothermal treatments requires the incorporation of sufficient amount of L-HNPs into tumors to be treated. Then, the tumor must be illuminated with an adequate laser source in such a way that tumor temperature is significantly increased while minimizing the heating effects caused to healthy tissues. The selective incorporation of L-HNPs into tumors can be achieved by following two different strategies: active and passive targeting. For active targeting, the surface of L-HNPs must be coated (functionalized) with adequate antibodies which can be specifically recognized by proteins over-expressed in the malignant cells. On the other hand, passive targeting is based on the so-called enhanced permeability and retention (EPR) effect of tumors and cancer cells.^{299, 300} This effect exploits abnormalities of tumor vasculature, aberrant vascular architecture and extensive production of vascular permeability factors to stimulate extravasation within tumor tissues. In addition, as the goal is to administrate L-HNPs intravenously, their size and coat may also be designed so as to avoid a rapid renal clearance, thus displaying long blood half-lives, i.e. long circulating times in the bloodstream.^{301, 302} In some *in vivo* experiments, L-HNPs are incorporated into the tumor by direct injection, i.e. the solution

containing the L-HNPs is not injected into the bloodstream but directly injected into the tumor. This method ensures a large intratumoral concentration of L-HNPs although it does not give a clear idea of the treatment efficacy in real conditions. For a more realistic approach, L-HNPs are intravenously administrated.

The procedure usually followed for simple *in vivo* photothermal treatment of tumors has different steps: first, the tumors are induced in healthy mice. Usually, two tumors are induced in each mouse, in such a way that one of them is treated and the remaining one is used as a control tumor. Then, L-HNPs are incorporated into the tumor by means of any of the methods described above. Once the L-HNPs are inside the tumor (inside the cancer cells or at their membranes) the tumor is illuminated by an external laser source so that intratumoral thermal loading is produced. The effectiveness of the treatment is usually evaluated by measuring the time evolution of the size of both treated and control tumors. The wavelength of the heating laser source is a critical parameter in this kind of experiments. Obviously, laser radiation has to be absorbed by the L-HNPs but, at the same time, it should be minimally absorbed by the tissues. This second condition should be satisfied in order to achieve selective heating, i.e. to heat only those tissues in which L-HNPs have been incorporated. Blood and tissues usually present strong absorption bands in the visible. Thus, *in vivo* photothermal treatments usually employ near infrared lasers (NIR lasers, with wavelengths larger than about 700 nm).^{106, 304} Laser irradiation of the tumor is carried out for a certain time (usually in the order of few minutes, until the tumor temperature reaches a steady value). Both the laser intensity and the irradiation time determine the magnitude of temperature increase caused in the tumor and so, according to **Figure 1**, the net effect caused on the tumor cells. As a consequence, the final result of the treatment would also be strongly dependent on both the laser irradiation intensity and treatment duration. This fact has been evidenced by several studies. Among them, the one performed by N. Huang et al. is especially relevant, as they studied how the efficiency of photothermal treatments of carcinoma tumors in mice (using CNTs) can be improved by an adequate selection of both laser intensity and irradiation time.³⁰⁵

The efficacy of a given photothermal treatment is usually elucidated by evaluating the time evolution of the treated tumor volume and comparing with that of the non-treated (control) tumor. This is illustrated in **Figure 29**, which shows how photothermal therapy is successfully applied to destroy malignant tumors (KB cell line) inoculated in mice backs by using SWCNTs as L-HNPs.³⁰³ After the induced tumors reached a volume of about 70 mm³ (2 days from the inoculation), a group of mice was intratumorally injected with 100 μ L of a PBS solution containing the nanoheaters (120 mg of PEG coated-SWNTs) and then subjected to CW laser irradiation at 808 nm (76 W/cm²) during 3 min.³⁰³ It can be observed as, for a mouse irradiated in such a way, the tumor was completely destroyed after 20 days (**Figure 29(a)**) and how after 60 days the mouse is still alive (**Figure 29(b)**). In fact, N. Huang et al. reported that over six months those photothermally treated mice displayed a healthy behavior without toxic effects or tumor recurrence. On the contrary, for the control mice (i.e. for non-irradiated mice or those irradiated but not injected with CNTs) tumors substantially

keep growing with the time after inoculation, reaching sizes near to 3000 mm³ after 25 days of tumor inoculation (Figure 29(c)). All control mice were dead after 60 days from inoculation (Figure 29(b)).

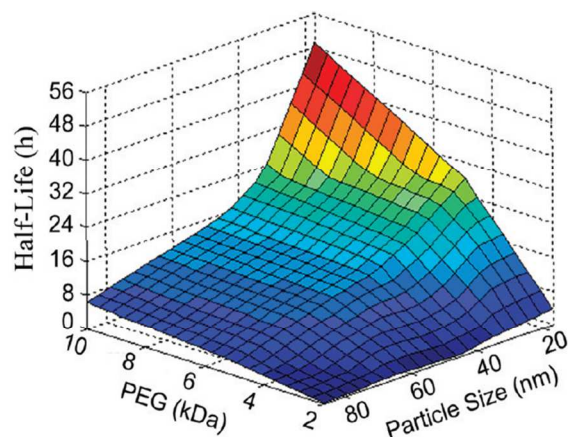


Fig. 30 Dependence of the blood half-life of PEG coated gold nanospheres on both particle size and molecular weight of PEG coating. Published with permission from Reference 306.

Finally, it should be mentioned that successful photothermal cancer therapy has been also achieved at laser fluences below the medical safety level using organic nanoparticles. Particularly, in vivo tumor destruction has been achieved in the case of polypyrrole NPs under a total laser fluence of 75 J/cm².

Biodistribution of L-HNPs

It is important to recall here that in the experiments of Figure 29, the L-HNPs (carbon nanotubes in that case) were directly delivered to the tumor by means of intratumoral injection. As commented before, while this method can be very successful for subcutaneous tumors, it does lack from clinical applicability. In a more realistic approach, the L-HNPs should be intravenously administrated, so that its selective accumulation in the tumoral regions would be produced after travelling through the blood stream. This has propelled numerous *in vivo* and *ex vivo* biodistribution studies of different L-HNPs in animals, mostly in mice, in order to establish proper models for their blood circulation ability, their retention into different organs and the excretion time and mechanisms.³⁰⁷⁻³¹¹ A complete review of all these aspects has been recently published by N. Khlebtsov et al.²⁷⁸ From this work it is evident how the biodistribution of NPs among the different organs depends on a variety of parameters such as their size and shape, surface coating, amount of incubated material, incubation time and injection mechanism. All these factors finally regulate the clearance of the L-HNPs from the blood, their ability to reach a tumor site, as well as the L-HNPs removal after a given photothermal treatment has been carried out. Although the majority of these models are related to gold-based nanoparticles, the main aspects can be considered independent on the nanoparticle type and so these models are nowadays considered as “standards” to evaluate the biological response to other L-HNPs.

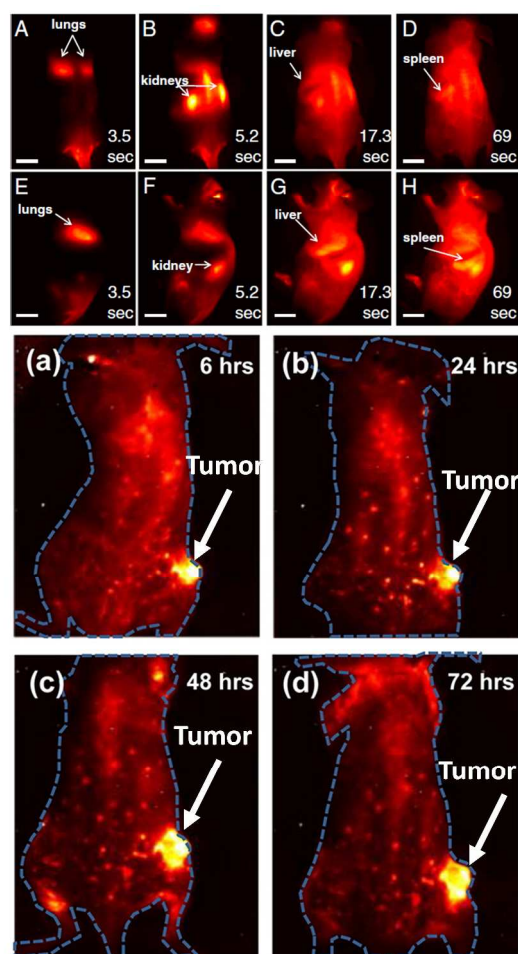


Fig. 31 Fluorescence images of a mouse after intravenous injection of luminescent SWCNTs. Figure (A)-(H) correspond to short times after injection (<1min) in a mouse free of tumors. Figure (a)-(d) correspond to the fluorescence images of a tumor at long times (6-72 h) after injection (indicated by an arrow). Figure (A)-(H) reproduced with permission from Reference 305. Figure (a)-(d) reprinted (adapted) with permission from J. T. Robinson, G. Hong, Y. Liang, B. Zhang, O. K. Yaghi and H. Dai, *Journal of the American Chemical Society*, 2012, 134, 10664-10669. Copyright (2012) American Chemical Society.

It is broadly assumed that, after intravenous injection of L-HNPs an efficient incorporation into tumors requires long circulating times, i.e. large blood half-life. A great effort is being done to achieve such long circulating times, which is not an easy task as many factors could be of significance. Perrault et al. used PEG-coated spherical gold nanoparticles as a model to investigate how relevant was the particle size in determining the blood half-life.³¹² PEG coating is usually selected for non-active delivery/targeting as it shows a close to zero potential. This, in principle, leads to a non-interacting surface and allows for long blood half-lives: indeed, this coating is used in several pharmaceutical drugs.³⁰⁶ Figure 30 shows the dependence of the blood half-life of PEG-coated colloidal gold nanospheres on both particle size and molecular weight of PEG coating. It can be seen that the blood half-life increases for decreasing particle size while, for a given particle size, it increases with the amount of PEG coating (PEG molecular weight). In particular, the largest half-life times (about 50 hours) were obtained for gold nanoparticles of about 20 nm (core diameter) but with high molecular weight of PEG coating

(10 KDa). This coat increased the hydrodynamic particle size up to about 60 nm (core+shell diameter). At this point, it is also important to recall that the size of the L-HNPs vehicles must also be optimized in order to maximize the tumor up-taking rate. As it has been mentioned previously,²⁶⁶ the uptake efficiency is optimum for sizes close to 50 nm. Therefore, this size (around 50 nm) simultaneously optimizes the blood circulating time and the uptake rate and, therefore, emerges as the optimum one for efficient photothermal treatments.

The total amount of particles accumulated in a tumor also depends on the surface coating. For instance, the surface (coating) charge of L-HNP has been found to play a relevant role.³¹³ Positively-charged nanoparticles were efficiently endocytosed by tumor cells, while negatively charged nanoparticles spread throughout the whole tumor.³¹³ In any case, previous biodistribution studies are needed for the selected L-HNP type before applying a given photothermal therapy.

Luminescence tracking of L-HNPs

Another important factor to be considered is that suitable imaging techniques must be used in order to monitor in real time the location of L-HNPs during *in vivo* treatments. Ideally, each particular L-HNP type should provide a mechanism to be optically imaged during its circulation in the blood. Otherwise L-HNPs must be synthesized with additional fluorescent labels that should also be stable during both the L-HNPs blood circulation and photothermal treatment. There is also the possibility of using additional analytical techniques (such as instrumental neutron activated analysis³¹⁶, inductively coupled plasma-mass spectrometry³¹⁷ or high performance liquid chromatography and immunohistology) to quantify the L-HNPs content in the different organs and tissues. Of course, the simplest approach is to use luminescent L-HNPs to achieve real-time tracking, since type of NP is required and the same excitation source used for the photothermal treatment could be used to excite the L-HNPs luminescence.

In the literature, there are several examples of real-time tracking by means of L-HNPs. As an example, the broad emission spectrum of SWCNTs in the second biological window has allowed for deep tissue anatomical fluorescence imaging of living mice.³¹⁴ S.P. Welsher et al. were able to record the real-time circulation of SWCNTs through lungs and kidneys several seconds after tail injection and how these nanoparticles were mostly located at the spleen and liver at longer times (see **Figures 31(A-H)**).³¹⁴ This pioneer work propelled the study of other novel nanofluorophores for deep tissue fluorescence imaging in the second biological window^{103, 180}. SWCNTs have not only been used for real-time biodistribution experiments but also to track their incorporation into tumors. **Figures 31(a-d)** show deep tissue fluorescence images of a tumor-bearing mouse after intravenous injection of CNTs, as reported by J.T. Robinson et al.³¹⁵ The long circulation times achieved (half-lives longer than 30 hours) allowed for an outstanding uptake efficiency by the tumor (indicated by arrows in **Figures 31(a-d)**). Indeed, J.T. Robinson et al. claimed that almost 30% of the injected CNTs were finally accumulated into the tumor. Such a large uptake was evidenced by the strong luminescence generated at tumor's location (see **Figures 31(a-d)**).

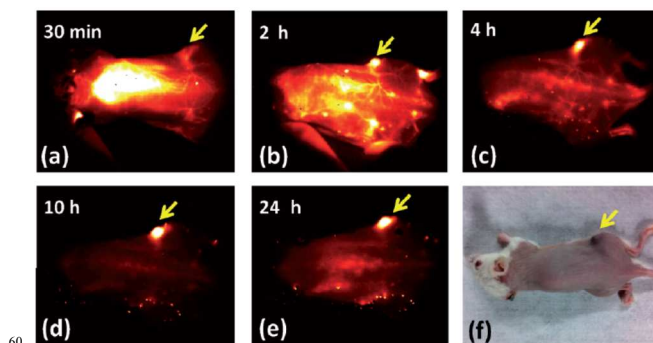


Fig. 32 Fluorescence images of a mouse after intravenous injection of a solution containing Ag_2S -QDs as obtained at different times after injection. Arrows indicate the location of a subcutaneous xenograft 4T1 murine tumor. Data reproduced from Reference 318 with permission.

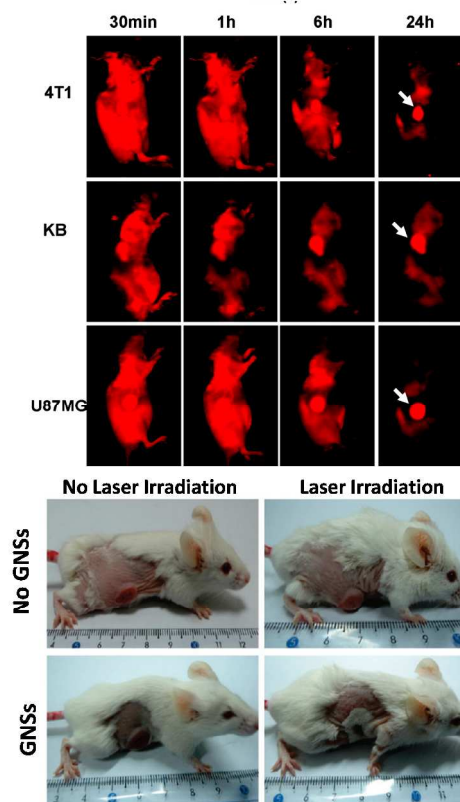


Fig. 33 Top- Fluorescence images of three mice with different tumors (indicated by arrows) as obtained at different times after intravenous injection of graphene Nano Sheets (NGSs). **Bottom-** Pictures of two mice with tumors obtained before and after laser irradiation in absence (no NGSs) and presence (NGSs) of intravenously injected NGSs. reprinted (adapted) with permission from K. Yang, S. Zhang, G. Zhang, X. Sun, S. T. Lee and Z. Liu, *Nano Letters*, 2010, 10, 3318-3323. Copyright (2010) American Chemical Society.

Deep tissue luminescence tracking as well as outstanding tumor uptake has also been demonstrated by using PEG-coated- Ag_2S biocompatible quantum dots emitting in the second biological window (at around 1200 nm). These nanoparticles display a reasonable fluorescence quantum yield (15 %) and so they allow for monitoring, in real time, their incorporation into a tumor.³¹⁸ **Figure 32** shows fluorescence images of a tumor bearing mouse after intravenous injection of PEG coated Ag_2S -QDs.

These nanoparticles had an average hydrodynamic diameter of about 54 nm, close to the optimum one. As can be observed, Ag_2S -QDs are passively accumulated at the tumor site as a result of the EPR effect, leading to a strong fluorescence signal at the tumor site. It should be noted that, due to its low quantum yield, these QDs could also act as efficient nanoheaters (i.e. as L-NHTs). As can be observed from the fluorescent images, the maximum QD concentration inside the tumor seems to be reached 10 hours after injection. Therefore, this would be a suitable time to start a photothermal therapy.

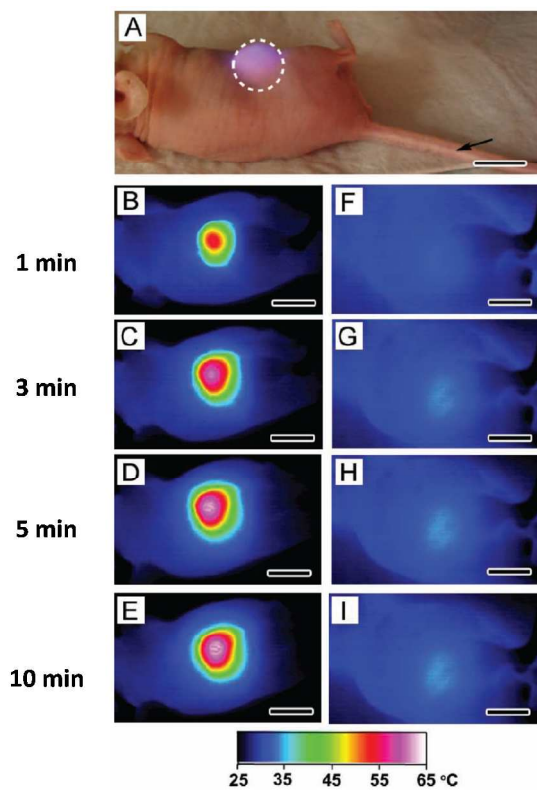


Fig. 34 (A) Photograph of a tumor-bearing mouse undergoing a photothermal treatment after intravenous injection with a colloidal solution containing PEG-coated gold nanocages. Thermographic images of (B–E) nanocage-injected and (F–I) saline-injected tumor-bearing mice at different irradiation times. Data reproduced with permission from Reference 321.

At this point, it is important to note that the time required to optimize the NP concentration inside tumors after intravenous injection will depend on the NP (material, size, shape and coating). This fact has been evidenced by a work recently published by K. Yang et al., who studied the incorporation of PEG-coated nanographene sheets (NGSs) into tumor-bearing mice after intravenous injection.³¹⁹ These authors observed (see **Figure 33**) that the highest intratumoral concentration of NGSs was achieved 24 hours after the intravenous injection. This was experimentally evidenced for three different tumor types.³¹⁹ In this case, since NGSs luminescence was hard to be detected, K. Wang et al. labelled NGSs with a NIR emitting dye, so that fluorescence tracking of NGSs was possible. Note in **Figure 33** how, 24 hours after injection, the fluorescence tumor signal clearly dominates over other the signals coming from other organs and tissues.³¹⁹ Again, the authors explained this dominant

tumor accumulation of NPs as a result of an efficient EPR effect. Indeed K. Wang et al claimed that the use of a sheet-like geometry (2D geometry) should favor the tumor uptake efficiency.³¹⁹ In fact, taking advantage of their heating property, these authors demonstrated efficient photothermal therapy of tumors by irradiating them with a 808 nm laser beam at moderate laser intensities (close to $2\text{W}/\text{cm}^2$). As can be observed in **Figure 33**, the laser-induced tumor heating (with an estimate temperature close to $50\text{ }^\circ\text{C}$) was high enough to eliminate the tumor. Tumors not containing NGSs irradiated under the same conditions did not experiment any beneficial effect (see **Figure 33**).

Heating Nanoparticles for co-adjuvant therapies

As we have already mentioned in **Section A**, photothermal therapies based on L-HNPs can be also used in combination with other cancer therapies (chemotherapy and radiotherapy).^{242, 322} In this sense, the results provided by R.L. Atkinson et al. should be mentioned.³²³ They demonstrated that the incorporation of GNSs into solid tumors could improve the efficacy of radiation based therapies. Authors incorporated GNSs into solid breast tumors that were exposed to both near infrared laser light and a dose of 6 Gray of ionizing radiation. As a consequence of this dual treatment, authors observed tumor contraction as well as a reduction in the number of stem cells that are especially resistant to radiation therapy. In addition, the same authors found that this dual treatment makes the tumor less aggressive.

The importance of temperature control during therapy

Finally we would like to point out the importance of real-time control over tumor temperature during photothermal treatments. Here, it is important to mention that for mice photothermal treatments typical temperatures to destroy tumors use to be below $60\text{ }^\circ\text{C}$ and higher than $48\text{ }^\circ\text{C}$, i.e. in the irreversible injury temperature range (see **Figure 1**). The final tumor temperature depends on a number of factors, such as laser features (intensity, pulsed or continuous mode, spatial laser mode, polarization mode...etc), number of nanoparticles inside the tumor, irradiation time...etc. Thus the temperature control in real time of the irradiated area and surroundings is essential not only in simple photothermal treatments but also in those combined that have been described in the previous paragraph. J.Y. Chen et al performed photothermal cancer therapy in several tumor-bearing mice to account for the importance of temperature control during photothermal treatments.³²¹ Mice were intravenously injected with a solution containing PEG-coated gold nanocages (GNCs) and the photothermal response was compared to that from mice injected only with a saline solution (i.e. without GNCs). **Figure 34** shows a photograph of a mouse whose tumor containing GNCs was being laser irradiated (with an intensity of $0.7\text{ W}/\text{cm}^2$). The laser wavelength was that of the surface plasmon resonance (808 nm) so that laser radiation was efficiently absorbed by GNCs. **Figures 34(B–E)** include the surface temperature images of the irradiated tumoral area, as obtained at different irradiation times. It can be clearly seen that the tumor temperature increases with irradiation time, reaching a maximum surface temperature close to $60\text{ }^\circ\text{C}$ for 10 min of irradiation. It can also be noticed how the temperature rise profile spreads out with time, due to heat diffusion. On the other hand, the thermal images of the non-injected tumor-bearing mice

display only a slight temperature increase during irradiation (see **Figures 34(F-I)**). As we stated in **Section A-1** (see also **Figure 1**), temperatures close to 60 °C would lead to irreversible damage in cancer cells but, in addition, a severe tissue damage could be caused. In other words, an excessive heating could create non selective damage. In fact, J.Y. Chen et al. also demonstrated that even in the case of a complete localization of L-HNPs inside tumors, the heat generated under laser irradiation could spread out of the tumor and so affecting healthy tissues³²¹. Thus, the minimization of collateral damages during photothermal treatments requires the development of novel techniques capable of thermal imaging and sensing, so that both laser intensity and treatment duration can be dynamically adjusted to keep temperature below the damage limit (60 °C). As well as in Chen's work, many authors used infrared thermal cameras to achieve such thermal control. Nevertheless these cameras provide the surface (skin) temperature, which could substantially differ from the intratumoral temperature.

E. Conclusions and future perspectives

In summary, we have presented a detailed review of the diverse nanoparticles that are currently being used as photothermal agents. The goal of these nanoheaters is to achieve highly efficient and selective thermal therapies for different diseases, although mainly for cancer. It has been shown that many nanoparticles (metallic nanoparticles, quantum dots, carbon nanotubes, graphene-based nanoparticles, rare earth-doped nanoparticles and organic nanoparticles) can be used as photothermal agents, i.e. show large light-to-heat conversion efficiencies. We have provided, for each kind of nanoparticle, fundamental information on the physical processes responsible the light-to-heat conversion. Special attention has been paid to those nanoparticles working in the biological windows (700-1400 nm), giving their specific spectral working ranges and fluorescence properties, that can provide the additional advantage of targeting and tracking by means fluorescence imaging. A general overview of the different routes for the synthesis of each system has also been provided. Finally, this work also includes a detailed description of the state of the art concerning the use of these photothermal agents for *in vitro* and *in vivo* therapies. We have paid special attention to highlight the critical points that could limit the efficacy of a thermal treatment, so that the reader could extract basic ideas for the design and establishment of adequate experimental protocols towards non-invasive, efficient photothermal treatments. When looking for the optimum nanoparticles for photothermal therapies we have concluded that, at the present time it is not possible to highlight one single system above the others, since a great variety of parameters are involved. For instance, the right nanoparticle to be used will depend on the spectral properties of the light source available for heating as well as the location and type of the target tissue. Nevertheless, according to the results reported up to now it is clear that both gold nanoparticles and carbon nanotubes are the most developed, controlled, and understood nanoparticles. Both have demonstrated large heating efficiency and outstanding biocompatibility. However, they have the main drawback of showing a weak fluorescence, which makes hard to track them in real *in vivo* treatments. In this respect, other

systems emerge as promising nanoheaters, such as quantum dots, rare earth doped nanoparticles and organic nanostructures. On the other hand there is a need for searching the best wavelengths within the biological windows, in order to get the deepest tissue penetration for real photothermal therapy. Thus, there still is a large field of improvement and work to be done before these nanoheaters can be clinically used as photothermal agents. For sure, this will be one of the main working areas in the field of nanotechnology during next years.

From this review, it is also concluded that efficient photothermal therapies require real-time control over the temperature increment induced. This implies the incorporation of luminescent nanothermometers in the volume to be treated simultaneously with the photothermal agents. This possibility, which would allow for real-time monitoring of temperature and dynamical control over treatment parameters, has already been demonstrated by using, simultaneously, two kinds of nanoparticles. The next step would obviously be the development of heating nanoparticles capable, at the same time, of heating and temperature reading. We predict that, in the near future, multifunctional nanoparticles will be developed offering heating and sensing in a single structure. The use of such fluorescent heating and thermometric nanoparticles will not only allow for the development of imaging-guided photothermal therapies (already possible by the combination of many different techniques such as CT, MRI, PET and PA) but also to achieve real time tumor thermal sensing. This last being a very challenging objective.

Additionally, the research on new therapies will very likely be focused not only in the development of novel heating nanoparticles but also in the development of novel light-to-tissues transfer mechanisms.

Finally, we believe that further development of photothermal therapies does not only call for the synthesis of novel nanoparticles with extended functionalities, but also requires the creation of new experimental apparatus. These novel setups would allow for complex experiments in which heating, nanoparticle tracking, thermal sensing and health-related parameter recording could be simultaneously achieved.

Work supported by Spanish Ministerio de Economía y Competitividad under project MAT2010-16161. A. Benayas gratefully acknowledges Le Fonds de recherche du Québec - Nature et technologies (FRQNT), for the Postdoctoral Fellowship granted to him through "Programme de Bourses d' Excellence". EMR is funded by the Marie Curie program (PIOF-GA-2010-274404 – LUNAMED).

Notes and references

^a Fluorescence Imaging Group, Departamento de Física de Materiales e Instituto Nicolás Cabrera, Facultad de Ciencias, Universidad Autónoma de Madrid, Campus de Cantoblanco, Madrid 28049, Spain Fax: 34+914978579; Tel: 34+914976424; E-mail: daniel.jaque@uam.es
^b Univ Quebec, Inst Natl Rech Sci Energie Mat & Telecommun, Varennes, PQ J3X 1S2, Canada

1. B. Hildebrandt, P. Wust, O. Ahlers, A. Dieing, G. Sreenivasa, T. Kerner, R. Felix and H. Riess, *Critical Reviews in Oncology/Hematology*, 2002, 43, 33-56.

2. J. L. Roti Roti, *International Journal of Hyperthermia*, 2008, 24, 3-15.
3. A. Chichel, J. Skowronek, M. Kubaszewska and M. Kanikowski, *Reports of Practical Oncology & Radiotherapy*, 2007, 12, 267-275.
4. P. Wust, B. Hildebrandt, G. Sreenivasa, B. Rau, J. Gellermann, H. Riess, R. Felix and P. M. Schlag, *Lancet Oncology*, 2002, 3, 487-497.
5. A. Burlaka, S. Lukin, S. Prylutska, O. Remeniak, Y. Prylutsky, M. Shuba, S. Maksimenko, U. Ritter and P. Scharff, *Experimental Oncology*, 2010, 32, 48-50.
6. P. A. Mackowiak, *Principles and practice of infectious diseases*, 2000, 6, 703-718.
7. C. A. Wunderlich, *On the temperature in diseases*, The New Sydenham Society, 1871.
8. N. P. O'Grady, P. S. Barie, J. G. Bartlett, T. Bleck, G. Garvey, J. Jacobi, P. Linden, D. G. Maki, M. Nam and W. Pasculle, *Clinical Infectious Diseases*, 1998, 26, 1042-1059.
9. J. Van der Zee, *Annals of Oncology*, 2002, 13, 1173-1184.
10. H.-U. Hobohm, *Healing heat: An essay on cancer immune defence*, BoD-Books on Demand, 2009.
11. R. W. Habash, R. Bansal, D. Krewski and H. T. Alhafid, *Critical Reviews in Biomedical Engineering*, 2006, 34, 491-542.
12. R. W. Habash, R. Bansal, D. Krewski and H. T. Alhafid, *Critical Reviews in Biomedical Engineering*, 2006, 34, 459-489.
13. M. Johannsen, U. Gneveckow, L. Eckelt, A. Feussner, N. Waldofner, R. Scholz, S. Deger, P. Wust, S. A. Loening and A. Jordan, *International Journal of Hyperthermia*, 2005, 21, 637-647.
14. J. Mendecki, E. Friedenthal, C. Botstein, R. Paglione and F. Sterzer, *International Journal of Radiation Oncology* Biology* Physics*, 1980, 6, 1583-1588.
15. G. Hegyi, G. P. Szigeti and A. Szasz, *Evid Based Complement Alternat Med*, 2013, 2013, 672873.
16. F. Zhou, D. Xing, Z. Ou, B. Wu, D. E. Resasco and W. R. Chen, *Journal of Biomedical Optics*, 2009, 14, 021009.
17. J. W. Fisher, S. Sarkar, C. F. Buchanan, C. S. Szot, J. Whitney, H. C. Hatcher, S. V. Torti, C. G. Rylander and M. N. Rylander, *Cancer Research*, 2010, 70, 9855-9864.
18. T. Hironobu, N. Takuro, N. Ayuko, N. Yasuro and Y. Sunao, *Nanotechnology*, 2006, 17, 4431.
19. C. W. Song, *Cancer Research*, 1984, 44, 4721s-4730s.
20. S. S. Chen and J. Humphrey, *Journal of Biomechanics*, 1997, 31, 211-216.
21. J. R. Oleson, T. V. Samulski, K. A. Leopold, S. T. Clegg, M. W. Dewhirst, R. K. Dodge and S. L. George, *International Journal of Radiation Oncology* Biology* Physics*, 1993, 25, 289-297.
22. R. W. Habash, R. Bansal, D. Krewski and H. T. Alhafid, *Critical Reviews in Biomedical Engineering*, 2007, 35, 123-182.
23. P. Chakravarty, R. Marches, N. S. Zimmerman, A. D. Swafford, P. Bajaj, I. H. Musselman, P. Pantano, R. K. Draper and E. S. Vitetta, *Proceedings of the National Academy of Sciences of the USA*, 2008, 105, 8697-8702.
24. R. W. Habash, R. Bansal, D. Krewski and H. T. Alhafid, *Critical Reviews in Biomedical Engineering*, 2007, 35, 37-121.
25. S. V. Torti, F. Byrne, O. Whelan, N. Levi, B. Ucer, M. Schmid, F. M. Torti, S. Akman, J. Liu, P. M. Ajayan, O. Nalamasu and D. L. Carroll, *International Journal of Nanomedicine*, 2007, 2, 707-714.
26. S. N. Goldberg, J. B. Kruskal and G. S. Gazelle, 1999.
27. C. J. Diederich, *International Journal of Hyperthermia*, 2005, 21, 745-753.
28. B. J. Wood, Z. Neeman and A. Kam, in *Tumor Ablation*, Springer, 2005, pp. 285-300.
29. T. Corwin, G. Lindberg, O. Traxer, M. T. Gettman, T. G. Smith, M. S. Pearle and J. A. Cadeddu, *The Journal of Urology*, 2001, 166, 281-284.
30. F. Litvack, W. S. Grundfest, T. Papaioannou, F. W. Mohr, A. T. Jakubowski and J. S. Forrester, *The American Journal of Cardiology*, 1988, 61, 81G-86G.
31. S. Rastegar, M. Motamedi, A. J. Welch and L. J. Hayes, *Ieee Transactions on Biomedical Engineering*, 1989, 36, 1180-1187.
32. A. J. Welch, M. Motamedi, S. Rastegar, G. L. Lecarpentier and D. Jansen, *Photochemistry and Photobiology*, 1991, 53, 815-823.
33. S. A. Sapareto and W. C. Dewey, *International Journal of Radiation Oncology* Biology* Physics*, 1984, 10, 787-800.
34. A. Buseti, M. Soncin, E. Reddi, M. A. Rodgers, M. E. Kenney and G. Jori, *Journal of Photochemistry and Photobiology B: Biology*, 1999, 53, 103-109.
35. J. R. Lepock, K.-H. Cheng, H. Al-qysi, I. Sim, C. J. Koch and J. Kruuv, *International Journal of Hyperthermia*, 1987, 3, 123-132.
36. J. R. Lepock, H. E. Frey, A. M. Rodahl and J. Kruuv, *Journal of cellular physiology*, 1988, 137, 14-24.
37. A. E. Caccamo, S. Desenzani, L. Belloni, A. F. Borghetti and S. Bettuzzi, *Journal of Cellular Physiology*, 2006, 207, 208-219.
38. K. J. Henle and L. A. Dethlefsen, *Cancer Research*, 1978, 38, 1843-1851.
39. B. W. Henderson and V. H. Fingar, *Cancer Research*, 1987, 47, 3110-3114.
40. M. Ahmed, *International Journal of Hyperthermia*, 2004, 20, 781-802.
41. L. E. Gerweck, *Cancer Research*, 1985, 45, 3408-3414.
42. V. K. Pustovalov, L. G. Astafyeva and W. Fritzsche, *Nano Energy*, 2013, 2, 1137-1141.
43. M. P. V. Shekhar, *Current Cancer Drug Targets*, 2011, 11, 613-623.
44. C. L. Garrett, D. O. Draper and K. L. Knight, *Journal of Athletic Training*, 2000, 35, 50-55.
45. N. A. Armar and G. C. L. Lachelin, *BJOG: An International Journal of Obstetrics & Gynaecology*, 1993, 100, 161-164.
46. U. G. Longo, M. Ronga and N. Maffulli, *Sports Medicine and Arthroscopy Review*, 2009, 17, 112-126.
47. H. I. Bicher, F. W. Hetzel, T. S. Sandhu, S. Frinak, P. Vaupel, M. O'hara and T. O'brien, *Radiology*, 1980, 137, 523-530.
48. J. G. Short and P. F. Turner, *Proceedings of the IEEE*, 1980, 68, 133-142.
49. A. I. Minchinton and I. F. Tannock, *Nature Reviews Cancer*, 2006, 6, 583-592.
50. S. H. van Rijt and P. J. Sadler, *Drug Discovery Today*, 2009, 14, 1089-1097.
51. Y. Lee, S. L. Auh, Y. Wang, B. Burnette, Y. Wang, Y. Meng, M. Beckett, R. Sharma, R. Chin and T. Tu, *Blood*, 2009, 114, 589-595.
52. A. A. Lugade, J. P. Moran, S. A. Gerber, R. C. Rose, J. G. Frelinger and E. M. Lord, *The Journal of Immunology*, 2005, 174, 7516-7523.
53. T. J. Dougherty, C. J. Gomer, B. W. Henderson, G. Jori, D. Kessel, M. Korbelik, J. Moan and Q. Peng, *Journal of the National Cancer Institute*, 1998, 90, 889-905.
54. M. P. Carey and T. G. Burish, *Psychological Bulletin*, 1988, 104, 307.
55. J. E. Johnson, L. M. Nail, D. Lauver, K. B. King and H. Keys, *Cancer*, 1988, 61, 46-51.
56. M. Clarke, R. Collins, S. Darby, C. Davies, P. Elphinstone, E. Evans, J. Godwin, R. Gray, C. Hicks and S. James, *Lancet*, 2005, 366, 2087-2106.
57. I. Takahashi, Y. Emi, S. Hasuda, Y. Kakeji, Y. Maehara and K. Sugimachi, *Surgery*, 2002, 131, S78-S84.
58. E. L. Jones, J. R. Oleson, L. R. Prosnitz, T. V. Samulski, Z. Vujaskovic, D. Yu, L. L. Sanders and M. W. Dewhirst, *Journal of Clinical Oncology*, 2005, 23, 3079-3085.
59. J. B. Marmor, D. Pounds, T. B. Postic and G. M. Hahn, *Cancer*, 1979, 43, 188-197.
60. L. O. Svaasand, T. Boerslid and M. Oeveraasen, *Lasers in surgery and medicine*, 1985, 5, 589-602.

61. A. Y. Cheung and A. Neyzari, *Cancer Research*, 1984, 44, 4736s-4744s.
62. *US Pat.*, US6432067 B1, 1999.
63. *US Pat.*, US5807395 A, 1998.
64. *US Pat.*, US4662383 A, 1987.
65. W. Hurter, F. Reinbold and W. Lorenz, *Microwave Theory and Techniques, IEEE Transactions on*, 1991, 39, 1048-1054.
66. J. Delannoy, D. LeBihan, D. Hoult and R. Levin, *Medical physics*, 1990, 17, 855.
67. *CA Pat.*, CA2365002 A1, 2001.
68. B. S. Tremblay, *Biomedical Engineering, IEEE Transactions on*, 1985, 152-157.
69. B. E. Lyons, R. H. Britt and J. W. Strohbehn, *Biomedical Engineering, IEEE Transactions on*, 1984, 53-62.
70. M. Johannsen, B. Thiesen, P. Wust and A. Jordan, *International Journal of Hyperthermia*, 2010, 26, 790-795.
71. M. Salloum, R. Ma, D. Weeks and L. Zhu, *International Journal of Hyperthermia*, 2008, 24, 337-345.
72. G. Kong, R. D. Braun and M. W. Dewhirst, *Cancer Research*, 2000, 60, 4440-4445.
73. S. Mornet, S. Vasseur, F. Grasset and E. Duguet, *Journal of Materials Chemistry*, 2004, 14, 2161-2175.
74. Q. A. Pankhurst, J. Connolly, S. Jones and J. Dobson, *Journal of Physics D: Applied Physics*, 2003, 36, R167.
75. R. Hergt, S. Dutz, R. Müller and M. Zeisberger, *Journal of Physics: Condensed Matter*, 2006, 18, S2919.
76. B. Thiesen and A. Jordan, *International Journal of Hyperthermia*, 2008, 24, 467-474.
77. A. Ito, M. Shinkai, H. Honda and T. Kobayashi, *Journal of Bioscience and Bioengineering*, 2005, 100, 1-11.
78. R. K. Gilchrist, R. Medal, W. D. Shorey, R. C. Hanselman, J. C. Parrott and C. B. Taylor, *Annals of Surgery*, 1957, 146, 596-606.
79. M. Johannsen, U. Gneveckow, K. Taymoorian, B. Thiesen, N. Waldofner, R. Scholz, K. Jung, A. Jordan, P. Wust and S. A. Loening, *Int J Hyperthermia*, 2007, 23, 315-323.
80. B. A. Moffat, G. R. Reddy, P. McConville, D. E. Hall, T. L. Chenevert, R. R. Kopelman, M. Philbert, R. Weissleder, A. Rehemtulla and B. D. Ross, *Molecular Imaging*, 2003, 2, 324-332.
81. D. Pissuwan, S. M. Valenzuela and M. B. Cortie, *TRENDS in Biotechnology*, 2006, 24, 62-67.
82. X. H. Huang, P. K. Jain, I. H. El-Sayed and M. A. El-Sayed, *Lasers in Medical Science*, 2008, 23, 217-228.
83. X. Huang, I. H. El-Sayed, W. Qian and M. A. El-Sayed, *Journal of the American Chemical Society*, 2006, 128, 2115-2120.
84. P. K. Jain, X. Huang, I. H. El-Sayed and M. A. El-Sayed, *Accounts of Chemical Research*, 2008, 41, 1578-1586.
85. M. Marsh, E. Schelew, S. Wolf and T. Skippon, *Queen's University, Kingston*, 2009, 29.
86. A. M. Smith, M. C. Mancini and S. Nie, *Nature Nanotechnology*, 2009, 4, 710-711.
87. R. Weissleder, *Nature Biotechnology*, 2001, 19, 316-317.
88. K. König, *Journal of Microscopy*, 2000, 200, 83-104.
89. F. Helmchen and W. Denk, *Nature Methods*, 2005, 2, 932-940.
90. M. P. Melancon, M. Zhou and C. Li, *Accounts of chemical research*, 2011, 44, 947-956.
91. G. S. Terentyuk, G. N. Maslyakova, L. V. Suleymanova, N. G. Khlebtsov and B. N. Khlebtsov, *Journal of Biomedical Optics*, 2009, 14, 021016.
92. M. Olivo, C. Y. Fu, V. Raghavan and W. K. Lau, *Annals of Biomedical Engineering*, 2012, 40, 460-473.
93. M. A. Albota, C. Xu and W. W. Webb, *Applied Optics*, 1998, 37, 7352-7356.
94. J. G. Teeguarden, P. M. Hinderliter, G. Orr, B. D. Thrall and J. G. Pounds, *Toxicological Sciences*, 2007, 95, 300-312.
95. M. S. Nikolic, M. Krack, V. Aleksandrovic, A. Kornowski, S. Förster and H. Weller, *Angewandte Chemie International Edition*, 2006, 45, 6577-6580.
96. X. Shi, S. Wang, H. Sun and J. R. Baker, *Soft Matter*, 2006, 3, 71-74.
97. W. W. Yu, E. Chang, R. Drezek and V. L. Colvin, *Biochemical and Biophysical Research Communications*, 2006, 348, 781-786.
98. N. R. Jana, C. Earhart and J. Y. Ying, *Chemistry of Materials*, 2007, 19, 5074-5082.
99. J.-s. Choi, Y.-w. Jun, S.-I. Yeon, H. C. Kim, J.-S. Shin and J. Cheon, *Journal of the American Chemical Society*, 2006, 128, 15982-15983.
100. X. Hong, Z. Wang, W. Cai, F. Lu, J. Zhang, Y. Yang, N. Ma and Y. Liu, *Chemistry of Materials*, 2005, 17, 1548-1552.
101. J. R. McCarthy, E. Korngold, R. Weissleder and F. A. Jaffer, *Small*, 2010, 6, 2041-2049.
102. A. Barhoumi, R. Huschka, R. Bardhan, M. W. Knight and N. J. Halas, *Chemical Physics Letters*, 2009, 482, 171-179.
103. U. Rocha, K. U. Kumar, C. Jacinto, I. Villa, F. Sanz-Rodríguez, M. del Carmen Iglesias de la Cruz, A. Juarranz, E. Carrasco, F. C. J. M. van Veggel, E. Bovero, J. G. Solé and D. Jaque, *Small*, 2013, DOI: 10.1002/smll.201301716.
104. H. Huang, S. Delikanli, H. Zeng, D. M. Ferkey and A. Pralle, *Nature nanotechnology*, 2010, 5, 602-606.
105. L. Cheng, K. Yang, Q. Chen and Z. Liu, *ACS Nano*, 2012, 6, 5605-5613.
106. L. M. Maestro, P. Haro-Gonzalez, B. del Rosal, J. Ramiro, A. J. Caamano, E. Carrasco, A. Juarranz, F. Sanz-Rodríguez, J. G. Sole and D. Jaque, *Nanoscale*, 2013, 5, 7882-7889.
107. S. Link and M. A. El-Sayed, *International Reviews in Physical Chemistry*, 2000, 19, 409-453.
108. S. Link and M. A. El-Sayed, *Journal of Physical Chemistry B*, 1999, 103, 4212-4217.
109. G. Mie, *Annalen der Physik*, 1908, 330, 377-445.
110. J. F. Lovell, C. S. Jin, E. Huynh, H. Jin and C. Kim, *Nature Materials*, 2011, 10, 324-332.
111. S. K. Ghosh and T. Pal, *Chemical Reviews*, 2007, 107, 4797-4862.
112. P. K. Jain, I. H. El-Sayed and M. A. El-Sayed, *Nano Today*, 2007, 2, 18-29.
113. S. E. Skrabalak, J. Chen, L. Au, X. Lu, X. Li and Y. Xia, *Advanced Materials*, 2007, 19, 3177-3184.
114. E. Carbo-Argibay, B. Rodriguez-Gonzalez, J. Pacifico, I. Pastoriza-Santos, J. Perez-Juste and L. M. Liz-Marzan, *Angew Chem Int Ed Engl*, 2007, 46, 8983-8987.
115. J. Pérez-Juste, I. Pastoriza-Santos, L. M. Liz-Marzán and P. Mulvaney, *Coordination Chemistry Reviews*, 2005, 249, 1870-1901.
116. P. K. Jain, K. S. Lee, I. H. El-Sayed and M. A. El-Sayed, *The Journal of Physical Chemistry B*, 2006, 110, 7238-7248.
117. L. Maestro, P. Haro-González, J. Coello and D. Jaque, *Applied Physics Letters*, 2012, 100, 201110-201114.
118. E. Prodan, P. Nordlander and N. J. Halas, *Nano Letters*, 2003, 3, 1411-1415.
119. S. J. Oldenburg, J. B. Jackson, S. L. Westcott and N. J. Halas, *Applied Physics Letters*, 1999, 75, 2897-2899.
120. A. M. Fales, H. Yuan and T. Vo-Dinh, *Langmuir*, 2011, 27, 12186-12190.
121. R. Rodríguez-Oliveros and J. A. Sánchez-Gil, *Opt. Express*, 2012, 20, 621-626.
122. H. Yuan, C. G. Houry, C. M. Wilson, G. A. Grant, A. J. Bennett and T. Vo-Dinh, *Nanomedicine*, 2012, 8, 1355-1363.
123. S. Trigari, A. Rindi, G. Margheri, S. Sottini, G. Dellepiane and E. Giorgetti, *Journal of Materials Chemistry*, 2011, 21, 6531-6540.
124. J. Chen, B. Wiley, Z. Y. Li, D. Campbell, F. Saeki, H. Cang, L. Au, J. Lee, X. Li and Y. Xia, *Advanced Materials*, 2005, 17, 2255-2261.
125. M. F. Tsai, S. H. Chang, F. Y. Cheng, V. Shanmugam, Y. S. Cheng, C. H. Su and C. S. Yeh, *ACS Nano*, 2013, 7, 5330-5342.
126. Y. Jin, J. Wang, H. Ke, S. Wang and Z. Dai, *Biomaterials*, 2013, 34, 4794-4802.
127. H. Ke, J. Wang, Z. Dai, Y. Jin, E. Qu, Z. Xing, C. Guo, X. Yue and J. Liu, *Angewandte Chemie (International ed. in English)*, 2011, 50, 3017-3021.

128. H. Ke, J. Wang, S. Tong, Y. Jin, S. Wang, E. Qu, G. Bao and Z. Dai, *Theranostics*, 2013, 4, 12-23.
129. H. Ke, X. Yue, J. Wang, S. Xing, Q. Zhang, Z. Dai, J. Tian, S. Wang and Y. Jin, *Small*, 2014, 10, 1220-1227.
- 5 130. S. C. Boca, M. Potara, A. M. Gabudean, A. Juhem, P. L. Baldeck and S. Astilean, *Cancer Letters*, 2011, 311, 131-140.
131. G. Fu, W. Liu, S. Feng and X. Yue, *Chemical Communications*, 2012, 48, 11567-11569.
132. M. Shokouhimehr, E. S. Soehnlén, A. Khitrin, S. Basu and S. P. D. Huang, *Inorganic Chemistry Communications*, 2010, 13, 58-61.
- 10 133. M. Shokouhimehr, E. S. Soehnlén, J. H. Hao, M. Griswold, C. Flask, X. D. Fan, J. P. Basilion, S. Basu and S. P. D. Huang, *Journal of Materials Chemistry*, 2010, 20, 5251-5259.
- 15 134. N. H. Levi-Polyachenko, E. J. Merkel, B. T. Jones, D. L. Carroll and J. H. Stewart, *Molecular Pharmaceutics*, 2009, 6, 1092-1099.
135. S. J. Yu, M. W. Kang, H. C. Chang, K. M. Chen and Y. C. Yu, *Journal of the American Chemical Society*, 2005, 127, 17604-17605.
- 20 136. G. Kucsko, P. C. Maurer, N. Y. Yao, M. Kubo and H. J. Noh, *Nature*, 2013, 500, 54-58.
137. S. Iijima, *Nature*, 1991, 354, 56-58.
138. J. T. Robinson, S. M. Tabakman, Y. Y. Liang, H. L. Wang, H. S. Casalongue, D. Vinh and H. J. Dai, *Journal of the American Chemical Society*, 2011, 133, 6825-6831.
- 25 139. X. Sun, Z. Liu, K. Welsher, J. Robinson, A. Goodwin, S. Zaric and H. Dai, *Nano Research*, 2008, 1, 203-212.
140. F. Wang, G. Dukovic, L. E. Brus and T. F. Heinz, *Science*, 2005, 308, 838-841.
- 30 141. M. S. Strano, S. K. Doorn, E. H. Haroz, C. Kittrell and R. H. Hauge, *Nano letters*, 2003, 3, 1091-1096.
142. L. Van Hove, *Physical Review*, 1953, 89, 1189-1193.
143. T. Stöckli, Z. L. Wang, J. M. Bonard, P. Sadelmann and A. Chatelain, *Philosophical Magazine Part B*, 1999, 79, 1531-1548.
- 35 144. A. V. Naumov, S. Ghosh, D. A. Tsybolski, S. M. Bachilo and R. B. Weisman, *ACS Nano*, 2011, 5, 1639-1648.
145. M. J. O'Connell, S. M. Bachilo, C. B. Huffman, V. C. Moore, M. S. Strano, E. H. Haroz, K. L. Rialon, P. J. Boul, W. H. Noon, C. Kittrell, J. Ma, R. H. Hauge, R. B. Weisman and R. E. Smalley, *Science*, 2002, 297, 593-596.
146. F. Wang, G. Dukovic, L. E. Brus and T. F. Heinz, *Physical Review Letters*, 2004, 92, 177401.
- 45 147. J. Crochet, M. Clemens and T. Hertel, *Journal of the American Chemical Society*, 2007, 129, 8058-8059.
148. S.-Y. Ju, W. P. Kopcha and F. Papadimitrakopoulos, *Science*, 2009, 323, 1319-1323.
149. M. Lin and K. W. K. Shung, *Physical Review B, Condensed Matter*, 1994, 50, 17744-17747.
- 50 150. B. Zhao, M. E. Itkis, S. Niyogi, H. Hu, J. Zhang and R. C. Haddon, *The Journal of Physical Chemistry B*, 2004, 108, 8136-8141.
151. F. Schöppler, C. Mann, T. C. Hain, F. M. Neubauer, G. Privitera, F. Bonaccorso, D. Chu, A. C. Ferrari and T. Hertel, *The Journal of Physical Chemistry C*, 2011, 115, 14682-14686.
- 55 152. Q. Cheng, S. Debnath, E. Gregan and H. J. Byrne, *The Journal of Physical Chemistry C*, 2008, 112, 20154-20158.
- 60 153. A. Burke, X. Ding, R. Singh, R. A. Kraft, N. Levi-Polyachenko, M. N. Rylander, C. Szot, C. Buchanan, J. Whitney, J. Fisher, H. C. Hatcher, R. D'Agostino, Jr., N. D. Kock, P. M. Ajayan, D. L. Carroll, S. Akman, F. M. Torti and S. V. Torti, *Proceedings of the National Academy of Sciences of the USA*, 2009, 106, 12897-12902.
- 65 154. S. H. Jeong, K. K. Kim, S. J. Jeong, K. H. An, S. H. Lee and Y. H. Lee, *Synthetic Metals*, 2007, 157, 570-574.
155. S. H. Kim, G. W. Mulholland and M. R. Zachariah, *Carbon*, 2009, 47, 1297-1302.
- 70 156. L. M. Maestro, E. M. Rodriguez, F. Vetrone, R. Naccache, H. L. Ramirez, D. Jaque, J. A. Capobianco and J. G. Solé, *Opt. Express*, 2010, 18, 23544-23553.
157. I. L. Medintz, H. T. Uyeda, E. R. Goldman and H. Mattoussi, *Nature Materials*, 2005, 4, 435-446.
- 75 158. N. Lewinski, V. Colvin and R. Drezek, *Small*, 2008, 4, 26-49.
159. K. T. Yong, W. C. Law, R. Hu, L. Ye, L. Liu, M. T. Swihart and P. N. Prasad, *Chemical Society Reviews*, 2013, 42, 1236-1250.
160. L. M. Maestro, P. Haro-González, M. C. Iglesias-de la Cruz, F. SanzRodríguez, Á. Juarranz, J. G. Solé and D. Jaque, *Nanomedicine*, 2013, 8, 379-388.
- 80 161. S. B. Lakshmanan, X. Zou, M. Hossu, L. Ma, C. Yang and W. Chen, *Journal of Biomedical Nanotechnology*, 2012, 8, 883-890.
- 85 162. Q. Tian, M. Tang, Y. Sun, R. Zou, Z. Chen, M. Zhu, S. Yang, J. Wang, J. Wang and J. Hu, *Advanced Materials*, 2011, 23, 3542-3547.
163. A. M. Derfus, W. C. W. Chan and S. N. Bhatia, *Nano Letters*, 2004, 4, 11-18.
- 90 164. Y. Li, W. Lu, Q. Huang, C. Li and W. Chen, *Nanomedicine*, 2010, 5, 1161-1171.
165. V. M. Garcia, P. K. Nair and M. T. S. Nair, *Journal of Crystal Growth*, 1999, 203, 113-124.
166. C. M. Hessel, V. P. Pattani, M. Rasch, M. G. Panthani, B. Koo, J. W. Tunnell and B. A. Korgel, *Nano Letters*, 2011, 11, 2560-2566.
- 95 167. Y. Zhao, H. Pan, Y. Lou, X. Qiu, J. Zhu and C. Burda, *Journal of the American Chemical Society*, 2009, 131, 4253-4261.
168. J. M. Luther, P. K. Jain, T. Ewers and A. P. Alivisatos, *Nature Materials*, 2011, 10, 361-366.
- 100 169. T. N. Lambert, N. L. Andrews, H. Gerung, T. J. Boyle, J. M. Oliver, B. S. Wilson and S. M. Han, *Small*, 2007, 3, 691-699.
170. G. Chen, T. Y. Ohulchanskyy, S. Liu, W.-C. Law, F. Wu, M. T. Swihart, H. Ågren and P. N. Prasad, *ACS Nano*, 2012, 6, 2969-2977.
- 105 171. G. Chen, J. Shen, T. Y. Ohulchanskyy, N. J. Patel, A. Kutikov, Z. Li, J. Song, R. K. Pandey, H. Ågren, P. N. Prasad and G. Han, *ACS Nano*, 2012, 6, 8280-8287.
172. F. Vetrone, R. Naccache, A. Juarranz de la Fuente, F. Sanz-Rodriguez, A. Blazquez-Castro, E. M. Rodriguez, D. Jaque, J. G. Solé and J. A. Capobianco, *Nanoscale*, 2010, 2, 495-498.
- 110 173. D. Jaque and F. Vetrone, *Nanoscale*, 2012, 4, 4301-4326.
174. A. Gnach and A. Bednarkiewicz, *Nano Today*, 2012, 7, 532-563.
- 115 175. J. G. Solé, L. E. Bausá and D. Jaque, in *An Introduction to the Optical Spectroscopy of Inorganic Solids*, John Wiley & Sons, Ltd, 2005, DOI: 10.1002/0470016043.fmatter, pp. i-xx.
176. A. A. Ansari, S. P. Singh, N. Singh and B. D. Malhotra, *Spectrochimica Acta Part A: Molecular and Biomolecular Spectroscopy*, 2012, 86, 432-436.
- 120 177. D. Wawrzynczyk, A. Bednarkiewicz, M. Nyk, W. Strek and M. Samoc, *Nanoscale*, 2012, 4, 6959-6961.
178. A. Bednarkiewicz, D. Wawrzynczyk, M. Nyk and W. Strek, *Applied Physics B*, 2010, 103, 847-852.
- 125 179. V. K. Tikhomirov, K. Driesen, V. D. Rodriguez, P. Gredin and M. Mortier, *Opt. Express*, 2009, 17, 11794-11798.
180. U. Rocha, C. Jacinto da Silva, W. Ferreira Silva, I. Guedes, A. Benayas, L. Martínez Maestro, M. Acosta Elias, E. Bovero, F. C. J. M. van Veggel, J. A. García Solé and D. Jaque, *ACS Nano*, 2013, 7, 1188-1199.
- 130 181. M. Ge, J. Rong, X. Fang, A. Zhang, Y. Lu and C. Zhou, *Nano Research*, 2013, 6, 174-181.
182. A. G. Cullis, L. T. Canham and P. D. J. Calcott, *Journal of Applied Physics*, 1997, 82, 909-965.
- 135 183. S. P. Low, N. H. Voelcker, L. T. Canham and K. A. Williams, *Biomaterials*, 2009, 30, 2873-2880.
184. L. Xiao, L. Gu, S. B. Howell and M. J. Sailor, *ACS Nano*, 2011, 5, 3651-3659.
185. E. J. Anglin, L. Cheng, W. R. Freeman and M. J. Sailor, *Advanced Drug Delivery Reviews*, 2008, 60, 1266-1277.
- 140 186. E. Secret, K. Smith, V. Dubljevic, E. Moore, P. Macardle, B. Delalat, M. L. Rogers, T. G. Johns, J. O. Durand, F. Cunin and N. H. Voelcker, *Advanced Healthcare Materials*, 2013, 2, 718-727.

187. J.-H. Park, L. Gu, G. von Maltzahn, E. Ruoslahti, S. N. Bhatia and M. J. Sailor, *Nature Materials*, 2009, 8, 331-336.
188. D. Gallach, G. Recio Sánchez, A. Muñoz Noval, M. Manso Silván, G. Ceccone, R. J. Martín Palma, V. Torres Costa and J. M. Martínez Duart, *Materials Science and Engineering: B*, 2010, 169, 123-127.
189. C. Lee, H. Kim, C. Hong, M. Kim, S. S. Hong, D. H. Lee and W. I. Lee, *Journal of Materials Chemistry*, 2008, 18, 4790-4795.
190. C. Lee, C. Hong, J. Lee, M. Son and S.-S. Hong, *Lasers in Medical Science*, 2012, 27, 1001-1008.
191. I. Sagnes, A. Halimaoui, G. Vincent and P. A. Badoz, *Applied physics letters*, 1993, 62, 1155-1157.
192. J. Yu, D. Javier, M. A. Yaseen, N. Nitin and R. Richards-Kortum, *Journal of the American Chemical Society*, 2010, 132, 1929-1938.
193. J. Yang, J. Choi, D. Bang, E. Kim, E. K. Lim, H. Park, J. S. Suh, K. Lee, K. H. Yoo, E. K. Kim, Y. M. Huh and S. Haam, *Angew Chem Int Ed Engl*, 2011, 50, 441-444.
194. S. Sharifi, S. Behzadi, S. Laurent, M. L. Forrest and P. Stroeve, *Chemical Society Reviews*, 2012, 41, 2323-2343.
195. H. Shinohara, A. Tanaka, T. Kitai, N. Yanabu and T. Inomoto, *Hepatology*, 1996, 23, 137-144.
196. M. Zheng, C. Yue, Y. Ma, P. Gong, P. Zhao, C. Zheng, Z. Sheng, P. Zhang, Z. Wang and L. Cai, *ACS Nano*, 2013, 7, 2056-2067.
197. B. Jung, A. L. N. Rao and B. Anvari, *ACS Nano*, 2011, 5, 1243-1252.
198. S. Gupta, M. R. Chatni, A. L. N. Rao, V. I. Vullev, L. V. Wang and B. Anvari, *Nanoscale*, 2013, 5, 1772-1776.
199. B. Bahmani, D. Bacon and B. Anvari, *Scientific Reports*, 2013, 3, 3.
200. Y. Ma, S. Tong, G. Bao, C. Gao and Z. Dai, *Biomaterials*, 2013, 34, 7706-7714.
201. C.-Y. Li, W.-Y. Chiu and C.-F. Lee, *e-Polymers*, 2007, 7, 164-180.
202. O. P. Dimitriev, *Macromolecules*, 2004, 37, 3388-3395.
203. L. Cheng, W. He, H. Gong, C. Wang, Q. Chen, Z. Cheng and Z. Liu, *Advanced Functional Materials*, 2013, DOI: 10.1002/adfm.201301045, n/a-n/a.
204. M. Soncin, A. Busetti, F. Fusi, G. Jori and M. A. J. Rodgers, *Photochemistry and Photobiology*, 1999, 69, 708-712.
205. C. S. Jin, J. F. Lovell, J. Chen and G. Zheng, *ACS Nano*, 2013, 7, 2541-2550.
206. L. Martínez Maestro, P. Haro-González, A. Sánchez-Iglesias, L. M. Liz-Marzán, J. A. García Sole and D. Jaque, *Langmuir*, 2014, DOI: 10.1021/la403435v.
207. Z. Zha, X. Yue, Q. Ren and Z. Dai, *Advanced Materials*, 2013, 25, 777-782.
208. Z. Zha, J. Wang, S. Zhang, S. Wang, E. Qu, Y. Zhang and Z. Dai, *Biomaterials*, 2014, 35, 287-293.
209. Y. Ma, X. Liang, S. Tong, G. Bao, Q. Ren and Z. Dai, *Advanced Functional Materials*, 2013, 23, 815-822.
210. J. Turkevich, P. C. Stevenson and J. Hillier, *The Journal of Physical Chemistry*, 1953, 57, 670-673.
211. G. Frens, *Nature Physical Science*, 1973, 241, 20-22.
212. W. S. Sutherland and J. D. Winefordner, *Journal of Colloid and Interface Science*, 1992, 148, 129-141.
213. K. C. Grabar, R. G. Freeman, M. B. Hommer and M. J. Natan, *Analytical chemistry (Washington)*, 1995, 67, 735-743.
214. Z. Liang, J. Zhang, L. Wang, S. Song and C. Fan, *International journal of molecular sciences*, 2007, 8, 526-532.
215. M. Brust, M. Walker, D. Bethell, D. J. Schiffrin and R. Whyman, *Journal of the Chemical Society, Chemical Communications*, 1994, DOI: 10.1039/c39940000801, 801.
216. J. L. Plaza and V. Carcelen, *Applied Surface Science*, 2009, 255, 6164-6167.
217. X. Wang, J. Zhuang, Q. Peng and Y. D. Li, *Nature*, 2005, 437, 121-124.
218. C. J. Murphy and N. R. Jana, *Advanced Materials*, 2002, 14, 80-82.
219. B. Nikoobakht and M. A. El-Sayed, *Langmuir*, 2001, 17, 6368-6374.
220. E. B. Dickerson, E. C. Dreaden, X. H. Huang, I. H. El-Sayed, H. H. Chu, S. Pushpanketh, J. F. McDonald and M. A. El-Sayed, *Cancer Letters*, 2008, 269, 57-66.
221. F. M. Veronese and G. Pasut, *Drug Discovery Today*, 2005, 10, 1451-1458.
222. J. R. Cole, N. A. Mirin, M. W. Knight, G. P. Goodrich and N. J. Halas, *The Journal of Physical Chemistry C*, 2009, 113, 12090-12094.
223. G. P. Goodrich, L. Bao, K. Gill-Sharp, K. L. Sang and J. Wang, *Journal of Biomedical Optics*, 2010, 15, 018001.
224. Q. Zhang, W. Li, L. P. Wen, J. Chen and Y. Xia, *Chemistry*, 2010, 16, 10234-10239.
225. S. E. Skrabalak, J. Chen, Y. Sun, X. Lu and L. Au, *Accounts of chemical research*, 2008, 41, 1587-1595.
226. J. Chen, M. Yang, Q. Zhang, E. C. Cho, C. M. Cobley, C. Kim, C. Glaus, L. V. Wang, M. J. Welch and Y. Xia, *Advanced Functional Materials*, 2010, 20, 3684-3694.
227. M. Hu, J. Chen, Z.-Y. Li, L. Au, G. V. Hartland, X. Li, M. Marquez and Y. Xia, *Chemical Society Reviews*, 2006, 35, 1084-1094.
228. C. Journet, W. K. Maser, P. Bernier, A. Loiseau and M. L. delaChapelle, *Nature*, 1997, 388, 756-758.
229. M. C. Altay and S. Eroglu, *Journal of Crystal Growth*, 2013, 364, 40-45.
230. T. Guo, P. Nikolaev, A. Thess, D. T. Colbert and R. E. Smalley, *Chemical physics letters*, 1995, 243, 49-54.
231. M. Paradise and T. Goswami, *Materials in engineering*, 2007, 28, 1477-1489.
232. H. Dai, *Surface Science*, 2002, 500, 218-241.
233. Y. Uemura, K. Baba, H. Ohe, Y. Ohzuno and Y. Hatate, *Journal of Material Cycles and Waste Management*, 2003, 5, 94-97.
234. A.-C. Dupuis, *Progress in Materials Science*, 2005, 50, 929-961.
235. S. McCaldin, M. Bououdina, D. M. Grant and G. S. Walker, *Carbon (New York)*, 2006, 44, 2273-2280.
236. A. Thess, R. Lee, P. Nikolaev, H. J. Dai and P. Petit, *Science*, 1996, 273, 483-487.
237. A. Valizadeh, H. Mikaeili, M. Samiei, S. M. Farkhani, N. Zarghami, M. Kouhi, A. Akbarzadeh and S. Davaran, *Nanoscale Research Letters*, 2012, 7, 480.
238. D. Bera, L. Qian, T.-K. Tseng and P. H. Holloway, *Materials*, 2010, 3, 2260-2345.
239. L. Y. Zhang, L. Wen, J. J. Zhang and L. L. Hu, *Materials Chemistry and Physics*, 2005, 91, 166-171.
240. N. Bogdan, E. Martín Rodríguez, F. Sanz-Rodríguez, M. C. Iglesias de la Cruz, A. Juaranz, D. Jaque, J. García Sole and J. A. Capobianco, *Nanoscale*, 2012, 4, 3647-3650.
241. V. Mahalingam, F. Vetrone, R. Naccache, A. Speghini and J. A. Capobianco, *Advanced Materials*, 2009, 21, 4025-4028.
242. W. Zhang, Z. Guo, D. Huang, Z. Liu, X. Guo and H. Zhong, *Biomaterials*, 2011, 32, 8555-8561.
243. X. Teng, Y. Zhu, W. Wei, S. Wang, J. Huang, R. Naccache, W. Hu, A. I. Y. Tok, Y. Han, Q. Zhang, Q. Fan, W. Huang, J. A. Capobianco and L. Huang, *Journal of the American Chemical Society*, 2012, 134, 8340-8343.
244. F. Vetrone, R. Naccache, V. Mahalingam, C. G. Morgan and J. A. Capobianco, *Advanced Functional Materials*, 2009, 19, 2924-2929.
245. F. Wang, D. K. Chatterjee, Z. Q. Li, Y. Zhang, X. P. Fan and M. Q. Wang, *Nanotechnology*, 2006, 17, 5786-5791.
246. H. X. Mai, Y. W. Zhang, R. Si, Z. G. Yan, L. D. Sun, L. P. You and C. H. Yan, *Journal of the American Chemical Society*, 2006, 128, 6426-6436.
247. Y. Su, L. Li and G. Li, *Crystal Growth & Design*, 2008, 8, 2678-2683.
248. Zhuang, Liang, H. H. Y. Sung, Yang, Wu, I. D. Williams, Feng and Q. Su, *Inorganic Chemistry*, 2007, 46, 5404-5410.
249. F. Wang, D. Banerjee, Y. Liu, X. Chen and X. Liu, *Analyst*, 2010, 135, 1839-1854.
250. W. Zhou, X. Liu and J. Ji, *Journal of Nanoparticle Research*, 2012, 14, 1-16.

251. M. Aeschbacher, C. A. Reinhardt and G. Zbinden, *Cell Biology and Toxicology*, 1986, 2, 247-255.
252. B. Alberts, *Molecular biology of the cell*, Garland Science, New York, 2008.
- 5 253. E. C. Cho, L. Au, Q. Zhang and Y. Xia, *Small*, 2010, 6, 517-522.
254. L. Tong, Y. Zhao, T. B. Huff, M. N. Hansen, A. Wei and J. X. Cheng, *Adv Mater*, 2007, 19, 3136-3141.
255. T. B. Huff, L. Tong, Y. Zhao, M. N. Hansen, J. X. Cheng and A. Wei, *Nanomedicine*, 2007, 2, 125-132.
- 10 256. M. J. Waring, *Journal of Molecular Biology*, 1965, 13, 269-282.
257. C. H. Chou, C. D. Chen and C. R. C. Wang, *Journal of Physical Chemistry B*, 2005, 109, 11135-11138.
- 15 258. P. Prentice, A. Cuschierp, K. Dholakia, M. Prausnitz and P. Campbell, *Nature Physics*, 2005, 1, 107-110.
259. X. Huang, P. K. Jain, I. H. El-Sayed and M. A. El-Sayed, *Photochemistry and Photobiology*, 2006, 82, 412-417.
260. M. Longmire, P. L. Choyke and H. Kobayashi, *Nanomedicine*, 2008, 3, 703-717.
- 20 261. A. K. Gupta, R. R. Naregalkar, V. D. Vaidya and M. Gupta, *Nanomedicine*, 2007, 2, 23-39.
262. X. H. Gao, Y. Y. Cui, R. M. Levenson, L. W. K. Chung and S. M. Nie, *Nature Biotechnology*, 2004, 22, 969-976.
- 25 263. I. H. El-Sayed, X. Huang and M. A. El-Sayed, *Cancer Letters*, 2006, 239, 129-135.
264. M. S. Yavuz, Y. Cheng, J. Chen, C. M. Cobley, Q. Zhang, M. Rycenga, J. Xie, C. Kim, K. H. Song, A. G. Schwartz, L. V. Wang and Y. Xia, *Nature Materials*, 2009, 8, 935-939.
- 30 265. A. S. Hoffman, *Advanced Drug Delivery Reviews*, 2002, 54, 3-12.
266. B. D. Chithrani, A. A. Ghazani and W. C. W. Chan, *Nano Letters*, 2006, 6, 662-668.
267. B. D. Chithrani and W. C. W. Chan, *Nano Letters*, 2007, 7, 1542-1550.
- 35 268. F. Osaki, T. Kanamori, S. Sando, T. Sera and Y. Aoyama, *Journal of the American Chemical Society*, 2004, 126, 6520-6521.
269. J. D. Trono, K. Mizuno, N. Yusa, T. Matsukawa, K. Yokoyama and M. Uesaka, *Journal of Radiation Research*, 2011, 52, 103-109.
- 40 270. J. Davda and V. Labhasetwar, *International Journal of Pharmaceutics*, 2002, 233, 51-59.
271. X. Xing, X. He, J. Peng, K. Wang and W. Tan, *Journal of Nanoscience and Nanotechnology*, 2005, 5, 1688-1693.
- 45 272. S. J. H. Soenen, E. Illyes, D. Vercauteren, K. Braeckmans and Z. Majer, *Biomaterials*, 2009, 30, 6803-6813.
273. H. Y. Nam, S. M. Kwon, H. Chung, S.-Y. Lee, S.-H. Kwon, H. Jeon, Y. Kim, J. H. Park, J. Kim, S. Her, Y.-K. Oh, I. C. Kwon, K. Kim and S. Y. Jeong, *Journal of Controlled Release*, 2009, 135, 259-267.
- 50 274. J. L. Goldstein, R. G. W. Anderson and M. S. Brown, *Nature*, 1979, 279, 679-685.
275. L. Tong, Y. Lu, R. J. Lee and J.-X. Cheng, *The Journal of Physical Chemistry B*, 2007, 111, 9980-9985.
- 55 276. N. Tran and T. J. Webster, *Nanotechnology*, 2013, 24, 185102.
277. Y. Zhang, W. Chen, J. Zhang, J. Liu, G. Chen and C. Pope, *Journal of Nanoscience and Nanotechnology*, 2007, 7, 497-503.
- 60 278. N. Khlebtsov and L. Dykman, *Chemical Society Reviews*, 2011, 40, 1647-1671.
279. N. Zeng and A. B. Murphy, *Nanotechnology*, 2009, 20, 375702.
280. L. Tong, Q. Wei, A. Wei and J. X. Cheng, *Photochemistry and Photobiology*, 2009, 85, 21-32.
- 65 281. A. N. S. Institute, *Laser Institute of America, Orlando, FL*, 2000.
282. G. T. Charras, M. Coughlin, T. J. Mitchison and L. Mahadevan, *Biophysics Journal*, 2008, 94, 1836-1853.
- 70 283. J. Hagmann, M. M. Burger and D. Dagan, *Journal of Cellular Biochemistry*, 1999, 73, 488-499.
284. S. Link, C. Burda, M. B. Mohamed, B. Nikoobakht and M. A. El-Sayed, *Physical Review. B, Condensed Matter*, 2000, 61, 6086-6090.
- 75 285. V. Kotaidis and A. Plech, *Applied Physics Letters*, 2005, 87, 213102.
286. S. Link, Z. L. Wang and M. A. El-Sayed, *The Journal of Physical Chemistry B*, 2000, 104, 7867-7870.
287. S. Link, C. Burda, B. Nikoobakht and M. A. El-Sayed, *The Journal of Physical Chemistry B*, 2000, 104, 6152-6163.
- 80 288. H. Petrova, J. P. Juste, I. Pastoriza-Santos, G. V. Hartland and L. M. Liz-Marzan, *Physical chemistry chemical physics : PCCP*, 2006, 8, 814-821.
289. M. B. Mohamed, K. Z. Ismail, S. Link and M. A. El-Sayed, *The Journal of Physical Chemistry B*, 1998, 102, 9370-9374.
- 85 290. H. Kang, B. Jia, J. Li, D. Morrish and M. Gu, *Applied Physics Letters*, 2010, 96, 063702.
291. E. Y. Hleb, J. H. Hafner, J. N. Myers, E. Y. Hanna, B. C. Rostro, S. A. Zhdanok and D. O. Lapotko, *Nanomedicine*, 2008, 3, 647-667.
- 90 292. E. Y. Lukianova-Hleb and D. O. Lapotko, *IEEE J. Sel. Top. Quantum Electron.*, 2014, 20, 7300412 (7300412 pp.)-7300412 (7300412 pp.)
293. E. Y. Lukianova-Hleb, X. Y. Ren, J. A. Zasadzinski, X. W. Wu and D. O. Lapotko, *Advanced Materials*, 2012, 24, 3831-3837.
- 95 294. P. Cherukuri, E. S. Glazer and S. A. Curleya, *Advanced Drug Delivery Reviews*, 2010, 62, 339-345.
295. D. O. Lapotko, E. Y. Lukianova-Hleb and A. A. Oraevsky, *Nanomedicine*, 2007, 2, 241-253.
- 100 296. B. P. Danysh, P. E. Constantinou, E. Y. Lukianova-Hleb, D. O. Lapotko and D. D. Carson, *Theranostics*, 2012, 2, 777-787.
297. E. Y. Lukianova-Hleb, A. Belyanin, S. Kashinath, X. W. Wu and D. O. Lapotko, *Biomaterials*, 2012, 33, 1821-1826.
- 105 298. E. Lukianova-Hleb, Y. Hu, L. Latterini, L. Tarpani, S. Lee, R. A. Drezek, J. H. Hafner and D. O. Lapotko, *ACS Nano*, 2010, 4, 2109-2123.
299. H. Maeda, *Advances in enzyme regulation*, 2001, DOI: 10.1016/S0065-2571(00)00013-3, 189-207.
- 110 300. A. Iyer, G. Khaled, J. Fang and H. Maeda, *Drug Discovery Today*, 2006, 11, 812-818.
301. P. R. Seevinck, J. H. Seppenwoolde, T. C. de Wit, J. F. Nijssen, F. J. Beekman, A. D. van Het Schip and C. J. Bakker, *Anticancer Agents in Medicinal Chemistry*, 2007, 7, 317-334.
- 115 302. H. Wang, W. Su, S. Wang, X. Wang and Z. Liao, *Nanoscale*, 2012, 4, 6501-6508.
303. H. K. Moon, S. H. Lee and H. C. Choi, *ACS Nano*, 2009, 3, 3707-3713.
304. R. R. Anderson and J. A. Parrish, *Journal of Investigative Dermatology*, 1981, 77, 13-19.
- 120 305. N. N. Huang, H. Q. Wang, J. H. Zhao, H. Lui, M. Korbeklik and H. S. Zeng, *Lasers in Surgery and Medicine*, 2010, 42, 638-648.
306. L. C. Kennedy, L. R. Bickford, N. A. Lewinski, A. J. Coughlin, Y. Hu, E. S. Day, J. L. West and R. A. Drezek, *Small*, 2011, 7, 169-183.
- 125 307. F. Alexis, E. Pridgen, L. K. Molnar and O. C. Farokhzad, *Molecular Pharmaceutics*, 2008, 5, 505-515.
308. L. Balogh, S. S. Nigavekar, B. M. Nair, W. Lesniak, C. Zhang, L. Y. Sung, M. S. Kariapper, A. El-Jawahri, M. Llanes, B. Bolton, F. Mamou, W. Tan, A. Hutson, L. Minc and M. K. Khan, *Nanomedicine*, 2007, 3, 281-296.
- 130 309. Z. Liu, C. Davis, W. B. Cai, L. He, X. Y. Chen and H. J. Dai, *Proceedings of the National Academy of Sciences of the United States of America*, 2008, 105, 1410-1415.
310. F. Sousa, S. Mandal, C. Garrovo, A. Astolfo, A. Bonifacio, D. Latawiec, R. H. Menk, F. Arfelli, S. Huewel, G. Legname, H. J. Galla and S. Krol, *Nanoscale*, 2010, 2, 2826-2834.
311. G. Zhang, Z. Yang, W. Lu, R. Zhang, Q. Huang, M. Tian, L. Li, D. Liang and C. Li, *Biomaterials*, 2009, 30, 1928-1936.
- 140 312. S. D. Perrault, C. Walkey, T. Jennings, H. C. Fischer and W. C. Chan, *Nano Letters*, 2009, 9, 1909-1915.
313. B. Kim, G. Han, B. J. Toley, C. K. Kim, V. M. Rotello and N. S. Forbes, *Nature Nanotechnology*, 2010, 5, 465-472.

314. K. Welsher, S. P. Sherlock and H. Dai, *Proceedings of the National Academy of Sciences of the USA*, 2011, 108, 8943-8948.
315. J. T. Robinson, G. Hong, Y. Liang, B. Zhang, O. K. Yaghi and H. Dai, *Journal of the American Chemical Society*, 2012, 134, 10664-10669.
316. B. J. Darien, P. A. Sims, K. T. Kruseelliott, T. S. Homan, R. J. Cashwell, A. J. Cooley and R. M. Albrecht, *Scanning Microscopy*, 1995, 9, 773-780.
- 10 317. T. A. Erickson and J. W. Tunnell, in *Nanotechnologies for the Life Sciences*, Wiley-VCH Verlag GmbH & Co. KGaA, 2007, DOI: 10.1002/9783527610419.ntls0150.
318. G. Hong, J. T. Robinson, Y. Zhang, S. Diao, A. L. Antaris, Q. Wang and H. Dai, *Angewandte Chemie International Edition*, 2012, 51, 9818-9821.
- 15 319. K. Yang, S. Zhang, G. Zhang, X. Sun, S. T. Lee and Z. Liu, *Nano Letters*, 2010, 10, 3318-3323.
320. Y. Zhang, G. Hong, Y. Zhang, G. Chen, F. Li, H. Dai and Q. Wang, *ACS Nano*, 2012, 6, 3695-3702.
- 20 321. J. Chen, C. Glaus, R. Laforest, Q. Zhang and M. Yang, *Small*, 2010, 6, 811-817.
322. E. Day, P. A. Thompson, L. Zhang, N. A. Lewinski and N. Ahmed, *Journal of Neuro-Oncology*, 2011, 104, 55-63.
323. R. Atkinson, M. Zhang, P. Diagaradjane, S. Peddibhotla and A. Contreras, *Science Translational Medicine*, 2010, 2, 55ra79.
- 25